

**ELM Suppression and Pedestal Structure in I-Mode Plasmas on  
Alcator C-Mod**

by

John Reel Walk, Jr.

S.B. Physics & Mathematics (2010)  
Massachusetts Institute of Technology

Submitted to the Department of Nuclear Science and Engineering  
in partial fulfillment of the requirements for the degree of

Doctor of Philosophy in Applied Plasma Physics

at the

MASSACHUSETTS INSTITUTE OF TECHNOLOGY

June 2014

© Massachusetts Institute of Technology 2014. All rights reserved.

Author .....  
.....

Department of Nuclear Science and Engineering  
June 10, 2014

Certified by.....

Jerry W. Hughes  
Research Scientist, Plasma Science and Fusion Center  
Thesis Supervisor

Certified by.....

Dennis G. Whyte  
Professor, Department of Nuclear Science and Engineering  
Thesis Reader

Accepted by .....

Mujid S. Kazimi  
TEPCO Professor of Nuclear Engineering  
Chair, Department Committee on Graduate Students



**ELM Suppression and Pedestal Structure in I-Mode Plasmas on Alcator C-Mod**  
by  
John Reel Walk, Jr.

Submitted to the Department of Nuclear Science and Engineering  
on June 10, 2014, in partial fulfillment of the  
requirements for the degree of  
Doctor of Philosophy in Applied Plasma Physics

*Abstract*

Abstract goes here.

Thesis Supervisor: Jerry W. Hughes  
Research Scientist, Plasma Science and Fusion Center

Thesis Reader: Dennis G. Whyte  
Professor, Department of Nuclear Science and Engineering



A dedication goes here maybe?



## ACKNOWLEDGMENTS

---

Acknowledgements go here.



## CONTENTS

---

<b>1</b>	<b>INTRODUCTION</b>	<b>15</b>
1.1	Plasmas for Fusion	16
1.1.1	Plasma Parameters	16
1.1.2	Fusion Fuels	17
1.2	Magnetic Confinement	20
1.2.1	Basic Principles	20
1.2.2	Toroidal Configurations	23
1.3	Alcator C-Mod	27
1.4	Confinement & Transport	30
1.4.1	Global Confinement	30
1.4.2	Transport Barriers	32
1.5	Goals & Outline	34
<b>2</b>	<b>HIGH-PERFORMANCE REGIMES</b>	<b>41</b>
2.1	ELM-Free H-Mode	42
2.2	ELMy H-Mode	44
2.2.1	ELMy H-Mode Operation	44
2.2.2	Edge-Localized Modes & Pedestal Limits	46
2.2.3	Active ELM Control	48
2.2.4	Prospects for ELMy H-Mode	49
2.3	ELM-Suppressed H-Modes	49
2.3.1	QH-Mode	50
2.3.2	EDA H-Mode	51
2.4	I-Mode	54
2.4.1	Access and Operation	55
2.4.2	Global Performance & Edge Behavior	56
2.4.3	Edge Fluctuations – the Weakly-Coherent Mode	58
<b>3</b>	<b>PEDESTAL MODELING AND THEORY</b>	<b>73</b>
3.1	Early Models	73
3.1.1	Empirical Observations	73
3.1.2	Neutral Penetration & the Density Pedestal	74
3.1.3	Ion-Orbit Loss & Gyradius Models	75
3.2	MHD Stability: Peeling-Ballooning Modes	76
3.2.1	Ballooning MHD	77
3.2.2	Peeling MHD	77
3.2.3	ELITE Code	77
3.3	Kinetic-Ballooning Turbulence Modeling	77
3.4	The EPED Model	77
<b>4</b>	<b>ELMY H-MODES ON C-MOD</b>	<b>83</b>
4.1	ELMy H-Mode Access & Experimental Arrangement	83

4.2	ELM Cycle Synchronization	88
4.3	EPED Model Predictions	89
4.3.1	Pedestal Height	90
4.3.2	Pedestal Width	91
4.4	Engineering Parameter Scan	94
4.4.1	$I_p$ Scan	95
4.5	Pedestal Width Response	98
4.5.1	Alternate Width Models	98
4.5.2	Normalized Pedestal Width	99
4.6	Conclusions	102
<b>5</b>	<b>I-MODE PEDESTAL SCALINGS</b>	<b>109</b>
5.1	Access and Experimental Setup	110
5.2	Pedestal Responses	110
5.2.1	Pedestal Temperature	110
5.2.2	Pedestal Response to Fueling	110
5.2.3	Pressure Pedestal Scalings and Performance	110
5.3	Pedestal Widths	110
5.4	Global Behavior, Performance, & Confinement	111
5.5	Fluctuation Characterization	111
<b>6</b>	<b>I-MODE PEDESTAL STABILITY MODELING</b>	<b>117</b>
6.1	MHD Stability – ELITE	117
6.2	KBM and Infinite-n MHD Stability	117
6.3	Sawtooth Perturbations of Pedestal Stability	117
6.4	Other Models	117
<b>7</b>	<b>CONCLUSIONS</b>	<b>121</b>
<b>A</b>	<b>DIAGNOSTICS</b>	<b>125</b>
A.1	Thomson Scattering	125
A.1.1	Principles of Thomson Scattering	126
A.1.2	Edge Thomson Scattering on C-Mod	134
A.2	Fast Diagnostics	136
A.2.1	Electron-Cyclotron Emission	137
A.2.2	$H_\alpha$ Emission	138
A.3	Fluctuation Diagnostics	138
<b>B</b>	<b>HIGH-RESOLUTION PEDESTAL DATABASE</b>	<b>141</b>

## LIST OF FIGURES

---

Figure 1.1	Binding energy per nucleon versus atomic mass number.	18
Figure 1.2	Normalized fusion reaction rate coefficients versus plasma temperature.	19
Figure 1.3	Gyro orbits in an applied magnetic field.	21
Figure 1.4	Geometry of a toroidal plasma.	23
Figure 1.5	Schematic of a tokamak coil configuration and plasma.	25
Figure 1.6	Tokamak cross-section with shaping parameter definitions.	26
Figure 1.7	Cutaway view of the Alcator C-Mod tokamak, cryostat and support structure.	28
Figure 1.8	Labeled cross-section of the C-Mod vacuum vessel.	29
Figure 1.9	Diffusion coefficients and plasma profiles for a “toy model” diffusion equation.	33
Figure 2.1	Characteristic traces of transient ELM-free H-modes.	43
Figure 2.2	Characteristic traces of a steady ELMy H-mode.	45
Figure 2.3	ELMy H-mode pedestal density and temperature on a fixed- $\beta_{p,ped}$ line.	45
Figure 2.4	Characteristic traces of an EDA H-mode on C-Mod.	52
Figure 2.5	C-Mod cross-sections illustrating magnetic configurations suitable for I-mode access.	55
Figure 2.6	Characteristic traces for a typical I-mode, and comparisons of I-mode pedestal profiles to L- and H-modes.	57
Figure 2.7	Impurity confinement time versus normalized confinement for L-, I-, and H-mode.	58
Figure 2.8	Fluctuations from the WCM in I-mode.	59
Figure 3.1	Schematic of peeling-balloonning MHD stability space.	77
Figure 3.2	Illustration of the peeling-balloonning MHD and KBM constraints used in the EPED model.	78
Figure 3.3	EPED predictions versus measured pressure pedestal heights.	78
Figure 4.1	C-Mod cross-section comparing typical and ELMy H-mode shaping.	84
Figure 4.2	Example time window for ELMy H-mode study, showing TS timebase.	85

- Figure 4.3 Comparison of pedestal fits for individual frames versus ensemble average. 86
- Figure 4.4 Example pedestal illustrating the  $\text{mtanh}$  fitting function. 87
- Figure 4.5 Comparison of measured  $n_e$  and  $T_e$  pedestal widths. 88
- Figure 4.6 Comparison of directly measured pressure pedestal width versus EPED pedestal width. 88
- Figure 4.7 Comparison of pressure pedestal height between ensemble-averaged and ELM-synced profiles. 89
- Figure 4.8 Comparison of pressure at the 95% flux surface between ensemble-averaged and ELM-synced profiles. 89
- Figure 4.9 Pressure pedestal height predicted by EPED versus measured (ensemble-averaged) height. 90
- Figure 4.10 Pressure pedestal height predicted by EPED versus measured ELM-synced pedestal height. 91
- Figure 4.11 Ensemble-averaged  $\Delta_\psi$  versus  $\beta_{p,\text{ped}}$ . 92
- Figure 4.12 Comparison of EPED-predicted pedestal width and height with corresponding experimental points. 92
- Figure 4.13 Comparison of ensemble-averaged and ELM-synced pedestal width and height, compared to the KBM constraint. 93
- Figure 4.14 ELM-synced pedestals with data binned by  $\beta_{p,\text{ped}}$ , fitted to  $\Delta_\psi \sim \beta_{p,\text{ped}}^{1/2}$ . 94
- Figure 4.15 Measured ensemble-averaged pedestal width versus EPED predictions. 94
- Figure 4.16 Measured ELM-synced pedestal width versus EPED predictions. 95
- Figure 4.17 Plasma current scalings of the density, temperature, and pressure pedestals. 96
- Figure 4.18 Pedestal density versus temperature normalized to poloidal field. 97
- Figure 4.19 Pedestal pressure versus  $I_p \sqrt{T_{e,95}}$  98
- Figure 4.20 Pedestal pressure versus  $I_p \sqrt{n_{e,95} T_{e,95}}$  98
- Figure 4.21  $\Delta_{n_e}$  versus  $n_{e,\text{ped}}$  98
- Figure 4.22  $\Delta_{T_e}$  and  $\Delta_p$  versus  $\rho_{i,\text{pol}}$  99
- Figure 4.23 Scaling of the normalized pedestal width with applied toroidal field. 100
- Figure 4.24 Scalings of normalized pedestal width with shaping parameters. 101
- Figure 4.25 Scaling of normalized pedestal width with pedestal collisionality. 102
- Figure 4.26 Scaling of normalized pedestal width with normalized pedestal ion gyroradius. 102

Figure 5.1	I-mode edge safety collisionality and safety factor. <a href="#">110</a>
Figure 5.2	Density and temperature pedestals at matched current and field with varying fueling and heating power – matched $P_{\text{net}}/\bar{n}_e$ maintains the $T_e$ pedestal. <a href="#">111</a>
Figure 5.3	Power-law fit to I-mode $\tau_E$ with full parameter set. <a href="#">111</a>
Figure 5.4	Power-law fit to I-mode $\tau_E$ , with poorly-fitted parameters excluded. <a href="#">112</a>
Figure 5.5	Power-law fit to I-mode $\tau_E$ , with fixed $R^2\sqrt{\epsilon}$ size scaling. <a href="#">113</a>
Figure 5.6	Power-law fit to I-mode $\tau_E$ extrapolated to larger devices. <a href="#">113</a>
Figure A.1	Coordinate system for Thomson scattering. <a href="#">126</a>
Figure A.2	Angular dependences in Thomson scattering geometry. <a href="#">128</a>
Figure A.3	Spectral functions normalized to density and laser power. <a href="#">133</a>
Figure A.4	Collection optics for core and edge Thomson scattering systems. <a href="#">135</a>
Figure A.5	Normalized spectral response functions of the edge TS polychromator. <a href="#">136</a>

## LIST OF TABLES

---

Table 1.1	Summary of Alcator C-Mod typical operating parameters. <a href="#">29</a>
Table 2.1	Typical operating parameters of tokamaks noted in this thesis, along with references to overviews of each machine. <i>Note:</i> all ITER values are projected. <a href="#">check all values here</a> <a href="#">42</a>
Table 5.1	Parameters for power-law scalings of I-mode energy confinement time. <a href="#">112</a>
Table B.1	SQL database parameters used as keys – (SHOT, TA, TB) is sufficient to uniquely identify entries in the database. <a href="#">141</a>
Table B.2	SQL database parameters used as flags for time windows. <a href="#">142</a>
Table B.3	SQL database parameters for useful measured parameters. <a href="#">142</a>
Table B.4	SQL database parameters for EFIT values. <a href="#">143</a>

Table B.5	SQL database parameters for heating power, stored energy, and confinement. <a href="#">144</a>
Table B.6	SQL database parameters for high-resolution pedestal profiles. <a href="#">145</a>
Table B.7	SQL database parameters for WCM fluctuation measurements. <a href="#">146</a>

## INTRODUCTION

---

The population of the earth is projected to increase substantially over the next half-century, potentially reaching as high as 10 billion globally by 2050 [1]. At the same time, any attempt to increase the quality of life of the existing population will necessarily involve increased energy consumption per capita, with a greater fraction of the earth approaching “first-world” consumption levels [2]. As such, worldwide energy consumption will likely continue to increase in the next few decades [3, 4]

This increase in energy demand occurs in parallel with increased pressure on traditional energy sources. Fossil fuels (oil, coal, and natural gas), while reliable sources of base-load power, nevertheless face issues. Oil faces increasing cost and technical difficulty in capturing dwindling available reserves, as well as the potential for serious ecological damage from accidents (e.g., the Deepwater Horizon offshore rig accident in 2010). Coal, while more readily available (an estimated 257 billion tons of recoverable reserves in the US, lasting roughly 240 years at current consumption [4, 5]), releases particulate matter into the atmosphere, with serious consequences both to the environment and to human health, as well as the greenhouse gases tied to deleterious climate change.

Renewable energy sources have a certain “green” appeal, providing power generation free of pollution and carbon emissions, and are in many cases scalable and near cost-competitive with fossil-fuel sources – however, each is subject to limitations on their implementation. Solar and wind power suffer from a large degree of variability in their output, necessitating a combination of expensive energy storage methods or (often fossil-fuel based) backup production to handle shortfalls. Hydroelectric and geothermal power are suitable for base-load power production, but are strictly limited in their implementation by geographic concerns – bluntly, there are relatively few locations where hydro or geothermal power generation is feasible, and many of these have already been developed.

Conventional – that is, fission-based – nuclear power can also supply carbon-free base-load power, with fuel reserves lasting through the next century. While nuclear power does suffer from the potential for extremely serious accidents (Fukushima, Chernobyl) it has, on a per-energy-produced basis, a remarkably good safety record. Public perception of nuclear power nevertheless hinges on the threat of serious accidents, limiting both the expansion of nuclear power to meet increasing demand and the development of safe long-term handling

of existing nuclear waste, as well as, ironically, preventing the replacement of an aging reactor fleet with newer, safer designs.

*Fusion*, the nuclear process driving stellar cores, is a potentially highly attractive option for satisfying the world's growing energy needs in an efficient, environmentally-sound manner. A fusion reactor would supply base-load power using only a small amount of an effectively inexhaustible fuel (readily available for harvesting from seawater), with no greenhouse gas emissions or high-level radioactive waste, and the physical impossibility of a major "meltdown" accident. However, fusion remains in the experimental stage, with significant technical hurdles remaining before the development of a prototype fusion power plant. This thesis will attempt to contribute to the understanding of one of these hurdles. Further reading on the development of fusion energy is available to the interested reader in several excellent references. [6, 7, 8] •

## 1.1 PLASMAS FOR FUSION

A *plasma* is a gas to which sufficient energy has been applied to strip some or all of the electrons from the nuclei of its constituent atoms. In a plasma, ions and electrons freely interact with one another, behaving as coupled fluids. Plasmas of interest for fusion research are comprised of light elements (typically hydrogen or helium), and are at extremely high temperatures, in excess of 100 million Kelvin (10 – 20 keV). As these conditions are far in excess of the ionization energy for these elements, the plasma is dominated by collisions between its charged particles, rather than interactions with bound electron states.

### 1.1.1 *Plasma Parameters*

As the plasma is composed of free charged particles, it responds strongly to electric and magnetic fields. In the presence of a DC electric field (externally applied, or generated by an imbalance of positive and negative charge in the plasma), the plasma will rearrange itself to screen out the field. This effect breaks down at short length scales, at which there are insufficient numbers of charge carriers to rearrange and counter the field – the characteristic scale for this effect is the Debye Length, given by

$$\lambda_D = \sqrt{\frac{\epsilon_0 T}{n e^2}} \quad (1.1)$$

At size scales significantly larger than  $\lambda_D$ , this will enforce an approximately balanced electric charge in the plasma, termed "quasi-

“neutrality”. This is reflected in the number densities of electrons and multiple ion species  $j$ , each with charge  $Z_j$ , by the relation

$$n_e = \sum_j n_j Z_j \quad (1.2)$$

In a multiple-ion species plasma, we may also define an effective ion charge

$$Z_{\text{eff}} = \frac{1}{n_e} \sum_j n_j Z_j^2 \quad (1.3)$$

The electrostatic force driving this charge redistribution induces a “ringing” oscillation in the plasma, at the characteristic plasma frequency  $\omega_p$ :

$$\omega_p = \sqrt{\frac{n e^2}{\epsilon_0 m_e}} \quad (1.4)$$

This natural oscillation in the plasma also has the effect of screening AC electric fields varying at frequencies  $\omega < \omega_p$ .

Coulomb collisions between charged particles in the plasma tend to drive magnetically-confined plasmas into thermal equilibrium, with the velocity distribution for a species given by the Maxwellian

$$f(v) = n \left( \frac{m}{2\pi T} \right)^{3/2} \exp \left( -\frac{mv^2}{2T} \right) \quad (1.5)$$

These collisions also cause the plasma to emit a continuous spectrum of Bremsstrahlung radiation. For a plasma in thermal equilibrium, integration over the full spectrum gives for the total radiated power

$$P_{\text{Brems}} = (5.35 \times 10^{-37}) n_e^2 Z_{\text{eff}} \sqrt{T} \quad (1.6)$$

representing a consistent source of heat loss from the plasma.

### 1.1.2 Fusion Fuels

Fusion collectively refers to the class of nuclear reactions merging lighter nuclei into a single heavier element. While fusion reactions for elements lighter than iron are generally exothermic, as they form nuclei with greater binding energy per nucleon (see fig. 1.1), the most common and readily attainable involve isotopes of hydrogen or helium, the most promising candidates for which are shown below.



**Figure 1.1:** Binding energy per nucleon versus atomic mass number, with notable isotopes marked. Reactions forming nuclei with higher binding energy are exothermic – thus, fusion of elements lighter than  $^{56}\text{Fe}$  or fission of elements heavier than  $^{56}\text{Fe}$  releases energy. [9]



Here D and T indicate nuclei of deuterium and tritium, two heavy isotopes of hydrogen (one proton plus one and two neutrons, respectively). The fusion reaction rate  $R_f$  is given by

$$R_f = n_1 n_2 \langle \sigma v \rangle_{1,2} \quad (1.11)$$

where  $n_1$  and  $n_2$  indicate the densities of the two fuel ions (e.g., for deuterium-tritium fuel  $n_1 n_2 = n_D n_T$ , while for pure-deuterium fuel  $n_1 n_2 = \frac{1}{2} n_D^2$  to remove double-counting of fuel ions) and  $\langle \sigma v \rangle_{1,2}$  is a rate parameter incorporating the energy-dependent reaction cross-section averaged over the Maxwellian fuel distribution (eq. (1.5)). In practice, the energy-dependent cross-section is empirically determined – measured rate parameters  $\langle \sigma v \rangle$  for the fuels of interest are shown in fig. 1.2.



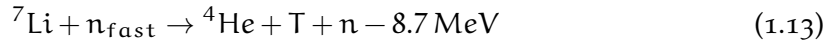
**Figure 1.2:** Reaction rate normalized to fuel density, expressed as the rate coefficient  $\langle\sigma v\rangle$ , for fusion fuels as a function of temperature. Notably, deuterium-tritium fusion exhibits a higher peak reaction rate, as well as reaching that peak at a lower temperature, than other fuels.

Pure deuterium fuel (reactions shown in eqs. (1.7) and (1.8)) is attractive from a research standpoint, due to the abundance and ease of use of deuterium. Deuterium is a stable nucleus, obviating the need for radiation safety in the fuel system, and is naturally occurring in relative abundance (approximately 1/6420 of hydrogen nuclei on earth are deuterium [10]), allowing harvesting of deuterium fuel from seawater. However, pure-deuterium reactions suffer from low energy output per reaction and a significantly lower reaction rate at feasible plasma conditions compared to other fuel options (see fig. 1.2), setting high performance requirements for a putative DD-burning reactor.

The  $D - {}^3He$  reaction (eq. (1.9)) exhibits several desirable properties, namely an impressive energy yield per reaction, and the fact that the reaction produces only charged particles rather than the high-energy neutrons found in  $D - D$  and  $D - T$  reactions, which can cause significant damage to reactor materials (note, however, that a  $D - {}^3He$  plasma will also undergo neutronic  $D - D$  fusion at a meaningful rate). However, as with  $D - D$  fuel, the  $D - {}^3He$  reaction suffers from a lower reaction rate at attainable conditions, as well as the fact that Helium-3 does not occur in economically usable quantities on Earth. While off-planet sources of Helium-3 exist (for example, a useful quantity is present in the lunar regolith [11] and in the

atmospheres of some gas giants [12]), this fuel remains the subject of speculation.

The deuterium-tritium reaction (eq. (1.10)) is considered the most promising for a first-generation fusion reactor, due to its high energy output per reaction and favorable reaction cross-section – the rate parameter  $\langle\sigma v\rangle_{DT}$  reaches its peak at a lower temperature, and reaches a greater absolute level than other fusion fuels. However, D – T operation is limited both by fuel sources, and reaction products. D – T fusion produces a 14 MeV neutron, carrying roughly 80% of the energy released by the fusion reaction, which can damage unshielded reactor materials. Moreover, while deuterium is stable and readily available, tritium is radioactive with a short half-life (roughly 12.3 years), so it is not naturally occurring in meaningful quantities on earth. A reactor will solve both of these problems with a *neutron blanket*, a neutron-absorbing structure surrounding the plasma. This provides the necessary shielding for sensitive reactor components. The heat generated in the blanket from neutron absorption will also be drawn off in a steam cycle to drive turbines, generating electricity from the reactor. Finally, seeding the blanket with lithium allows the following reactions with fusion neutrons:



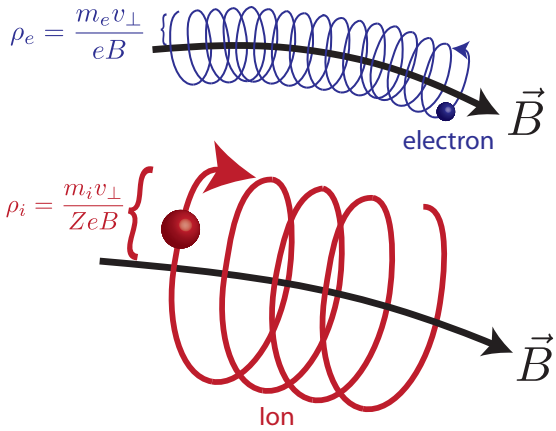
the Lithium-6 reaction (eq. (1.12)) absorbs “slow” neutrons (that is, neutrons that have thermalized to the blanket temperature via collisions) to produce tritium, plus additional heat. Lithium-7 (eq. (1.13)) is more likely to capture fast neutrons to produce tritium in an endothermic reaction; however, the reaction also acts as a neutron multiplier, as a free neutron is maintained through the reaction. Using blankets enriched with  ${}^6\text{Li}$ , coupled with neutron multipliers, a reactor will target an over-unity tritium breeding ratio, with  $> 1$  tritons produced per neutron entering the blanket (i. e., per tritium consumed in a fusion reaction). •

## 1.2 MAGNETIC CONFINEMENT

### 1.2.1 Basic Principles

The temperatures in excess of 100 million Kelvin necessary for fusion in a plasma are incompatible with any contact between solid reactor materials and the hot core of the plasma. Magnetic confinement relies on the strong response of the charged particles composing the plasma to magnetic fields, rather than a material wall, to retain the thermal pressure ( $\sim 10$  atm for a reactor) from the plasma. The response of

**Figure 1.3:** Electron and ion gyro orbits in an applied magnetic field. Note that, due to the charge dependence in the Lorentz Force (eq. (1.14)), electrons and ions orbit in opposite directions relative to the magnetic field.



a charged particle to electric and magnetic fields is governed by the Lorentz force,

$$\vec{F} = q \left( \vec{E} + \vec{v} \times \vec{B} \right) \quad (1.14)$$

In a strong background magnetic field, the particle will move on a helical path along the field line. The  $\vec{v} \times \vec{B}$  factor in the Lorentz Force causes the particle to experience no magnetic force parallel to the field, while velocity perpendicular to the field generates a force proportional to the velocity times the magnetic field, directed perpendicular to both – thus the particle freely streams parallel to the field, but is trapped in a circular orbit perpendicular to it, termed “gyro motion”, shown in fig. 1.3. The particle will orbit at the cyclotron frequency,

$$\omega_c = \frac{qB}{m} \Rightarrow \omega_{ce} = \frac{eB}{m_e}, \quad \omega_{ci} = \frac{ZeB}{m_i} \quad (1.15)$$

for electrons and ions of charge  $Z$ , respectively (note that for brevity we indicate the magnitude of vectors as scalar variables, e.g.,  $B = |\vec{B}|$ ). A particle with velocity perpendicular to the magnetic field  $v_\perp$  (formally,  $v_\perp = |\vec{v} \times \vec{B}| / B$ ) orbits at its gyroradius,

$$\rho = \frac{v_\perp}{\omega_c} = \frac{mv_\perp}{qB} \quad (1.16)$$

For a thermalized plasma, the perpendicular velocity will, on average, be the thermal velocity  $v_t = \sqrt{2T/m}$ , thus

$$\rho = \frac{\sqrt{2mT}}{qB} \quad (1.17)$$

The introduction of a nonzero electric field drives additional motion for the particle in the form of a drift velocity – the guiding center (that is, the average point about which the orbital motion of the particle gyrates) will shift with a bulk velocity (see [6, § 8.4] for derivation)

$$\vec{v}_d = \frac{\vec{E} \times \vec{B}}{B^2} \quad (1.18)$$

independent of particle charge, mass, or energy.

This restriction of particle motion perpendicular to field lines to short length scales (at fusion-relevant temperatures and magnetic fields, the gyroradius is typically  $\sim 10^{-5}$  m for electrons and  $\sim 10^{-3}$  m for ions) compared to the size of the plasma is central to the concept of magnetic confinement. In the perpendicular direction, this scale restriction of particle motion permits a fluid treatment of the dynamics of the plasma. Further simplification of the fluid model (see [13, § 2.3] for detailed derivation) leads to the theory of *magnetohydrodynamics* (MHD), the “workhorse” model describing plasma behavior. A basic equilibrium in a confined plasma is described in MHD by the simple relation

$$\nabla p = \vec{J} \times \vec{B} \quad (1.19)$$

in which the outward force due to the plasma pressure gradient is balanced by an inward force from the interplay between magnetic fields and electric currents (expressed by the current density  $\vec{J}$ ). This interplay is readily illustrated in the simple one-dimensional case of an infinite straight cylinder of plasma – in this case, the radially-outward  $\nabla p$  force may be balanced by an axial current in the  $\hat{z}$  direction with an azimuthal  $\hat{\theta}$  magnetic field (z-pinch), an azimuthal current and axial field ( $\theta$ -pinch), or a superposition of the two (screw pinch). However, all three of these options suffer from a lack of parallel confinement – as the magnetic field does not restrict the free-streaming parallel motion of the plasma, these linear concepts (when reduced to a physical, non-infinite size!) suffer from plasma losses at the ends of the cylinder. Despite efforts to restrict the parallel motion in a linear device (e.g., the *magnetic mirror*, which pinches the magnetic field at the cylinder ends in order to reflect the parallel motion of particles with a force due to the field gradient [14]), end losses in linear de-

vices proved incompatible with steady-state fusion conditions. The clear solution, then, was to close the magnetic geometry such that the magnetic field lines have no ends: a *torus*.

### 1.2.2 Toroidal Configurations

**Figure 1.4:** Example geometry of a circular-cross-section tokamak plasma, describing a torus of major radius  $R_0$  and minor radius  $a$ , with poloidal coordinate  $\theta$  and toroidal coordinate  $\Phi$ . Tokamak configurations are characterized by an applied toroidal field  $B_T$  with a toroidal plasma current  $I_p$ , which in turn generates a poloidal magnetic field  $B_p$ .



An example toroidal geometry is shown above in fig. 1.4. In comparison to the previous straight cylindrical geometry, the radial coordinate is replaced by a *minor radius*  $r$ , measured from the center of the plasma column to its edge ( $r = a$ ), while the *major radius*  $R_0$  denotes the radius of the torus itself measured from its center axis ( $Z$  in fig. 1.4) to the plasma axis. The azimuthal cylindrical coordinate is replaced by the poloidal coordinate  $\theta$ , wrapping immediately about the plasma column. The axial coordinate in the cylindrical system is replaced by the toroidal angle  $\Phi$  wrapping around the center axis of the torus and describing a circuit along the plasma column. As with the straight cylindrical case, the magnetic geometry may be described with toroidal and poloidal currents and magnetic fields balancing radially-outward thermal pressure.

However, introducing toroidal effects into the magnetic geometry gives rise to additional drift velocities, causing the guiding centers of

particle gyro-orbits to shift (see [6, § 8.5-7]). Spatial variation in the magnetic field strength causes the  $\nabla B$  drift, given by

$$\vec{v}_{\nabla B} = \frac{v_{\perp}^2}{2\omega_c} \frac{\vec{B} \times \nabla B}{B^2} \quad (1.20)$$

while the toroidal twist in the magnetic field causes the curvature drift,

$$\vec{v}_k = \frac{v_{\parallel}^2}{\omega_c} \frac{\vec{R}_c \times \vec{B}}{R_c^2 B} \quad (1.21)$$

where  $v_{\parallel}$  is the particle velocity parallel to the magnetic field,  $\omega_c$  is the species cyclotron frequency (eq. (1.15)), and  $\vec{R}_c$  is the radius of curvature of the field. In the case of an applied toroidal magnetic field, these drifts are directed vertically in the  $\hat{Z}$  direction, and are directed oppositely for electrons and ions due to the charge dependence in  $\omega_c$ . The electric field resulting from this charge separation drives an outward  $\vec{E} \times \vec{B}$  drift (see eq. (1.18)), breaking confinement. This effect is countered by the addition of a poloidal field, which adds a helical twist to the guiding-center path to average out the separation due to particle drifts. Concepts aiming for steady-state magnetic confinement of a plasma typically rely on generating this twist, termed the *rotational transform*, to maintain stable confinement.

One of the most successful implementations of this concept for Magnetic Fusion Energy (MFE) is the *tokamak* [7] (a Russian acronym from *тороидальная камера с магнитными катушками*, *toroidalnaya kamera s magnetnymi katushkami*, “toroidal chamber with magnetic coils”). The tokamak design is characterized by a strong toroidal magnetic field (variously denoted  $B_T$  or  $B_\Phi$ ) applied by external coils, with a poloidal field ( $B_p$  or  $B_\theta$ ) primarily generated by a current (termed the *plasma current*  $I_p$ ). A schematic of the plasma and coil arrangement for a tokamak is shown in fig. 1.5. By generating the rotational transform to the magnetic field using the plasma current, the tokamak design utilizes relatively simple planar magnetic coils, avoiding the significantly more complex three-dimensional coils used to generate the helical field in a *stellarator* (the major competing design concept [15]). However, the necessity for large ( $> 1$  MA) plasma currents presents a significant engineering and physics challenge. It is straightforward to generate the plasma current through a simple transformer action from a central solenoid in the torus (depicted in fig. 1.5) – however, this AC-current-driven transformer action necessarily limits tokamaks to pulsed operation. Generation of non-inductive DC current drive [16], via RF [17, 18] or particle beams [19], is an active area of research in tokamak physics and engineering, but is outside the scope of this thesis.

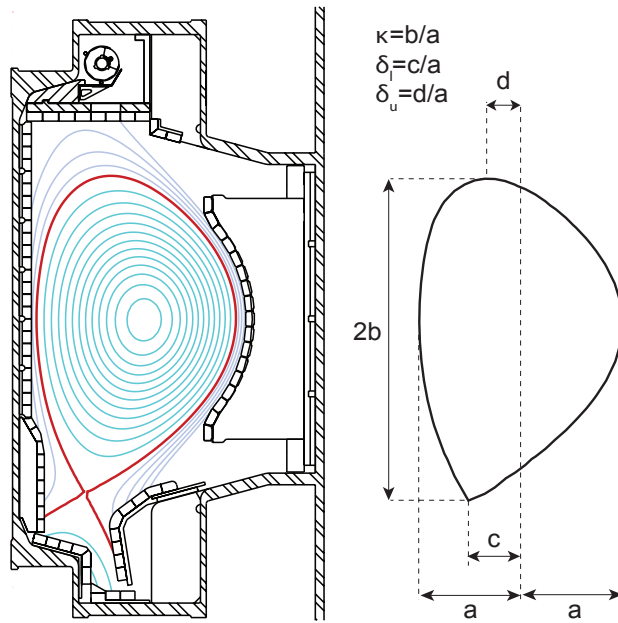


**Figure 1.5:** Schematic of a tokamak configuration, showing the plasma and magnetic coils. The applied toroidal magnetic field is generated by the toroidal field coils (shown in blue). A toroidal plasma current is generated by the center transformer, in turn generating a poloidal magnetic field (shown in green). These combine to form the helical magnetic field. The plasma shape and equilibrium is adjusted with the outer poloidal field coils (gray).

Due to its regular, planar magnetic coils and continuous plasma current, tokamak equilibria are characterized by rotational symmetry (to good approximation) about the center axis of the torus (*axisymmetry*). Solutions to the MHD equilibrium equation, eq. (1.19), thus reduce to a two-dimensional equation in  $R$  and  $Z$  (as  $\partial/\partial\Phi \rightarrow 0$ ), given by the Grad-Shafranov Equation [13, 20, 21]:

$$\begin{aligned}\Delta^*\psi &= -\mu_0 R^2 \frac{dp}{d\psi} - \frac{1}{2} \frac{dF^2}{d\psi} \\ \Delta^*\psi &= R^2 \nabla \cdot \left( \frac{1}{R^2} \nabla \psi \right) = R \frac{\partial}{\partial R} \left( \frac{1}{R} \frac{\partial \psi}{\partial R} \right) + \frac{\partial^2 \psi}{\partial Z^2}\end{aligned}\quad (1.22)$$

**Figure 1.6:** Cross-section of a plasma on the Alcator C-Mod tokamak, illustrating closed magnetic flux surfaces (light blue), the last closed flux surface (red), and surfaces with open magnetic field lines (dark blue). Definitions for plasma shaping parameters elongation  $\kappa$ , and upper and lower triangularity  $\delta_u$ ,  $\delta_l$  are shown at right.



where  $F = RB_\phi$  encodes the toroidal field and  $p$  is the thermal pressure. The poloidal field (equivalently, the plasma current profile) is described by the poloidal magnetic flux  $\psi$ ,

$$\psi = \frac{1}{2\pi} \int \vec{B}_p \cdot d\vec{S} \quad (1.23)$$

where  $\vec{S}$  is a surface with one edge along the magnetic axis. In eq. (1.22),  $\psi$  is treated as both an dependent parameter encoding the current, and as an independent variable – a consequence of Grad-Shafranov is that a number of parameters of interest, including pressure and current density, are *flux functions*, constant on a surface of constant  $\psi$ , and thus can be expressed as functions of  $\psi$  alone, e.g.  $p = p(\psi)$ . Moreover, magnetic field lines lie within surfaces of constant flux, with helical structure encoded by the flux function  $q(\psi)$ , termed the *safety factor*, given for a circular cross-section by

$$q = \frac{rB_\Phi}{RB_\theta} \quad (1.24)$$

As the plasma temperature rapidly equilibrates along field lines, the temperature is also a flux function to good approximation. It is useful, then, to picture the confined plasma as a series of closed, nested surfaces of constant  $\psi$ , on which the plasma is trapped (see fig. 1.6). In practice, these contours are calculated via a numerical solution of eq. (1.22) by an equilibrium solver such as the EFIT code [22]. For flux functions (i. e., constant parameters on these flux surfaces), this explic-

itly removes the dependence on the poloidal angle  $\theta$  – the poloidal flux  $\psi$  is thus a useful one-dimensional abscissa derived directly from the magnetic geometry (thus independent of the physical scale of the tokamak and useful for cross-machine comparisons) for the profiles of most parameters of interest, and shall be used thus for the balance of this thesis.

Using outer poloidal field coils (shown in fig. 1.5), the tokamak operator may push the plasma into a non-circular shape, with beneficial effects on plasma performance and stability. In general, flux surfaces sufficiently far from the plasma core will not close on themselves, instead intersecting the wall; the boundary between closed, nested surfaces and these open surfaces is termed the *last closed flux surface* or LCFS. With sufficient shaping, the operator may generate a null point, the *X-point*, in the LCFS where the poloidal field is zero, splitting the LCFS (also called the *separatrix* in such configurations) into a minimally open surface with “legs” contacting the wall. This magnetic configuration is illustrated in fig. 1.6, along with a diagram defining the typical plasma shaping parameters: elongation  $\kappa$  and upper and lower triangularity  $\delta_u$ ,  $\delta_l$ . As the plasma diffuses outwards, it eventually crosses the LCFS and enters open flux surfaces in the *scrape-off layer* (SOL). The plasma then streams freely along these open magnetic field lines until it contacts the wall. By maintaining an X-point, the operator may steer this plasma exhaust into a section of the tokamak, the *divertor* [23, 24, 25], that is designed to handle this high heat flux – a necessary feature to handle reactor-scale exhaust in a tokamak.

### 1.3 ALCATOR C-MOD

The data presented in this thesis were collected on the Alcator C-Mod tokamak [26, 27] at the MIT Plasma Science and Fusion Center. The Alcator tokamak experiments were designed as compact, high-field tokamaks. Despite its small physical size (67 cm major radius, 22 cm minor radius, considerably smaller than other major experiments), Alcator C-Mod plasmas are capable of approaching ITER- and reactor-relevant densities ( $> 1 \times 10^{20} \text{ m}^{-3}$ ) and pressures ( $> 1 \text{ atm}$ ). This compact design is enabled by a very high toroidal magnetic field driven by liquid-Nitrogen-cooled copper coils, reaching as high as 8.1 T, with typical operation near 5.5 T, allowing reactor-relevant research in a small, cost-effective machine. C-Mod plasmas are primarily heated by RF heating in the ion-cyclotron range of frequencies (ICRF) [28], with up to 6 MW of heating power, with an additional  $\sim 1 \text{ MW}$  of lower-hybrid resonance (LHRF) power used for heating and non-inductive current drive [29], providing exceptionally high power density in the  $\sim 1.1 \text{ m}^3$  plasma. A cutaway view of C-Mod, including support structures and the concrete “igloo” housing the



**Figure 1.7:** Cutaway view of the Alcator C-Mod tokamak, including cryostat and ancillary structures, illustrating the extensive support structures necessary for compact, high-field operation.

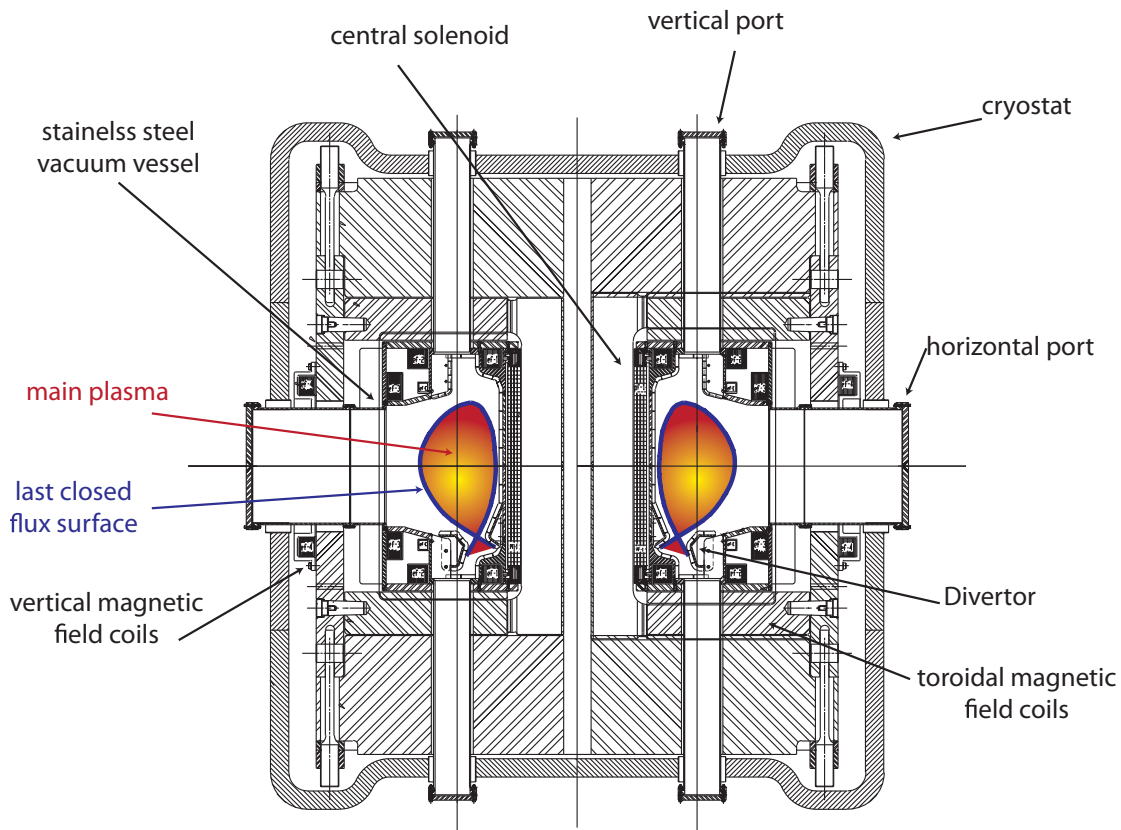


**Figure 1.8:** Cross-section of the C-Mod vacuum vessel, cryostat and diagnostic access ports, with toroidal-field and equilibrium-field magnetic coils labeled. Also shown is the plasma position in a typical LSN shape, with strike points in the lower divertor shown..

cooling systems, is visible in fig. 1.7. A detailed and annotated view of the C-Mod cross-section is shown in fig. 1.8.

Due to their high plasma pressure and power density, C-Mod plasmas must exhaust a large heat flux, reaching levels comparable to that anticipated for ITER [30, 31, 32]. To handle this heat flux, C-Mod operates entirely with high-Z metal materials (primarily Molybdenum and Tungsten) for all plasma-facing surfaces. In addition to its high heat tolerance and low erosion rates due to plasma contact, metal walls provide relatively low retention of fuel gas at the edge – metal walls are thus the leading candidate for ITER- and reactor-scale plasma-facing components.

The presence of a full high-Z lower divertor and upper strike plate, as well as metal limiter walls, gives C-Mod great flexibility in attainable plasma shapes – plasmas may be run in a lower-single null (LSN) shape with the plasma exhaust striking the lower divertor (shown in fig. 1.8, upper-single null (USN) ex-

**Table 1.1:** Summary of Alcator C-Mod typical operating parameters.

parameter	range
major radius	0.67 m
minor radius	0.22 m
toroidal field	3 – 8.1 T
plasma current	$\leq 2$ MA
plasma density	$\leq 5 \times 10^{20} \text{ m}^{-3}$
central temperature	$\leq 8$ keV
plasma pressure	$\leq 2$ atm
ICRF power	6 MW
LHFR power	1 MW

hausting into the upper strike plate, or in a limited shape where the scrape-off layer directly impinges on the plasma-facing wall. •

## 1.4 CONFINEMENT & TRANSPORT

### 1.4.1 Global Confinement

The rate at which a fusion plasma bleeds off heat is described by a characteristic time scale, the energy confinement time  $\tau_E$ . From basic power balance for the total plasma stored energy  $W_p$ ,

$$\frac{dW_p}{dt} = P_{in} - P_{out} = P_{tot} - \frac{W_p}{\tau_E} \quad (1.25)$$

where  $P_{in} = P_{tot}$  is the total input heating power, from Ohmic heating  $P_{Ohm} = I_p^2 R_{plasma}$ , RF or beam auxiliary heating power  $P_{aux}$ , or self-heating of the plasma from fusion reactions. In the case of the latter, note that as fusion neutrons are immediately lost into the blanket, only the energy carried by *charged* fusion products contributes to fusion self-heating: in the case of D – T fusion we denote this as the alpha heating power  $P_\alpha = 1/5 \times P_{fusion}$  for the energy carried by the  ${}^4\text{He}$  nucleus. It is common to encapsulate these heat source and sink terms into a single “loss” power,

$$P_{loss} = P_{Ohm} + P_{aux} + P_{fusion} - \frac{dW_p}{dt} = P_{tot} - \frac{dW_p}{dt} \quad (1.26)$$

While  $P_{loss}$  is commonly used as a parameter of merit for confinement studies, it is also important to account for the radiated power  $P_{rad}$ , the heat loss due to radiative (primarily Bremsstrahlung) rather than transport-driven effects encoded by  $W_p/\tau_E$ . This is expressed in the net power,

$$\begin{aligned} P_{net} &= P_{Ohm} + P_{aux} + P_{fusion} - P_{rad} - \frac{dW_p}{dt} \\ P_{net} &= P_{loss} - P_{rad} \end{aligned} \quad (1.27)$$

The radiative power loss is commonly difficult to consistently determine experimentally, and is only partially subject to operator control, as the radiation is due both to intrinsic impurities from plasma-facing materials and intentionally-introduced high-Z impurities for radiation control. As such,  $P_{loss}$  is typically used for a simply relation for the experimental energy confinement time,

$$\tau_E = \frac{W_p}{P_{loss}} \quad (1.28)$$

Nevertheless an understanding of the radiated power is necessary for reactor operation. Radiated power from the core is deleterious to performance, driving decreased  $\tau_E$  at higher radiated-power fractions  $P_{\text{rad}}/P_{\text{tot}}$  [33]. Edge radiation, conversely, is essential for reactor operation to reduce the heat loads incident on the divertor, with edge radiated power fractions in excess of 50% predicted to be necessary for ITER [30]. In practice, the physics determining energy confinement are extremely complex; as such, working models for calculating  $\tau_E$  from bulk parameters typically require an empirical power-law scaling.

A closer examination of the power balance equation, eq. (1.25), reveals an important figure of merit. For a DT-burning fusion reactor, steady-state operation with plasma temperatures sustained by fusion self-heating (termed “ignition”) is highly desirable. At these conditions, the heating power is dominated by  $P_\alpha$ ; for steady-state operation ( $dW_p/dt \rightarrow 0$ ), eq. (1.25) reduces to

$$\frac{W_p}{\tau_E} = P_\alpha \quad (1.29)$$

The alpha heating power is simply the fusion reaction rate  $R_f = n_D n_T \langle \sigma v \rangle_{DT}$  times the energy carried by charged particles from a single reaction,  $E_\alpha = 1/5 \times E_{\text{fusion}} = 3.5 \text{ MeV}$ . Quasineutrality (eq. (1.2)) requires  $n_e \approx n_D + n_T$ . As the reaction rate is optimized for a 50-50 fuel mix, the alpha heating power is given by

$$P_\alpha = \frac{1}{4} n_e^2 \langle \sigma v \rangle E_\alpha \quad (1.30)$$

The stored energy is defined by

$$W_p = \frac{3}{2} p_{\text{thermal}} \quad (1.31)$$

with the thermal pressure in the plasma given by

$$p_{\text{thermal}} = n_e T_e + n_D T_D + n_T T_T = 2n_e T_e \quad (1.32)$$

assuming the condition above on the electron and ion densities, and assuming temperature equilibration  $T_e \approx T_D \approx T_T$ . This, then, implies  $W_p = 3n_e T_e$  (a convenient expression, as electron quantities are typically more readily measured in plasma experiments). Power balance at ignition then requires

$$\frac{3n_e T_e}{\tau_E} = \frac{1}{4} n_e^2 \langle \sigma v \rangle E_\alpha \quad (1.33)$$

thus simplifying to the Lawson Criterion [34]

$$n_e \tau_E = \frac{12 T_e}{\langle \sigma v \rangle E_\alpha} \quad (1.34)$$

Multiplying both sides by  $2T_e$  gives the “triple product,”

$$2n_e T_e \tau_E = p \tau_E = \frac{24 T_e^2}{\langle \sigma v \rangle E_\alpha} \quad (1.35)$$

an important figure of merit for a reactor that is optimized for D – T fusion at  $T_e \approx 15$  keV with a value of  $p \tau_E \approx 8.3$  atm · s, setting target parameters for a fusion reactor [15].

However, the maximum attainable thermal pressure in a tokamak is limited by a global MHD stability limit expressed in terms of [7, § 6.16]

$$\beta = \frac{2\mu_0 p}{B^2} \quad (1.36)$$

the ratio of thermal pressure to magnetic pressure  $B^2/2\mu_0$  (equivalently, the ratio of thermal and magnetic stored energy) – a normalization that also falls naturally out of solutions to the MHD equilibrium, eq. (1.19). Thus for a given  $B_T$ , set by design and operational limits, there is a maximum obtainable pressure, necessitating increased energy confinement – that is, higher values for  $\tau_E$  – to reach the triple-product target for ignition.

#### 1.4.2 Transport Barriers

Global improvement to energy confinement may be achieved through local modification of the transport of energy or particles out of the plasma, achieved via regions termed *transport barriers*. While the physics driving the formation of transport barriers is not entirely understood, the effect is evidently caused by sheared flows in the plasma – these break up the turbulent “eddies” driving much of the energy or particle transport through the plasma, locally reducing transport drive in the sheared region.

The effect on the transport is clearly evident from a diffusive transport model, given by

$$\frac{\partial Q}{\partial t} = \nabla \cdot (D_Q \nabla Q) + R_Q \quad (1.37)$$

for a general parameter  $Q(\vec{x}, t)$  with accompanying diffusion coefficient  $D_Q(Q, \vec{x}, t)$  and net source/sink term  $R_Q(Q, \vec{x}, t)$ . We may con-

sider a one-dimensional “toy model” of diffusion with a simple constant source term, given in steady state by

$$\frac{d}{dx} \left( D_Q \frac{dQ}{dx} \right) + R_Q = 0 \quad (1.38)$$

The solution to this model for two sample diffusion coefficients is given in fig. 1.9. A simple constant diffusion coefficient  $D_Q$  produces a profile with weak slope, whereas an order-of-magnitude drop in  $D_Q$  near the edge (consistent with experimentally-observed values of diffusion coefficients in transport barriers) produces a region with a steep gradient in  $Q$  compared to the flat- $D_Q$  solution, despite identical source terms  $R_Q$ . Experimentally, reductions in the particle transport coefficient  $D_n$  or the heat transport coefficient  $\chi$  due to sheared flows correspond to steep-gradient regions in density or temperature, characteristic of the transport barrier.

Of particular interest is the *edge transport barrier*, also termed the *pedestal* [33, 35]. A number of high-performance tokamak regimes have been established, exploiting the formation of a pedestal to suppress transport and boost global energy confinement to levels necessary to reach the triple-product target (eq. (1.35)) for an ignited plasma. The understanding of these high-performance regimes, commonly referred to as “high-confinement” or H-modes, and their extrapolation to ITER and reactor-scale devices has been a major focus of recent tokamak research.

However, the formation of the pedestal also presents challenges that must be addressed for reactor-scale operation. Increased particle confinement causes the plasma to retain impurities – particularly ionized wall materials – along with fuel ions. Low-Z impurities, particularly the  ${}^4\text{He}$  “fusion ash”, tend to slow the fusion reaction rate due to fuel dilution, while high-Z impurities drive elevated radiative losses (note the strong charge dependence for Bremsstrahlung radiation, eq. (1.6)). This ultimately leads to a *radiative collapse* [27, 33], dropping the plasma out of H-mode – thus, stationary (i.e., non-transient) operation in H-mode requires a means to regulate particle confinement and flush impurities from the plasma core.

The steep gradient in the plasma pressure generated in the pedestal has been shown to drive *Edge-Localized Modes* (ELMs) [36], instabilities

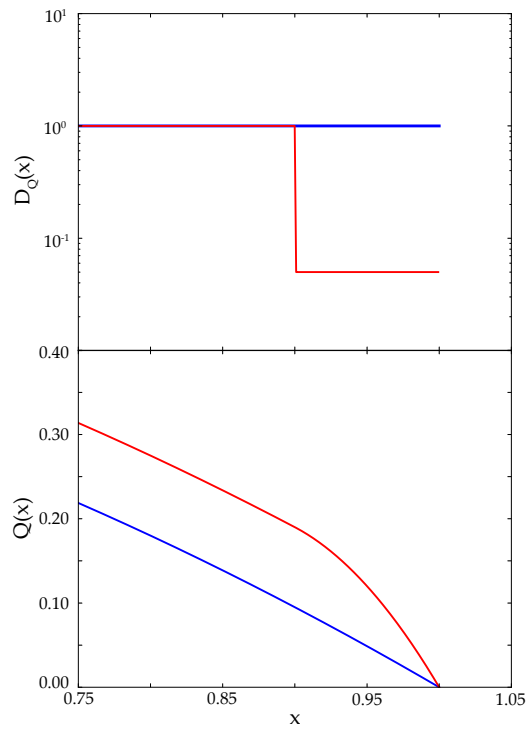


**Figure 1.9:** Diffusion coefficients and plasma profiles for a “toy model” 1D diffusion equation with a general parameter  $Q(x)$  and accompanying diffusion coefficient  $D_Q(x)$ .

that cause the pedestal to periodically “crash,” expelling particles and energy into the scrape-off layer. The smaller ELM bursts found in existing experiments provide the desired level of particle transport for stationary operation – thus ITER operation is designed considering an H-mode with ELMs as the baseline for operation [37, 38]. However, on ITER-scale devices the heat pulses from ELMs drive unacceptable levels of transient thermal loading and erosion damage to wall and divertor materials [39, 40]. As such, high-performance operation on ITER- or reactor-scale devices requires mitigation or elimination of large, deleterious ELMs, either through externally-applied controls or physics-based stabilization.

### 1.5 GOALS & OUTLINE

This thesis will present results in the *I-mode*, a novel high-performance regime pioneered on Alcator C-Mod. I-mode is notable for its apparent decoupling of energy and particle transport, reaching H-mode-like energy confinement while maintaining L-mode levels of particle and impurity transport, achieving the desired flushing of impurities from the plasma. This is manifested in the edge with the formation of an H-mode-like temperature pedestal without the accompanying density pedestal found in conventional H-modes. I-mode also appears to be naturally free of large ELMs, avoiding the need for complex externally-applied controls, and to exhibit highly favorable scalings of energy confinement with heating power.

A firm understanding of the structure and stability of the pedestal is essential to extend I-mode operation to larger devices. This thesis will describe a combined approach to the understanding of the pedestal in I-mode, using both direct observations of pedestal structure and numerical modeling of the pedestal stability against MHD triggers for large, deleterious ELMs. The applicability of I-mode to reactor operation can thereby be evaluated. The balance of this thesis is arranged as follows:

#### CHAPTER 2: HIGH-PERFORMANCE REGIMES

An overview of existing results in established H-mode regimes, including observed pedestal behaviors. A detailed introduction to I-mode physics and operation is also included.

#### CHAPTER 3: PEDESTAL MODELING AND THEORY

An introduction to the theory of the MHD and turbulent instabilities governing the pedestal and driving large ELMs, and the numerical modeling approaches used in their analysis.

#### CHAPTER 4: ELMY H-MODES ON C-MOD

The results of recent experiments on C-Mod testing a unified model for pedestal structure in ELMy H-mode, the approach to which is also applied to I-mode pedestals.

**CHAPTER 5: I-MODE PEDESTAL SCALINGS**

New results from dedicated pedestal experiments in I-mode examining the response of pedestal structure to engineering and physics parameters, and potential extrapolations of pedestal structure and performance to larger devices.

**CHAPTER 6: I-MODE PEDESTAL STABILITY MODELING**

Numerical modeling results for the stability of I-mode pedestals against identified ELM triggers, and correlations to the generally observed lack of ELMs in I-mode.

**CHAPTER 7: CONCLUSIONS**

A summary of the results presented in this thesis and some directions for future work.

An overview of the diagnostics used in the experiments presented here is also given in appendix A. A summary of the pedestal database used in these experiments is given in appendix B. ★



## BIBLIOGRAPHY

---

- [1] United Nations. *World Population Prospects: The 2010 Revision. Comprehensive Tables*, volume 1. United Nations, 2010.
- [2] J. Klugman et al. *Human development report 2011. Sustainability and Equity: A Better Future for All*, 2011.
- [3] H. Gruenspecht. *International energy outlook 2011. Center for Strategic and International Studies*, 2010.
- [4] B.P. Global. *Statistical review of world energy 2010*.
- [5] U.S. Energy Information Administration. *Annual coal report 2012*, 2013.
- [6] J.P. Freidberg. *Plasma Physics and Fusion Energy*. Cambridge books online. Cambridge University Press, 2007.
- [7] J. Wesson. *Tokamaks*. International Series of Monographs on Physics. Oxford University Press, 2011.
- [8] F.F. Chen. *Introduction to Plasma Physics and Controlled Fusion*. Springer, 1984.
- [9] K.S. Krane. *Introductory Nuclear Physics*. Wiley, 1987.
- [10] W.M. Haynes. *CRC Handbook of Chemistry and Physics, 93rd Edition*. Taylor & Francis, 2012.
- [11] Jeffrey R. Johnson, Timothy D. Swindle and Paul G. Lucey. *Estimated solar wind-implanted helium-3 distribution on the moon*. *Geophysical Research Letters*, 26(3):385–388, 1999.
- [12] B. Palaszewski. *Atmospheric mining in the outer solar system*. In *41st American Institute of Aeronautics and Astronautics Joint Propulsion Conference and Exhibit*, 2005.
- [13] Jeffrey P. Freidberg. *Ideal Magnetohydrodynamics*. Springer, 1987.
- [14] J. Kesner, R.S. Post, B.D. McVey and D.K. Smith. *A tandem mirror with axisymmetric central-cell ion confinement*. *Nuclear Fusion*, 22(4):549, 1982.
- [15] Dale Meade. *50 years of fusion research*. *Nuclear Fusion*, 50(1):014004, 2010.
- [16] Egbert Westerhof. *Non-inductive current drive*. *Fusion Science and Technology*, 61:312–319, 2012.

- [17] Paul T. Bonoli. **Review of recent experimental and modeling progress in the lower hybrid range of frequencies at ITER relevant parameters.** *AIP Conference Proceedings*, 1580(1):15–24, 2014.
- [18] R. Prater. **Heating and current drive by electron cyclotron waves.** *Physics of Plasmas*, 11(5):2349–2376, 2004.
- [19] C. Gormezano, A.C.C. Sips, T.C. Luce, S. Ide, A. Becoulet et al. **Chapter 6: Steady state operation.** *Nuclear Fusion*, 47(6):S285, 2007.
- [20] H. Grad and H. Rubin. MHD equilibrium in an axisymmetric toroid. In *Proceedings of the 2nd U.N. Conference on the Peaceful Uses of Atomic Energy*, volume 31, page 190, 1958.
- [21] V.D. Shafranov. Grad-Shafranov equation for MHD equilibrium in a torus. *Soviet Physics, Journal of Experimental and Theoretical Physics*, 26:682, 1960.
- [22] L.L. Lao, H. St. John, R.D. Stambaugh, A.G. Kellman and W. Pfeiffer. **Reconstruction of current profile parameters and plasma shapes in tokamaks.** *Nuclear Fusion*, 25(11):1611, 1985.
- [23] B. Lipschultz, X. Bonnin, G. Counsell, A. Kallenbach, A. Kukushkin et al. **Plasma–surface interaction, scrape-off layer and divertor physics: implications for ITER.** *Nuclear Fusion*, 47(9):1189, 2007.
- [24] B. Lipschultz, B. LaBombard, J. L. Terry, C. Boswell and I. H. Hutchinson. **Divertor physics research on Alcator C-Mod.** *Fusion Science and Technology*, 51:369–380, 2007.
- [25] P. Titus, R. Vieira, B. LaBombard, B. Lipschultz, S. Wolfe et al. **Conceptual design of a new outer divertor for C-Mod.** *Fusion Science and Technology*, 56(1):101–106, 2009.
- [26] I. H. Hutchinson, R. Boivin, F. Bombarda, P. Bonoli, S. Fairfax et al. **First results from Alcator C-Mod.** *Physics of Plasmas*, 1(5):1511–1518, 1994.
- [27] M. Greenwald, N. Basse, P. Bonoli, R. Bravenec, E. Edlund et al. **Confinement and transport research in Alcator C-Mod.** *Fusion Science and Technology*, 51(3):266–287, 2007.
- [28] Y Takase, R L Boivin, F Bombarda, P T Bonoli, C L Fiore et al. **Survey of ICRF heating experiments and enhanced performance modes in Alcator C-Mod.** *Plasma Physics and Controlled Fusion*, 38(12):2215, 1996.
- [29] J.R. Wilson, R. Parker, M. Bitter, P.T. Bonoli, C. Fiore et al. **Lower hybrid heating and current drive on the Alcator C-Mod tokamak.** *Nuclear Fusion*, 49(11):115015, 2009.

- [30] A. Loarte, B. Lipschultz, A.S. Kukushkin, G.F. Matthews, P.C. Stangeby et al. **Chapter 4: Power and particle control.** *Nuclear Fusion*, 47(6):S203, 2007.
- [31] J. L. Terry, B. LaBombard, B. Lipschultz, M. J. Greenwald, J. E. Rice et al. **The scrape-off layer in Alcator C-Mod: Transport, turbulence, and flows.** *Fusion Science and Technology*, 51(3):342–356, 2007.
- [32] B. LaBombard, J. L. Terry, J. W. Hughes, D. Brunner, J. Payne et al. **Scaling of the power exhaust channel in Alcator C-Mod.** *Physics of Plasmas*, 18(5):056104, 2011.
- [33] M. Greenwald, R.L. Boivin, F. Bombarda, P.T. Bonoli, C.L. Fiore et al. **H-mode confinement in Alcator C-Mod.** *Nuclear Fusion*, 37(6):793, 1997.
- [34] J D Lawson. **Some criteria for a power producing thermonuclear reactor.** *Proceedings of the Physical Society. Section B*, 70(1):6, 1957.
- [35] F. Wagner, G. Becker, K. Behringer, D. Campbell, A. Eberhagen et al. **Regime of improved confinement and high beta in neutral-beam-heated divertor discharges of the ASDEX tokamak.** *Physical Review Letters*, 49(19):1408–1412, Nov 1982.
- [36] H Zohm. **Edge localized modes (ELMs).** *Plasma Physics and Controlled Fusion*, 38(2):105, 1996.
- [37] ITER Physics Expert Group on Confinement, Transport and ITER Physics Expert Group on Confinement Modelling and Database and ITER Physics Basis Editors. **Chapter 2: Plasma confinement and transport.** *Nuclear Fusion*, 39(12):2175, 1999.
- [38] M. Shimada, D.J. Campbell, V. Mukhovatov, M. Fujiwara, N. Kirneva et al. **Chapter 1: Overview and summary.** *Nuclear Fusion*, 47(6):S1, 2007.
- [39] A Loarte, G Saibene, R Sartori, D Campbell, M Becoulet et al. **Characteristics of type I ELM energy and particle losses in existing devices and their extrapolation to ITER.** *Plasma Physics and Controlled Fusion*, 45(9):1549, 2003.
- [40] G Federici, A Loarte and G Strohmayer. **Assessment of erosion of the ITER divertor targets during type I ELMs.** *Plasma Physics and Controlled Fusion*, 45(9):1523, 2003.



# 2

## HIGH-PERFORMANCE REGIMES

---

The development of magnetic-confinement fusion into an economical form of power generation is characterized by two seemingly contrary requirements: first, a high level of energy confinement is necessary to reach the desired level of self-heating of the plasma by fusion products, satisfying triple-product requirements (eq. (1.35)). At the same time, particle transport must be sufficient to avoid the deleterious effects of accumulated helium “fusion ash” and other impurities on fusion performance – particularly important in the case of the high-Z impurities from the metal plasma-facing walls necessary for reactor-scale devices [1].

A number of operating scenarios, collectively termed “high confinement” or H-modes[2, 3], satisfying these requirements have been developed. The “low confinement” or L-mode operating baseline of energy confinement is characterized through an extensive multi-machine scaling study [4] by the ITER-89 scaling,

$$\tau_{E,ITER89} = 0.048 \times \bar{n}_e^{0.1} M^{0.5} I_p^{0.85} R^{1.2} a^{0.3} \kappa^{0.5} B_T^{0.2} P_{aux}^{-0.5} \quad (2.1)$$

in which  $\bar{n}_e$  is the line-averaged density ( $10^{20} \text{ m}^{-3}$ ),  $M$  is the atomic mass (amu),  $I_p$  is the plasma current (MA),  $B_T$  is the toroidal field (T),  $R$  and  $a$  are the major and minor radii in m (see fig. 1.4),  $\kappa$  is the elongation (see fig. 1.6), and  $P_{aux}$  is the externally-applied heating power (MW). Compared to this baseline, H-modes represent a significant improvement in performance, with confinement – here represented in a normalized sense by the H-factor, i.e.,

$$H_{89} = \frac{\tau_E}{\tau_{E,ITER89}} \quad (2.2)$$

improved by roughly a factor of two compared to L-mode [5].

This improvement in confinement is due to the formation of a *pedestal*, a transport barrier (see section 1.4.2) at the edge that greatly slows the transport of particles and/or energy out of the plasma, and accordingly forms a steep-gradient region in density and/or temperature at the edge. Pedestal formation is achieved through strongly sheared flows in the plasma edge, driven in part by a radial electric field (the “ $E_r$  well”) and the resulting  $\vec{E} \times \vec{B}$  flows in the pedestal. While this flow is difficult to model due to the short scale lengths inherent to the pedestal [6, 7], the role of edge  $E_r$  and flows has been extensively studied both from an experimental [8, 9, 10, 11] and a the-

oretical [12, 13, 14, 15, 16] standpoint, as has the role of other edge fluctuations coupling into these flows in driving the transition into H-mode [17]. As the pedestal structure is known to set a strong constraint on the overall performance in high-confinement regimes [18], as well as determining the edge stability and heat exhaust properties of the regime, a firm understanding of the pedestal is essential for extrapolation of a high-performance regime to ITER and beyond.

This chapter provides an overview and comparison of different classes of established H-mode operation, particularly regarding their behaviors in the high energy confinement and low particle confinement required for a reactor. Additionally, observations of Edge-Localized Modes (ELMs) [19] are addressed. We then introduce the access conditions, operation, and global characteristics of *I-mode* – an alternate high-performance regime with a number of favorable characteristics for reactor operation, and the subject of the majority of this thesis.

**Table 2.1:** Typical operating parameters of tokamaks noted in this thesis, along with references to overviews of each machine. Note: all ITER values are projected.[check all values here](#)

Device	R/a [m]	I <sub>p</sub> [MA]	B <sub>T</sub> [T]	⟨n <sub>e</sub> [10 <sup>19</sup> m <sup>-3</sup> ]	T <sub>e0</sub> [keV]	refs.
C-Mod (USA)	0.67/0.22	≤ 2	3 – 8.1	≤ 50	≤ 8	[20, 21, 22]
DIII-D (USA)	1.67/0.67	1 – 3	2.2	6	5 – 10	[23, 24, 25]
ASDEX-U (GER)	1.65/0.5	~ 1	3.9	7.5	2 – 3	[26, 27, 28]
JET (UK)	3.4/0.9	3 – 4	3.8	5	10 – 20	[29, 30]
JT-60U (JAP)	3.4/0.9	3 – 4	4.8	5	10 – 20	[31, 32]
JFT-2M (JAP)	1.3/0.35	0.5	2.2	5	1 – 2	[33, 34]
ITER*	6.2/2.0	15	5.3	10	10	[35, 36, 37]

## 2.1 ELM-FREE H-MODE

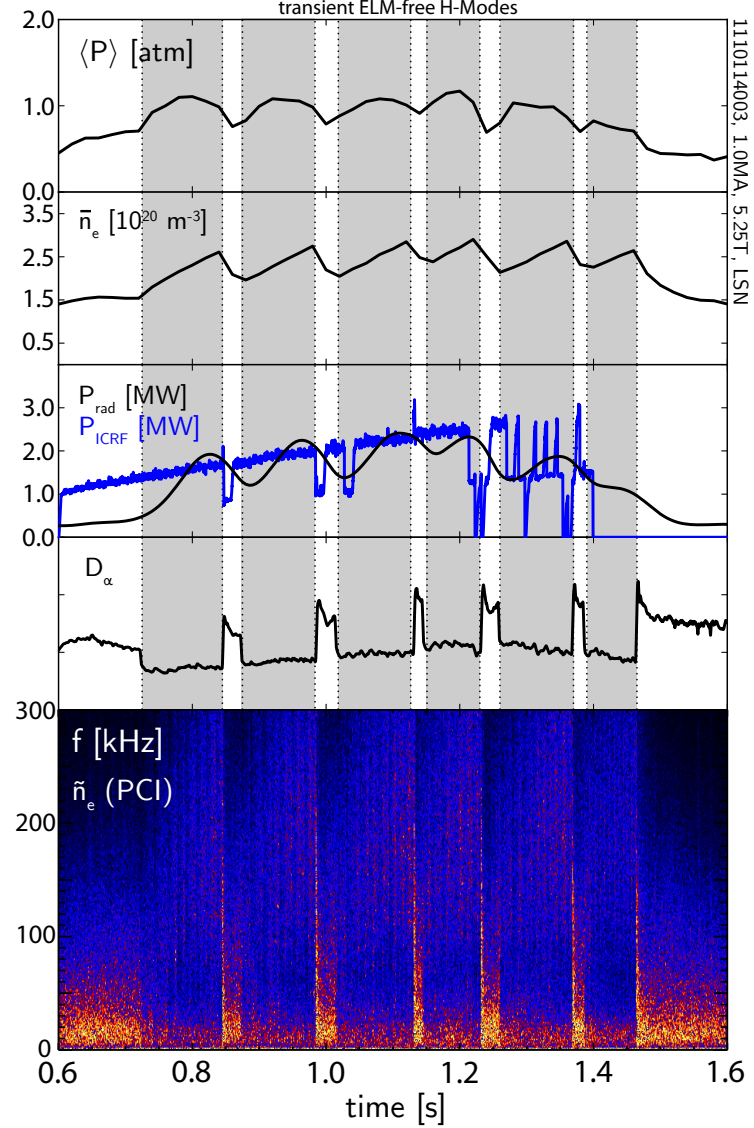
At moderate levels of heating power above the L-H threshold [38],

$$P_{\text{thres}} = 0.0488 \times \bar{n}_e^{0.717} B_T^{0.803} S^{0.941} \quad [\text{MW}]$$

$$S = (2\pi)^2 a R \sqrt{\kappa} \quad (2.3)$$

(⟨n<sub>e</sub> is the line-averaged density in 10<sup>20</sup> m<sup>-3</sup>, B<sub>T</sub> in T, and S is the plasma surface area in m<sup>2</sup>) the plasma enters a transient *ELM-free H-mode*, in which an H-mode forms without exhibiting large edge-localized modes (ELMs) [19, 39]. ELM-free H-modes exhibit high levels of both energy and particle confinement (H<sub>89</sub> ~ 2), resulting in strong density and temperature pedestals [40, 41]. The plasma stored energy, global pressure, and density rise monotonically after the L-H transition (shown in fig. 2.1), as does the edge pressure gradient [42]. This, however, is unsustainable – the increased particle confinement

**Figure 2.1:** Characteristic traces of transient ELM-free H-modes, highlighted on the traces (section 2.1). After the L-H transition, density and thermal pressure (and therefore fusion reaction rate and stored energy) rise, while turbulent particle transport is reduced, as seen by the drop in edge  $D_\alpha$  light and suppression of turbulence. However, radiated power rises due to impurity accumulation – when radiated power reaches a level comparable to total heating power, the plasma drops back into L-mode.



causes impurities to accumulate in the plasma, increasing the power lost to radiative effects. Above  $P_{\text{rad}}/P_{\text{in}} \sim 0.5$  confinement degrades due to cooling at the edge, and the H-mode terminates as the radiated power approaches the total heating power, an event termed the “radiative collapse” [5].

As a result, the conventional ELM-free H-mode is an inherently transient state for the plasma – the excessive particle confinement and resulting radiative losses tend to drop the plasma back into L-mode, although under certain conditions the edge pressure gradient may grow sufficiently to instead transition into an ELMy H-mode [42]. This demonstrates the necessity of some form of density regulation in high-performance regimes to control and flush impurities from the plasma, allowing stationary operation. ●

## 2.2 ELMY H-MODE

### 2.2.1 ELMY H-Mode Operation

The first H-modes, observed in high-power experiments on ASDEX [2, 3], exhibited a prompt decrease by roughly a factor of two in both particle and energy transport [2]. The H-mode transition is marked by high edge temperatures and strong gradients – the first H-modes were observed in divertor experiments on ASDEX, as the diverted configuration allows higher edge temperatures than are attainable in limited plasmas [3]. Unlike ELM-free H-modes, however, the confinement is periodically degraded by *Edge-Localized Modes* (ELMs), intermittent “crashes” in the pedestal expelling particles and energy into the SOL, with repetition rates ranging from a few ELM cycles per second to over 100 Hz, which drives sufficient particle transport to flush impurities from the plasma and allow stationary operation [3, 19]. The ELMY H-mode forms a strong pedestal in both density and temperature, although at lower electron-ion coupling rates the ion pedestal may be wider [43] – due to profile stiffness in the core, this supports high temperatures and pressures and good global performance [5, 44, 45]. Moreover, the ELMY H-mode is readily attainable on all major tokamak experiments, although ELMY H-modes on C-Mod require an atypical shape [46, 47], as well as at a broad range of collisionalities and operating densities. Here we define the collisionality (normalized collision frequency) by [48],

$$\begin{aligned} \nu^* &= \frac{\nu_{\text{eff}}}{\nu_{\text{bounce}}} = \frac{qR\nu_{ei}}{\varepsilon^{3/2}\nu_{Th,e}} \\ &= (6.921 \times 10^{-18}) \frac{Rqn_e Z_{\text{eff}} \ln \Lambda_e}{\varepsilon^{3/2} T_e^2} \end{aligned} \quad (2.4)$$

with electron density  $n_e$  in  $\text{m}^{-3}$  and temperature in eV, major radius  $R$  in m, and with the Coulomb logarithm defined by  $\ln \Lambda_e = 24 - \ln(\sqrt{n_e}/T_e)$ . Typically the pedestal collisionality is calculated by evaluating  $n_e$ ,  $T_e$ , and  $q$  at the 95% flux surface. The operating density range is expressed in terms of the Greenwald density limit [49],

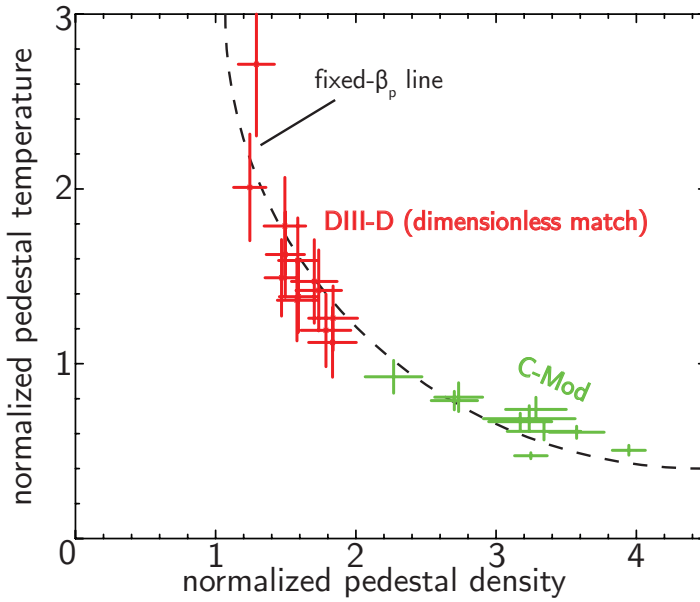
$$n_{Gr} = \frac{I_p}{\pi a^2} \quad f_{Gr} = \frac{\bar{n}_e}{n_{Gr}} \quad (2.5)$$

with  $I_p$  in MA and  $a$  in m yielding density in  $10^{20} \text{ m}^{-3}$ . ELMY H-mode operation is possible with Greenwald fractions ranging from  $f_{Gr} \sim 0.3 - 1.0$ , although confinement degrades severely as  $f_{Gr}$  approaches unity [50]. As such, the ELMY H-mode is considered the baseline for ITER operation [35, 36]. Analysis of a multi-machine

**Figure 2.2:** Characteristic traces of a steady ELMy H-mode (section 2.2). Density and radiated power rise after the L-H transition, but stabilize as the periodic relaxation of the pedestal regulates and flushes impurities from the plasma. ELM bursts are visible as spikes on the edge D<sub>α</sub> signal.



**Figure 2.3:** ELMy H-mode pedestals from experiments on Alcator C-Mod and DIII-D, with matched dimensionless parameters between the two machines **elaborate on matching?**. Pedestal densities and temperatures are shown normalized to poloidal field (which accounts for differences in plasma current) such that hyperbolae in the parameter space are curves of constant poloidal beta. In the dimensionless match, ELMy H-mode pedestals are, to lowest order, constrained to a curve of fixed  $\beta_{p,\text{ped}}$ .



database [51] led to the development of the ITER98y2 H-mode confinement scaling [36],  
check  $P_{\text{net}}$  vs  $P_{\text{loss}}$

$$\tau_{\text{ITER98y2}} = 0.0562 \times \bar{n}_e^{0.41} M^{0.19} I_p^{0.93} R^{1.39} a^{0.58} \kappa^{0.78} B_T^{0.15} P_{\text{net}}^{-0.69} \quad (2.6)$$

$$H_{98} = \frac{\tau_E}{\tau_{E,\text{ITER98y2}}} \quad (2.7)$$

in which  $\bar{n}_e$  is the line-averaged density ( $10^{19} \text{ m}^{-3}$ ),  $M$  is the atomic mass (amu),  $I_p$  is the plasma current (MA),  $B_T$  is the toroidal field (T),  $R$  and  $a$  are the major and minor radii in m (see fig. 1.4),  $\kappa$  is the elongation (see fig. 1.6), and  $P_{\text{net}}$  is the net heating power defined in eq. (1.27) (MW).

Due to the importance of pedestal structure on overall performance [18], a number of models for the pedestal width and height in ELM My H-mode have been proposed. The ELM My H-mode pedestal has been observed to be limited in pressure gradient [52, 53] – as the pedestal width on a given machine typically varies only over a small range [45, 54], this constitutes (to lowest order approximation) a limit on the attainable pedestal height. Models based on gyroradius limits, and their expected effects on the growth rates of turbulent modes compared to the  $\vec{E} \times \vec{B}$  shearing rate, have been proposed [43, 55]. However, this has been discounted in favor of a model based on poloidal beta limits,  $\beta_p = 2\mu_0 p/B_p^2$ , both by experiments varying density and temperature at fixed  $p_{\text{ped}}$  [56] and by isotope-mass-difference experiments [57] (both of which vary the gyroradius without varying  $\beta_{p,\text{ped}}$ ). These models are described in more detail in ??.

On smaller machines, ELMs provide sufficient impurity transport to allow stationary operation without seriously impacting energy confinement [58]. However, the transient power load from the ELM heat pulse is consistently observed to be 20 – 30% of the input heating power [59], resulting in ELM energy losses reaching 2 – 6% of the total stored energy – on ITER, this results in heat pulses as high as 80 MJ reaching the divertor plate [44, 60]. As wall materials are generally limited to ELM heat loads of  $\sim 10 \text{ MJ}$  per ELM [61], uncontrolled large ELM pulses can seriously exceed tolerances for ITER plasma-facing wall and divertor materials [61, 62]. Thus, avoiding or mitigating large, deleterious ELMs is essential for ITER operation.

### 2.2.2 Edge-Localized Modes & Pedestal Limits

Early phenomenological experiments on DIII-D and ASDEX [19, 44, 52] classified ELMs into three broad categories:

#### TYPE-I

Large, discrete ELMs. Repetition rate  $f_{\text{ELM}}$  rises with increasing

heating power. The ELM crash is preceded by broadband electromagnetic and density fluctuations. Type-I ELMy pedestals are modeled to be at or near the ballooning stability boundary (described below).

#### TYPE-II

Smaller and faster than type-I, often termed “grassy ELMs.” No discernable  $f_{\text{ELM}}$  dependence on heating power. Found in strongly shaped plasmas between the first and second-stable regions for ballooning MHD.

#### TYPE-III

Small ELMs,  $f_{\text{ELM}}$  decreases with increasing heating power. Exhibit a coherent magnetic precursor fluctuation before the ELM crash. Found only below a threshold pedestal temperature.

Early investigation of the ELMy pedestal, particularly in large type-I ELMs, associated the pedestal limit with a “ballooning” MHD instability – these MHD modes are driven unstable by strong pressure gradients in the edge, expressed in terms of the parameter  $\alpha_{\text{MHD}}$  for a general toroidal equilibrium [63],

$$\alpha_{\text{MHD}} = -\frac{2}{(2\pi)^2} \frac{\partial V}{\partial \psi} \sqrt{\frac{V}{2\pi^2 R}} \mu_0 \frac{dp}{d\psi} \quad (2.8)$$

This reduces to a more intuitive form for a cylindrical plasma [64],

$$\alpha_{\text{MHD}} = -\frac{2Rq^2}{B_T^2} \nabla p \quad (2.9)$$

with the  $q^2/B_T^2$  factor effectively expressing the scaling as  $\alpha_{\text{MHD}} \sim \nabla p/B_p^2$ . Type-I ELMy H-mode pedestals are typically found to be near a critical value for  $\alpha_{\text{MHD}}$  dependant on the plasma shape [56] – stronger shaping is associated with slower ELM frequencies and greater stabilization of type-I ELMs, consistent with ballooning MHD [19, 50, 53]. Due to the restricted width range for the pedestal on a given machine [45, 54], the  $\alpha_{\text{MHD}}$  limit reduces, to good approximation, to a limit on  $\beta_p$  at the pedestal top [50, 53]. For example, points at matched shaping, field and current across a DIII-D/C-Mod similarity experiment, shown in fig. 2.3, lie on a fixed  $n_e T_e$  line. The transition from type-I to type-III ELMs with increasing density and decreasing temperature [50], or alternately the transition from type-III ELMs just above the L-H transition to type-I ELMs with increasing heating power [52], is consistent with the transition from a resistive mode for type-III ELMs to the ideal MHD modes identified with type-I ELMs.

A naive ballooning MHD analysis, however, does not accurately capture the ELMy H-mode pedestal – parallel observations of MHD stability in early ELMy H-modes also identified current-driven kink/peeling modes as a potential limiting instability, particularly at low collisionality [43, 44, 52]. This is particularly true in light of the *bootstrap current*, an effect by which gradients in the plasma self-generate an electric current, given by [48]

$$j_{\text{boot}} = I(\psi)p_e(\psi) \left[ \alpha \frac{dn_e}{d\psi} + \beta \frac{dT_e}{d\psi} + \gamma \frac{dT_i}{d\psi} \right] \quad (2.10)$$

where  $I(\psi) = RB_\phi$  is a flux function encoding the field,  $p_e(\psi)$  is the electron pressure, and  $\alpha$ ,  $\beta$ , and  $\gamma$  are coefficients determined by the collisionality and trapped-particle fraction, ordered  $\alpha > \beta > \gamma$ . Due to the strong density and temperature gradients in the pedestal, the local current density may be large enough for current-driven kink/peeling modes to be a concern.

MHD models built on coupled peeling and ballooning MHD modes, as well as diamagnetic effects stabilizing ballooning modes with high toroidal mode number  $n$  [44], have been developed [65, 66] and successfully capture the MHD limits of the ELMy H-mode. Moreover, turbulence studies based on the kinetic ballooning mode [67] predict that the mode will limit the pressure gradient and width such that the pedestal width scales with  $\beta_{p,\text{ped}}$  in a manner consistent with experimental observations,  $\Delta_{\text{ped}} \sim \beta_{p,\text{ped}}^{1/2}$  [68]. Turbulent fluctuations with an onset soon after the inter-ELM pressure pedestal gradient saturation have been observed [69], but a definitive analysis is still ongoing. A self-consistent model including both the MHD and turbulent constraints, EPED [70], has been implemented and tested in multi-machine analyses [71], including on DIII-D [72], C-Mod [73], and KSTAR [74]. The constraints of this model are discussed in detail in chapter 3.

### 2.2.3 Active ELM Control

In lights of the potential deleterious effects of large ELMs on ITER-scale devices [61, 62], mitigating or preventing large type-I ELMs in H-mode is of prime concern. One engineering solution for active ELM control is the application of a *resonant magnetic perturbation* (RMP) [75, 76, 77]. This perturbation drives additional particle and energy losses along stochastic field lines crossing the edge, limiting the pedestal before a large ELM boundary is reached [75, 76]. Small perturbations (less than 1/1000 the magnitude of the background magnetic field), for example that driven by an  $n = 3$  coil set on DIII-D [75] or a variable  $n = 3, 4, 6$  set on MAST [78], couples to the intrinsic error field caused by the toroidal-field coils to provide the reso-

nant perturbation [76]. Due to its resonant nature, the RMP effect is strongly sensitive on edge safety factor  $q$ , limiting the potential profiles possible for RMP ELM suppression [76]. This results in a strong density pumpout, along with moderate decreases in pedestal temperature gradients, which relaxes the pedestal and maintains it in the peeling-balloonning stable region [72, 77].

Rather than attempting to eliminate the ELM instability, it is also possible to “smooth out” the ELM heat pulse using pellet pacing [79]. Generally, the transient ELM power  $P_{\text{ELM}} \sim f_{\text{ELM}} \Delta W_{\text{ELM}}$  is roughly fixed - thus smaller, faster ELMs expel the less energy per ELM for the same average power. By triggering smaller, faster ELMs the heat load can be smoothed to a level closer to steady-state heat loads tolerable to divertor materials, rather than large transient heat pulses. In pellet pacing, the sharp density increase locally introduced in the pedestal by the pellet triggers a high- $n$  ballooning mode, resulting in a small ELM. In ITER-match experiments on DIII-D [79], cryogenic Deuterium pellets fired at twelve times the expected ELM frequency (roughly 5 Hz) reduced the per-ELM energy loss from 8% of total stored energy, 55 kJ, to less than 0.5% (3 kJ). However, the question of feasibility of pellet pacing for ITER, as well as the potential for non-axisymmetric heat loading in the divertor due to the localized nature of the pellet perturbation, remain open for the applicability of the concept to ITER.

#### 2.2.4 Prospects for ELMy H-Mode

Though ELMy H-mode represents the most readily attainable high-performance regime, its applicability to ITER-scale devices hinges on the limitation, mitigation, or elimination of large ELMs and the associated heat loads on wall and divertor surfaces. ELM losses from type-I ELMs tend to be smaller for a given  $\beta_{p,\text{ped}}$  at higher density and lowe temperature, ultimately transitioning to type-III ELMs [53], however these plasmas tend to exhibit lower global confinement [50]. Type-II ELMs may provide the necessary near-continuous heat exhaust, but access to the regime is narrow and highly sensitive to shaping [59]. Alternately, ELM heat loading in type-I regimes may be controlled or suppressed via engineering solutions (i. e., RMP or pellet pacing) – but these are similarly limited in availability, and are of uncertain extrapolation to ITER-scale devices. Thus, recent efforts have also placed great emphasis on high-performance regimes that are naturally free of large ELMs. •

### 2.3 ELM-SUPPRESSED H-MODES

In addition to H-modes exhibiting ELMs, classes of H-mode have been established capable of stationary operation with acceptable lev-

els of particle transport (avoiding the radiative collapse and subsequent transient nature found in classical ELM-free H-modes) without exhibiting the bursty heat and particle transport driven by ELMs. Rather, the pedestal is regulated by a continuous fluctuation localized in the pedestal. Due to this attractive property, these regimes have been extensively researched. The characteristics of two major types, the Quiescent H-mode (QH-mode) and Enhanced D <sub>$\alpha$</sub>  (EDA) H-mode are presented here.

### 2.3.1 QH-Mode

The *Quiescent H-mode* (QH-mode) was first observed on DIII-D [80, 81], and subsequently achieved on ASDEX Upgrade [82], JT-60U [83], and JET [84]. In QH-mode operation, following a brief ELM-free or ELMing phase after the L-H transition, the plasma enters a state with steady averaged density and radiated power, indicating a lack of serious impurity accumulation, despite lacking ELM transport (evident from divertor D <sub>$\alpha$</sub>  light, which is “quiescent” compared to the characteristic spikes driven by ELMs). Although QH-mode requires lower densities (average density reduced by roughly a factor of two from comparable ELMMy H-modes) with cryopumping for density control, access is otherwise robust, with successful operation across a broad range of shaping, safety factor, current and field [80]. The regime is capable of stationary operation, with the mode sustained for most of the current flat-top on DIII-D ( $\sim 25\tau_E$ ) with very good confinement – in cases with an internal transport barrier in addition to the pedestal (termed the “Quiescent Double Barrier” or QDB regime [85, 86, 87]) a confinement metric of  $\beta_N H_{89} \sim 7$  was reached (albeit for a briefer period,  $\sim 5\tau_E$ ), compared to  $\beta_N H_{89} \sim 4$  found in ELMMy H-modes on DIII-D [86]. Here we use the normalized pressure metric [88]

$$\beta_N = \beta \frac{a B_T}{I_p} \quad (2.11)$$

in mT/MA. Similarly competitive confinement between QH-mode and ELMMy H-mode is seen on ASDEX Upgrade and JET, although the mode on JT-60U is out-performed by ELMMy H-mode [89]. The pedestal density is reduced (comparable to the reduction in globally-averaged density) in QH-mode compared to ELMMy H-mode, and excess fueling to the edge by gas puffing, pellet fueling, or wall outgassing destroys the QH-mode. However, pedestal temperatures are typically somewhat higher [86], thus the mode is found at ITER-relevant low collisionalities. Pedestal pressure gradients are comparable to those found in ELMMy H-mode, implying stabilization of the peeling-balloonning MHD modes typically associated with the ELM trigger [80]. A particularly strong E<sub>r</sub> well (2 – 3 times deeper than

*elaborate?*

in comparable ELMy H-modes) is also observed in the QH-mode pedestal [87].

In place of bursty ELM transport, the pedestal in QH-mode is continuously regulated by the *Edge Harmonic Oscillation* (EHO), an MHD mode observed in density, temperature, and magnetic fluctuations [80]. The EHO is made up of distinct harmonics with toroidal mode numbers  $n \sim 1 - 10$ ; these harmonics are directly observed in the particle flux at the divertor, indicating that the EHO is responsible for density regulation in QH-mode [86]. MHD modeling approaches similar to that described in chapter 3 indicate that the EHO is a saturated peeling mode [72, 90, 91]. This is consistent with the low pedestal collisionality in the QH-mode pedestal (lower collisionalities and higher bootstrap currents tends to drive the pedestal towards the peeling side of the peeling-balloonning MHD boundary, as described in chapter 3), and with the observed localization of the EHO in the region of strongest  $E_r$  and rotation shear [85]. The saturated mode is driven by the strong rotation shear in the edge – while this typically destabilizes low- $n$  MHD modes, in the case of the EHO the magnetic component of the mode couples to the vacuum-vessel wall as the rotation spins up, providing the drag force necessary to saturate the mode at finite amplitude [92]. This maintains the pedestal below the current-driven peeling boundary associated with the ELM trigger, providing the ELM suppression in QH-mode [72].

*pull ref 9 from  
Burrell2009?*

Historically, QH-mode operation has required significant neutral-beam inputs directed counter the plasma current direction, providing the necessary rotation [80]. However, counter-current beam operation drives significant fast-ion losses into the outer wall, necessitating operation with a large outer gap to avoid wall outgassing. More recent experiments have successfully generated QH-modes with co-current beam injection [92] and with torque from non-axisymmetric magnetic fields [93, 94]. The latter is of particular importance, as it is not expected that the NBI systems on ITER will drive sufficient torque to produce QH-mode [93]. In addition to the requirement for externally-supplied torque to maintain the mode, QH-mode suffers from accumulation of high-Z impurities – while lower-Z ions are flushed from the plasma by the EHO, high-Z impurities tend to accumulate in the core [84, 86], which may present difficulties attaining QH-mode on metal-walled machines where high-Z impurities dominate. Nevertheless QH-mode is an attractive option for a reactor regime.

### 2.3.2 EDA H-Mode

The *Enhanced D<sub>α</sub> H-mode* (EDA H-mode) is a high-performance regime explored on the Alcator C-Mod tokamak [95, 96, 97]. Along with transient ELM-free H-modes, the EDA regime is the customary approach to H-mode operation on C-Mod, unlike other major tokamak exper-

*time trace,  
fluctuations, profile  
comparison between  
EDA, ELMy*

**Figure 2.4:** Characteristic traces of an EDA H-mode on C-Mod (section 2.3.2). Following a brief ELM-free phase, the plasma density and radiated power stabilizes at a sustainable level. The edge transport barrier is regulated by the continuous QCM fluctuation rather than bursty ELM transport.



*make sure to elaborate on this in ELM section or reference later*

*move this elsewhere?*

*check this, reward?*

iments; the Type-I ELM My H-mode typical on other devices requires an abnormal shaping to more easily reach the stability boundary associated with the ELM trigger on C-Mod [47]. In EDA operation, the L-H transition is followed by a rise in radiated power and density similar to an ELM-free H-mode. However, shortly thereafter the H-mode stabilizes at steady density [95], with the radiated power held at  $P_{rad}/P_{in} \sim 30\%$  [98], allowing steady operation (maintained for most of the steady current phase,  $\sim 10\tau_E$ ) and good performance, with  $H_{89} \sim 1.9$ ,  $H_{98} \sim 1$  [96]. Notably, modeling of the pedestal in EDA H-mode indicates energy confinement with potentially weaker degradation of  $\tau_E$  with input heating power [97, 99, 100]. Rather than bursty ELM transport, the EDA pedestal is regulated by a continuous density pumpout, with divertor  $D_\alpha$  signals (indicative of the density exhaust from the plasma) recovering to near L-mode levels after an initial drop at the L-H transition. Access to EDA H-mode is

fairly robust, although it is strongly favored by higher collisionality ( $\nu^* > 1$ ) and edge safety factor [99, 101] and by strong shaping [101]. Although a higher collisionality is observed to be required at lower values of  $q_{95}$ , a collisionality threshold alone is insufficient to explain EDA access [99]. Instead, EDA and ELM-free H-modes are separated in a phase space of collisionality and normalized pressure gradient ( $\nu^* - \alpha_{MHD}$ ) – however, the transition between the two regimes is soft, with the EDA smoothly appearing at higher pressure gradients and collisionalities rather than exhibiting a sharp transition [102].

While the pedestal pressure in EDA H-mode is comparable to that in ELM<sub>y</sub> H-mode, the pedestal profiles in EDA tend towards higher density and lower temperature – this strongly alters the collisionality (consistent with the observed requirements for  $\nu^* > 1$  for EDA access) and bootstrap current near the edge, with significant impact on MHD behavior. The pedestal appears to be limited by transport effects rather than stability – the pedestal is modeled to be stable to ideal MHD effects [47, 101], despite exhibiting a  $\nabla p \sim I_p^2$  trend expected from a ballooning instability [100]. Instead, the pedestal density is determined by the interplay between an inward particle pinch and outward density transport. Outward particle transport is decreases at higher currents (and therefore higher densities at fixed Greenwald fraction), while the high pedestal density results in strong ionization in the scrape-off layer and an edge that is relatively opaque to neutrals [21, 103]. As a result, the density will rise until the transport saturates – additional fueling through the edge triggers minimal response, while a density drop is countered by increased particle confinement to recover the density, resulting in pedestal and global density values set by the plasma current, with weak dependence on other engineering parameters [104].

The regulation of the pedestal in EDA H-mode is provided by the *Quasi-Coherent Mode* (QCM), a field-aligned electromagnetic fluctuation localized in the steep-gradient region of the pedestal [96, 105, 106]. The QCM is a fairly narrow-band ( $\delta f/f \sim 10\%$ ) mode strongly visible in density and magnetic fluctuations, with a centroid frequency of 50 – 200 kHz and a fairly short poloidal wavelength,  $k_\theta \sim 1.5 \text{ cm}^{-1}$  [105]. QCM fluctuations are visible in the density flux to the divertor, indicating that the QCM fluctuation is directly responsible for the particle transport through the EDA H-mode pedestal [21, 105]. Numerical modeling of the EDA H-mode pedestal suggests a resistive ballooning mode (the collisional analogue to the ideal ballooning MHD mode found in ELM<sub>y</sub> H-modes) for the QCM [102, 107]. This is consistent with experimental observations of the EDA pedestal – the requirement of high collisionality (the QCM disappears below  $\nu^* \sim 0.1$ ) suggests a resistive effect [47], while the favored high edge pressure gradient ( $\alpha_{MHD}$ ) suggests a ballooning instability. At high power and high edge pressure gradient, the QCM is replaced by

*define  $\nu^*$  here, or earlier?*

*define  $\alpha_{MHD}$  before here*

*elaborate here, or elsewhere?*

*explain or reward*

*describe this in ELM<sub>y</sub> section*

small, high-frequency ELMs [101, 102, 106], potentially indicating that the pedestal is “burning through” the resistive-balloonning regulation of the pedestal and reaching the ideal MHD boundary associated with the ELM trigger.

*ref here about high collisionality in other small-ELM regimes?*

The EDA H-mode presents another potential route to reactor-scale operation with naturally-suppressed large ELMs. The regime is robustly accessible on C-Mod using only RF heating with no external momentum sources or non-axisymmetric magnetic coils, with good confinement and acceptable levels of impurity accumulation and radiated power consistent with high performance [108]. Moreover, there is an extensive body of research studying the EDA H-mode on a machine with all-metal walls, with ITER-relevant heat flux and edge neutral behavior [21, 103], and with similar electron-ion equilibration to that expected for ITER [11]. However, the necessary collisionality ( $\nu^* > 1$ ) for the QCM fluctuation is significantly higher than the expected levels for the ITER pedestal ( $\nu^* < 0.1$ ), inconsistent with unaided access to the EDA regime. •

*where to go with this, mention shoelace?*

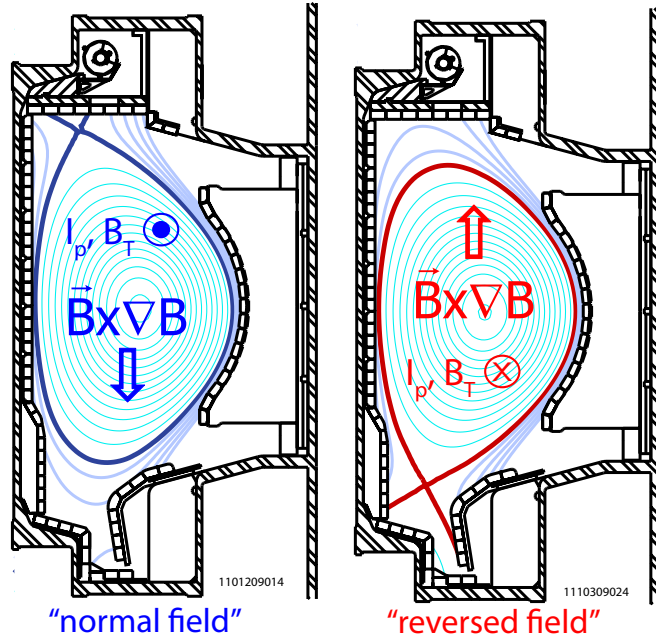
#### 2.4 I-MODE

*reword this, shorter*

In order for an H-mode regime to achieve stationary operation, there must be some form of relaxation of the density transport barrier – either by intermittent bursts of transport due to ELMs, or through a continuous fluctuation regulating the particle confinement (as in the EDA and QH-modes). However, each of these modes faces some level of increased particle confinement, as well as difficulties inherent in their operation – the large type-I ELMs found in the most readily accessible ELMy H-mode on most tokamaks is incompatible with reactor-scale operation due to the large pulsed heat loads on wall and divertor materials [61, 62], while alternate H-modes are more restricted in their accessibility. Recent work on Alcator C-Mod has demonstrated a novel high-confinement regime, termed the *I-mode*, which is unique in that it appears to completely decouple energy and particle transport, forming an H-mode-like temperature pedestal with the accompanying improvement in energy confinement, while maintaining an L-mode density profile and particle transport level. I-mode exhibits several highly attractive properties for a reactor regime:

1. The lack of a particle transport barrier or density pedestal maintains the desired level of impurity flushing from the plasma, avoiding excessive radiative losses
2. I-mode appears to be generally stable against large ELMs, avoiding the excessive pulsed heat loads found in ELMs (of critical importance for ITER-scale devices) without externally-applied engineering controls

**Figure 2.5:** C-Mod cross-sections illustrating magnetic configurations suitable for I-mode access. Either upper-null operation in the normal field direction, or lower-null with field and current reversed provides ion  $\nabla B$  drift away from the X-point. This configuration is unfavorable for the H-mode threshold, but allows for easier access to I-mode.



3. appears to exhibit much weaker degradation of confinement with increased heating power

A firm understanding of the structure and stability of the I-mode pedestal is essential for the extrapolation of I-mode operation to larger devices, and will form the balance of this thesis.

#### 2.4.1 Access and Operation

It has been long established that the orientation of the X-point (described in section 1.2.2) relative to the vertical particle drifts (particularly the  $\nabla B$  drift, eq. (1.20)) in the plasma column has a strong effect on plasma behavior, particularly flows in the edge [103, 109, 110, 111]. Notably, in cases where the ion  $\nabla B$  drift is directed towards the X-point, the power threshold to access conventional H-modes is reduced by roughly a factor of two [59, 112, 113] (thus for the balance of this section we refer to this configuration as the “favorable  $\nabla B$  drift direction”). In experiments in the unfavorable drift configuration (that is, ion  $\nabla B$  drift away from the X-point), however, a transitional state was observed in L-H threshold experiments in which energy confinement improved before the formation of a classical H-mode. This transient state, termed the “improved L-mode” on ASDEX [114], was later expanded into a sustained, distinct operating regime, termed I-mode, on Alcator C-Mod [11, 115, 116].

I-mode access is fairly robust, provided the appropriate drift configuration is held – this can be achieved either by running an upper-null shape, or by reversing the field (as well as the plasma current, to maintain magnetic-field helicity) and running in a standard LSN

*graphic here*

*ref to description,  
prob chapter 4?*

shape [117]. Upper-null operation allows a broader range of plasma shapes, but suffers from poorer diagnostic coverage and power handling due to the SOL flux impinging on a flat strike plate rather than the full lower divertor [117, 118]. Short I-mode periods have also been observed in the favorable-drift configuration in a modified plasma shape used for ELMy H-mode experiments on C-Mod, but these transitioned quickly into H-mode and will not be considered for the balance of this thesis [47, 118]. In either the forward-field USN or reversed-field LSN shape, I-mode access is favored by higher heating powers, low collisionality, and strong shaping [115]; as with all C-Mod operation, I-mode is accessible with purely RF heating, without external sources of momentum input [119]. Unlike H-modes on C-Mod, I-mode operation is also largely insensitive to wall conditions due to the low impurity confinement [117].

Initially, access to I-mode was available within a relatively narrow window in density and heating power – I-mode attempts with insufficient density were aborted by core radiation from high-Z impurities generated by interactions between fast ions and the wall, while high-density or high-power cases tended to transition into an ELM-free H-mode [115]. However, more recent experiments have greatly expanded both the available density and heating power range in I-mode, particularly by fueling into established I-modes to maintain sufficiently low density at the L-I transition [119]. As of the most recent campaign, I-modes can be sustained for the current flat-top ( $\sim 20\tau_E$ ) up to the maximum available RF heating power [117, 119].

#### 2.4.2 Global Performance & Edge Behavior

I-mode is characterized by H-mode-like energy confinement ( $H_{98} \sim 1$ ) while maintaining an L-mode density profile and particle transport level. While the pedestal density is generally low,  $n_{e,ped} \sim 1 \times 10^{20} \text{ m}^{-3}$ , pedestal temperatures are typically higher than H-modes at comparable power. Due to profile stiffness in the core, this results in very high core temperatures, and global-average pressures near the C-Mod H-mode – and therefore the all-tokamak – record ( $\sim 1.5 \text{ atm}$  in I-mode, compared to  $\sim 1.8 \text{ atm}$  in H-mode) [116]. Notably, scalings of stored energy against RF power in I-mode indicate only weak degradation of energy confinement with heating power, contrary to the  $\tau_E \sim P^{-0.5}$  (L-mode) or  $\tau_E \sim P^{-0.69}$  (ELMy H-mode) scalings previously observed – a potentially highly-favorable result for extrapolation to ITER-scale devices. Particle and impurity confinement, on the other hand, is minimal, limiting radiative losses to  $\sim 25\%$  of heating power, well below H-mode levels [115] – impurity confinement times and accumulation are measured to be at L-mode levels on laser blow-off [120] and charge-exchange [11, 121] diagnostics. Initial studies of the I-mode threshold indicate that the mode should be accessible on ITER at re-

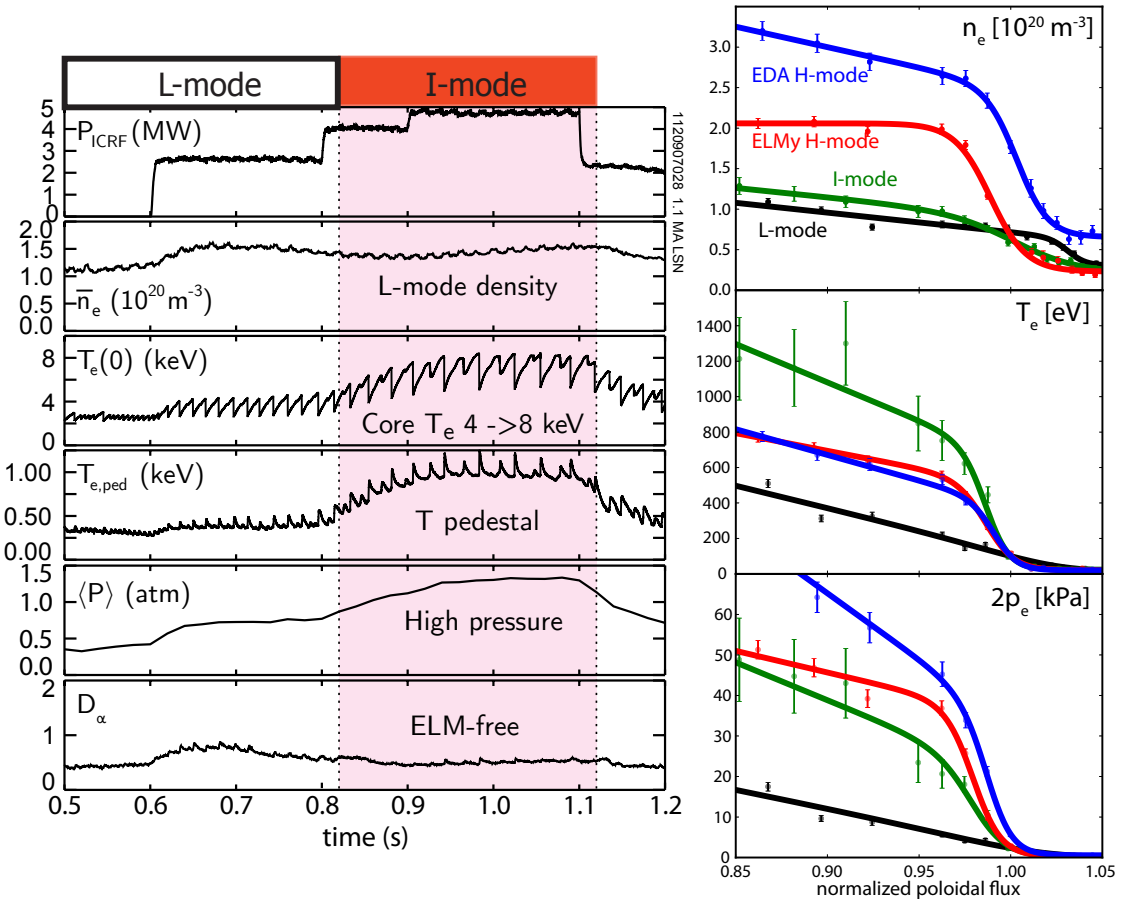


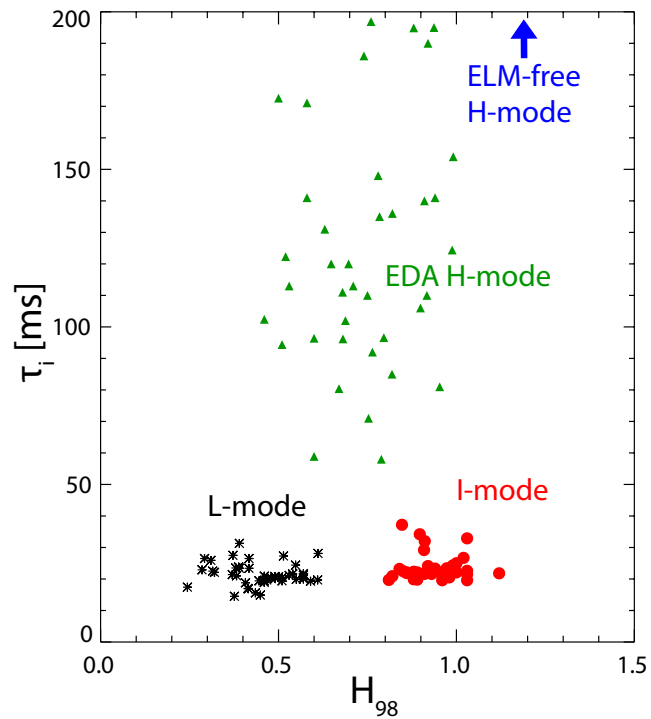
**Figure 2.6:** (right) Characteristic traces for a typical I-mode. At the L-I transition, the core and edge temperature rise over several sawtooth cycles before reaching a steady level; global confinement and pressure rise accordingly. However, the density remains at L-mode levels, and no ELMs are exhibited. (left) Edge profiles for density, temperature, and pressure in L-, I-, and H-mode. The I-mode (green) retains an density profile comparable to the L-mode (black), unlike the ELMy (red) and EDA (blue) H-modes which form a strong density pedestal. However, the I-mode forms a taller temperature pedestal than either H-mode. As a result, the I-mode reaches comparable pedestal pressures to the H-modes while retaining L-mode particle transport.

duced density ( $\sim 4 \times 10^{19} \text{ m}^{-3}$ ), then fueled after the transition up to a  $Q = 10$  scenario [22, 119]. Ready fueling control in such a scenario would be critical, as density is the primary engineering “knob” for fusion power in predominantly self-heated fusion plasmas [117].

The lack of a particle transport barrier in I-mode drives significantly different edge behavior compared to H-mode – the reduced  $\nabla n_e$  in the pedestal reduces both the overall pressure gradient and the bootstrap current drive, which has a stabilizing effect on both ballooning and kink/peeling edge MHD modes [47]. The SOL heat flux channel in I-mode also appears to be significantly wider than in comparable H-modes [115, 119]. Energy transport suppression in I-mode appears along with the expected  $E_r$  well at the edge – although historically I-mode  $E_r$  wells are shallower and exhibit weaker shear than those in H-mode, more recent measurements have found comparable well

define bootstrap earlier?

**Figure 2.7:** Impurity confinement time  $\tau_I$  measured by laser blow-off [120] versus normalized confinement  $H_{98}$  for L-mode, I-mode, and H-mode. I-mode exhibits H-mode-like energy confinement, increased by roughly a factor of two over L-mode. However, I-mode retains L-mode levels of particle and impurity transport, readily flushing heavy impurities from the plasma. EDA H-mode exhibits strongly increased particle confinement, while transient ELM-free H-modes increase their particle confinement to the point of radiative collapse (see section 2.1).



depths in both regimes [121, 122]. I-modes exhibit toroidal rotation levels comparable to H-mode, consistent with a  $\nabla T_e$  scaling for rotation velocity [123], which may contribute to edge shearing in I-mode [121].

Notably, the edge behavior across the L-I transition is distinct from more conventional L-H transitions. While the L-H transition is a rapid ( $\sim 20$  ms on C-Mod) bifurcation in transport, the L-I transition is marked by a slower, steady increase in edge temperature, lasting up to  $\sim 150$  ms [115, 121]. The L-I transition appears to be tied to sawtooth heat pulses reaching the edge – with each heat pulse, the edge temperature “ratchets” upward, reaching a steady I-mode over several sawtooth cycles [116, 117]. The L-I transition is seen to be more rapid at higher levels of RF heating power and lower  $q_{95}$  [115]. Both factors are associated with larger sawtooth crashes, consistent with a transient heat pulse driving the transition [117].

*reword, check values*

*explain sawteeth  
where?*

#### 2.4.3 Edge Fluctuations – the Weakly-Coherent Mode

As with other high-performance regimes, the I-mode pedestal exhibits broadband suppression of turbulence at moderate frequencies (20 – 150 kHz). In its place, the I-mode pedestal exhibits a broad electromagnetic fluctuation termed the *Weakly-Coherent Mode* [115]. The WCM is primarily observed as a density and magnetic fluctuation, although temperature fluctuations associated with the mode are also observed (albeit at an amplitude reduced by roughly an order of mag-

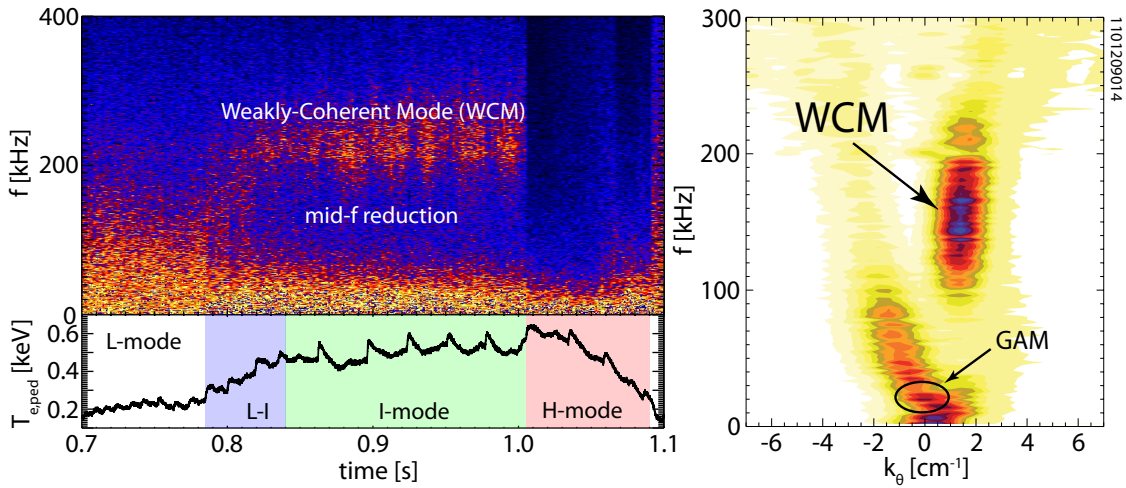


**Figure 2.8:** Measurements of  $n_e$  fluctuations from the WCM in I-mode. (left) Reflectometer measurements in the pedestal region, showing the transition from broadband L-mode turbulence to the WCM, and subsequent fluctuation suppression as the plasma transitions into an ELM-free H-mode. Edge  $T_e$  measurements are also shown, tracking the formation of the characteristic I-mode temperature pedestal. Note the dynamics of the L-I transition – while the edge temperature increases steadily over several sawtooth periods, the turbulence suppression and formation of the WCM is more rapid, with the mode spinning up in frequency as the I-mode is established. (right) Gas-puff imaging measurements of the WCM, averaged over the I-mode. The mode is restricted in  $k$ -space to  $k_\theta \sim 2 \text{ cm}^{-1}$ , but is broad in frequency. Also shown is the  $k_\theta = 0$ ,  $f \sim 10 \text{ kHz}$  signal of the GAM coupled to the WCM. [point to Cziegler here?](#)

nitude) [118, 124, 125]. Due to its prominence in the I-mode edge and similarity to the quasi-coherent mode (QCM) found in the EDA H-mode, the WCM is a prime candidate for pedestal regulation in I-mode, driving the enhanced density transport – initial observations indicate a correlation between particle flux through the LCFS and the (normalized) WCM amplitude [118], although a firm characterization of the effect of the WCM on the particle transport is ongoing.

The WCM is found at fairly short poloidal wavelength,  $k_\theta \sim 1.5 \text{ cm}^{-1}$ , similar to the QCM [118]. Compared to the QCM, however, the WCM is significantly less coherent –  $\delta f/f \sim 50\%$ , compared to  $\sim 10\%$  for the QCM – and exists at a higher frequency ( $200 - 400 \text{ kHz}$ ) and phase velocity [116, 124]. While the radial location and extent of the WCM has not yet been definitively determined, it has been localized within the last  $\sim 2 \text{ cm}$  of the LCFS by O-mode reflectometry [118] and gas-puff imaging [124, 126]. The onset of the WCM is immediate and contemporaneous with the turbulence suppression in the L-I transition, unlike the formation of the  $T_e$  pedestal, which typically requires several sawtooth cycles to form [126]. However, the WCM can “dither” for several sawtooth heat pulses in marginal I-modes, and typically spins up in frequency as the mode is established (contrary to the behavior observed in the QCM) [116, 126].

The nature of the WCM is, as of this writing, an open question – several candidate instabilities have been proposed, including a branch

*elaborate on  
potential modes?  
general cite for  
GAM?*

of the kinetic-balloonning mode [67] or the heavy-particle mode [127, 128], but the underlying instability in the WCM remains unknown. Notably, the WCM appears to be coupled to Geodesic Acoustic Modes (GAMs) in the plasma edge. GAM dynamics have been associated with the L-H transition on other tokamaks, but GAMs are not seen in H-modes on C-Mod – however, persistent GAMs co-existing with the mean flow in the edge are consistently seen in I-mode [124]. Interplay with GAMS appears to drive much of the physics of the WCM, but the nature of the relationship between the two is still the subject of active research.

★

## BIBLIOGRAPHY

---

- [1] A. Loarte, B. Lipschultz, A.S. Kukushkin, G.F. Matthews, P.C. Stangeby et al. **Chapter 4: Power and particle control.** *Nuclear Fusion*, 47(6):S203, 2007.
- [2] F. Wagner, G. Becker, K. Behringer, D. Campbell, A. Eberhagen et al. **Regime of improved confinement and high beta in neutral-beam-heated divertor discharges of the ASDEX tokamak.** *Physical Review Letters*, 49(19):1408–1412, Nov 1982.
- [3] M Keilhacker, G Becker, K Bernhardi, A Eberhagen, M ElShaer et al. **Confinement studies in L and H-type ASDEX discharges.** *Plasma Physics and Controlled Fusion*, 26(1A):49, 1984.
- [4] P.N. Yushmanov, T. Takizuka, K.S. Riedel, O.J.W.F. Kardaun, J.G. Cordey et al. **Scalings for tokamak energy confinement.** *Nuclear Fusion*, 30(10):1999, 1990.
- [5] M. Greenwald, R.L. Boivin, F. Bombarda, P.T. Bonoli, C.L. Fiore et al. **H-mode confinement in Alcator C-Mod.** *Nuclear Fusion*, 37(6):793, 1997.
- [6] Grigory Kagan and Peter J Catto. **Neoclassical ion heat flux and poloidal flow in a tokamak pedestal.** *Plasma Physics and Controlled Fusion*, 52(5):055004, 2010.
- [7] Matt Landreman and Darin R Ernst. **Local and global Fokker–Planck neoclassical calculations showing flow and bootstrap current modification in a pedestal.** *Plasma Physics and Controlled Fusion*, 54(11):115006, 2012.
- [8] R. J. Groebner, K. H. Burrell and R. P. Seraydarian. **Role of edge electric field and poloidal rotation in the L-H transition.** *Physical Review Letters*, 64(25):3015–3018, Jun 1990.
- [9] Keith H. Burrell. **Tests of causality: Experimental evidence that sheared  $E \times B$  flow alters turbulence and transport in tokamaks.** *Physics of Plasmas*, 6(12):4418–4435, 1999.
- [10] P. W. Terry. **Suppression of turbulence and transport by sheared flow.** *Reviews of Modern Physics*, 72:109–165, Jan 2000.
- [11] R. M. McDermott, B. Lipschultz, J. W. Hughes, P. J. Catto, A. E. Hubbard et al. **Edge radial electric field structure and its connections to H-mode confinement in Alcator C-Mod plasmas.** *Physics of Plasmas*, 16(5):056103, 2009.

- [12] K. C. Shaing and E. C. Crume. **Bifurcation theory of poloidal rotation in tokamaks: A model for L-H transition.** *Physical Review Letters*, 63(21):2369–2372, Nov 1989.
- [13] H. Biglari, P. H. Diamond and P. W. Terry. **Influence of sheared poloidal rotation on edge turbulence.** *Physics of Fluids B: Plasma Physics*, 2(1):1–4, 1990.
- [14] Y. B. Kim, P. H. Diamond and R. J. Groebner. **Neoclassical poloidal and toroidal rotation in tokamaks.** *Physics of Fluids B: Plasma Physics*, 3(8):2050–2060, 1991.
- [15] A S Ware, P W Terry, P H Diamond and B A Carreras. **Transport reduction via shear flow modification of the cross phase.** *Plasma Physics and Controlled Fusion*, 38(8):1343, 1996.
- [16] K H Burrell, T N Carlstrom, E J Doyle, D Finkenthal, P Gohil et al. **Physics of the L-mode to H-mode transition in tokamaks.** *Plasma Physics and Controlled Fusion*, 34(13):1859, 1992.
- [17] L. Schmitz, L. Zeng, T. L. Rhodes, J. C. Hillesheim, E. J. Doyle et al. **Role of zonal flow predator-prey oscillations in triggering the transition to H-mode confinement.** *Physical Review Letters*, 108:155002, Apr 2012.
- [18] J.E. Kinsey, G.M. Staebler, J. Candy, R.E. Waltz and R.V. Budny. **ITER predictions using the GYRO verified and experimentally validated trapped gyro-Landau fluid transport model.** *Nuclear Fusion*, 51(8):083001, 2011.
- [19] H Zohm. **Edge localized modes (ELMs).** *Plasma Physics and Controlled Fusion*, 38(2):105, 1996.
- [20] I. H. Hutchinson, R. Boivin, F. Bombarda, P. Bonoli, S. Fairfax et al. **First results from Alcator C-Mod.** *Physics of Plasmas*, 1(5):1511–1518, 1994.
- [21] M. Greenwald, N. Basse, P. Bonoli, R. Bravenec, E. Edlund et al. **Confinement and transport research in Alcator C-Mod.** *Fusion Science and Technology*, 51(3):266–287, 2007.
- [22] M. Greenwald, A. Bader, S. Baek, H. Barnard, W. Beck et al. **Overview of experimental results and code validation activities at Alcator C-Mod.** *Nuclear Fusion*, 53(10):104004, 2013.
- [23] J.L. Luxon. **A design retrospective of the DIII-D tokamak.** *Nuclear Fusion*, 42(5):614, 2002.
- [24] J.L. Luxon, T.C. Simonen, R.D. Stambaugh and the DIII-D Team. **Overview of the DIII-D fusion science program.** *Fusion Science and Technology*, 48(2):807–827, October 2005.

- [25] J.L. Luxon. **A brief introduction to the DIII-D tokamak.** *Fusion Science and Technology*, 48(2):828–833, October 2005.
- [26] A. Herrmann and O. Gruber. **Chapter 1: ASDEX upgrade - introduction and overview.** *Fusion Science and Technology*, 44(3):569–577, November 2003.
- [27] F. Ryter, A. Stäbler and G. Tardini. **Chapter 5: Core energy transport in conventional scenarios in ASDEX Upgrade.** *Fusion Science and Technology*, 44(3):618–635, November 2003.
- [28] U. Stroth, J. Adamek, L. Aho-Mantila, S. Äkäslompolo, C. Amador et al. **Overview of ASDEX upgrade results.** *Nuclear Fusion*, 53(10):104003, 2013.
- [29] D.C. McDonald, Y. Andrew, G.T.A. Huysmans, A. Loarte, J. Onenga et al. **Chapter 3: ELMY H-mode operation on JET.** *Fusion Science and Technology*, 53(4):891–957, May 2008.
- [30] F. Romanelli and JET EFDA Contributors. **Overview of the JET results with the ITER-like wall.** *Nuclear Fusion*, 53(10):104002, 2013.
- [31] Y. Kamada, T. Fujita, S. Ishida, M. Kikuchi, S. Ide et al. **Fusion plasma performance and confinement studies on JT-60 and JT-60U.** *Fusion Science and Technology*, 42(2,3):185–254, November 2002.
- [32] A. Kitsunezaki, M. Shimizu, H. Ninomiya, M. Kuriyama and the JT-60 Team. **JT-60 program.** *Fusion Science and Technology*, 42(2,3):179–184, September 2002.
- [33] Y. Kusama, M. Yamamoto and the JFT-2M Group. **JFT-2M program.** *Fusion Science and Technology*, 49(2):89–95, February 2006.
- [34] Y. Miura, M. Mori, T. Shoji, H. Matsumoto, K. Kamiya et al. **Studies of improved confinement in JFT-2M.** *Fusion Science and Technology*, 49(2):96–121, February 2006.
- [35] M. Shimada, D.J. Campbell, V. Mukhovatov, M. Fujiwara, N. Kirneva et al. **Chapter 1: Overview and summary.** *Nuclear Fusion*, 47(6):S1, 2007.
- [36] ITER Physics Expert Group on Confinement, Transport and ITER Physics Expert Group on Confinement Modelling and Database and ITER Physics Basis Editors. **Chapter 2: Plasma confinement and transport.** *Nuclear Fusion*, 39(12):2175, 1999.
- [37] E.J. Doyle, W.A. Houlberg, Y. Kamada, V. Mukhovatov, T.H. Osborne et al. **Chapter 2: Plasma confinement and transport.** *Nuclear Fusion*, 47(6):S18, 2007.

- [38] Y R Martin, T Takizuka and the ITPA CDBM H-mode Threshold Database Working Group. **Power requirement for accessing the H-mode in ITER.** *Journal of Physics: Conference Series*, 123(1):012033, 2008.
- [39] W Suttrop, O Gruber, B Kurzan, H D Murmann, J Neuhauser et al. **Effect of plasma shape variation on ELMs and H-mode pedestal properties in ASDEX upgrade.** *Plasma Physics and Controlled Fusion*, 42(5A):A97, 2000.
- [40] A E Hubbard. **Physics and scaling of the H-mode pedestal.** *Plasma Physics and Controlled Fusion*, 42(5A):A15, 2000.
- [41] T Hatae, Y Kamada, S Ishida, T Fukuda, T Takizuka et al. **Characteristics of edge pedestal width in JT-60U ELM-free H-mode plasmas.** *Plasma Physics and Controlled Fusion*, 40(6):1073, 1998.
- [42] P Breger, C Flewin, K-D Zastrow, S J Davies, N C Hawkes et al. **Plasma-edge gradients in L-mode and ELM-free H-mode JET plasmas.** *Plasma Physics and Controlled Fusion*, 40(3):347, 1998.
- [43] R. J. Groebner and T. H. Osborne. **Scaling studies of the high mode pedestal.** *Physics of Plasmas*, 5(5):1800–1806, 1998.
- [44] W Suttrop. **The physics of large and small edge localized modes.** *Plasma Physics and Controlled Fusion*, 42(5A):A1, 2000.
- [45] P.A. Schneider, E. Wolfrum, R.J. Groebner, T.H. Osborne, M.N.A. Beurskens et al. **Analysis of temperature and density pedestal gradients in AUG, DIII-D and JET.** *Nuclear Fusion*, 53(7):073039, 2013.
- [46] J. Hughes, P. Snyder, X. Xu, J. Walk, E. Davis et al. **Pedestal stability and transport on the Alcator C-Mod tokamak: Experiments in support of developing predictive capability.** In *24th IAEA Fusion Energy Conference*, 2012.
- [47] J.W. Hughes, P.B. Snyder, J.R. Walk, E.M. Davis, A. Diallo et al. **Pedestal structure and stability in H-mode and I-mode: a comparative study on Alcator C-Mod.** *Nuclear Fusion*, 53(4):043016, 2013.
- [48] O. Sauter, C. Angioni and Y. R. Lin-Liu. **Neoclassical conductivity and bootstrap current formulas for general axisymmetric equilibria and arbitrary collisionality regime.** *Physics of Plasmas*, 6(7):2834–2839, 1999.
- [49] M. Greenwald, J.L. Terry, S.M. Wolfe, S. Ejima, M.G. Bell et al. **A new look at density limits in tokamaks.** *Nuclear Fusion*, 28(12):2199, 1988.

- [50] G. Saibene, L.D. Horton, R. Sartori, B. Balet, S. Clement et al. **The influence of isotope mass, edge magnetic shear and input power on high density ELMy H modes in JET.** *Nuclear Fusion*, 39(9):1133, 1999.
- [51] J.P. Christiansen, J.G. Cordey, K. Thomsen, A. Tanga, J.C. DeBoo et al. **Global energy confinement H-mode database for ITER.** *Nuclear Fusion*, 32(2):291, 1992.
- [52] J W Connor. **Edge-localized modes - physics and theory.** *Plasma Physics and Controlled Fusion*, 40(5):531, 1998.
- [53] H Urano, W Suttrop, L D Horton, A Herrmann, J C Fuchs et al. **Energy and particle losses during type-I ELMy H-mode in ASDEX Upgrade.** *Plasma Physics and Controlled Fusion*, 45(9):1571, 2003.
- [54] C.F. Maggi. **Progress in understanding the physics of the H-mode pedestal and ELM dynamics.** *Nuclear Fusion*, 50(6):066001, 2010.
- [55] M. N. A. Beurskens, T. H. Osborne, P. A. Schneider, E. Wolfrum, L. Frassinetti et al. **H-mode pedestal scaling in DIII-D, ASDEX Upgrade, and JET.** *Physics of Plasmas*, 18(5):056120, 2011.
- [56] T H Osborne, R J Groebner, L L Lao, A W Leonard, R Maingi et al. **H-mode pedestal characteristics, ELMs, and energy confinement in ITER shape discharges on DIII-D.** *Plasma Physics and Controlled Fusion*, 40(5):845, 1998.
- [57] H. Urano, T. Takizuka, Y. Kamada, N. Oyama, H. Takenaga et al. **Dimensionless parameter dependence of H-mode pedestal width using hydrogen and deuterium plasmas in JT-60U.** *Nuclear Fusion*, 48(4):045008, 2008.
- [58] B.W. Rice, K.H. Burrell, J.R. Ferron, C.M. Greenfield, G.L. Jackson et al. **Progress towards sustainment of advanced tokamak modes in DIII-D.** *Nuclear Fusion*, 39(11Y):1855, 1999.
- [59] W. Suttrop, A. Herrmann, F. Ryter and J. Stober. **Chapter 6: H-mode and pedestal physics in ASDEX Upgrade.** *Fusion Science and Technology*, 44(3):636–649, November 2003.
- [60] A.W. Leonard, A. Herrmann, K. Itami, J. Lingertat, A. Loarte et al. **The impact of ELMs on the ITER divertor.** *Journal of Nuclear Materials*, 266–269(0):109 – 117, 1999.
- [61] G Federici, A Loarte and G Strohmayer. **Assessment of erosion of the ITER divertor targets during type I ELMs.** *Plasma Physics and Controlled Fusion*, 45(9):1523, 2003.

- [62] A Loarte, G Saibene, R Sartori, D Campbell, M Becoulet et al. **Characteristics of type I ELM energy and particle losses in existing devices and their extrapolation to ITER.** *Plasma Physics and Controlled Fusion*, 45(9):1549, 2003.
- [63] R. L. Miller, M. S. Chu, J. M. Greene, Y. R. Lin-Liu and R. E. Waltz. **Noncircular, finite aspect ratio, local equilibrium model.** *Physics of Plasmas*, 5(4):973–978, 1998.
- [64] J. W. Connor, R. J. Hastie and J. B. Taylor. **Shear, periodicity, and plasma ballooning modes.** *Physical Review Letters*, 40:396–399, Feb 1978.
- [65] P. B. Snyder, H. R. Wilson, J. R. Ferron, L. L. Lao, A. W. Leonard et al. **Edge localized modes and the pedestal: A model based on coupled peeling–ballooning modes.** *Physics of Plasmas*, 9(5):2037–2043, 2002.
- [66] A D Turnbull, L L Lao, T H Osborne, O Sauter, E J Strait et al. **Edge localized modes in DIII-D high performance discharges.** *Plasma Physics and Controlled Fusion*, 45(10):1845, 2003.
- [67] W.M. Tang, J.W. Connor and R.J. Hastie. **Kinetic-balloonning-mode theory in general geometry.** *Nuclear Fusion*, 20(11):1439, 1980.
- [68] P. B. Snyder and G. W. Hammett. **Electromagnetic effects on plasma microturbulence and transport.** *Physics of Plasmas*, 8(3):744–749, 2001.
- [69] A. Diallo, W. Hughes, J. M. Greenwald, B. LaBombard, E. Davis et al. **Observation of edge instability limiting the pedestal growth in tokamak plasmas.** *Physical Review Letters*, 112:115001, Mar 2014.
- [70] P. B. Snyder, R. J. Groebner, A. W. Leonard, T. H. Osborne and H. R. Wilson. **Development and validation of a predictive model for the pedestal height.** *Physics of Plasmas*, 16(5):056118, 2009.
- [71] R.J. Groebner, C.S. Chang, J.W. Hughes, R. Maingi, P.B. Snyder et al. **Improved understanding of physics processes in pedestal structure, leading to improved predictive capability for ITER.** *Nuclear Fusion*, 53(9):093024, 2013.
- [72] P. B. Snyder, T. H. Osborne, K. H. Burrell, R. J. Groebner, A. W. Leonard et al. **The EPED pedestal model and edge localized mode-suppressed regimes: Studies of quiescent H-mode and development of a model for edge localized mode suppression via resonant magnetic perturbations.** *Physics of Plasmas*, 19(5):–, 2012.

- [73] J.R. Walk, P.B. Snyder, J.W. Hughes, J.L. Terry, A.E. Hubbard et al. **Characterization of the pedestal in Alcator C-Mod ELM-ing H-modes and comparison with the EPED model.** *Nuclear Fusion*, 52(6):063011, 2012.
- [74] Hyunsun Han, Ohjin Kwon and J. Y. Kim. **Predictive modeling of pedestal structure in KSTAR using EPED model.** *Physics of Plasmas*, 20(10):–, 2013.
- [75] T. E. Evans, R. A. Moyer, P. R. Thomas, J. G. Watkins, T. H. Osborne et al. **Suppression of large edge-localized modes in high-confinement DIII-D plasmas with a stochastic magnetic boundary.** *Physical Review Letters*, 92:235003, Jun 2004.
- [76] R. A. Moyer, T. E. Evans, T. H. Osborne, P. R. Thomas, M. Be- coulet et al. **Edge localized mode control with an edge resonant magnetic perturbation.** *Physics of Plasmas*, 12(5):–, 2005.
- [77] T E Evans, R A Moyer, K H Burrell, M E Fenstermacher, I Joseph et al. **Edge stability and transport control with resonant mag- netic perturbations in collisionless tokamak plasmas.** *Nature Physics*, 2:419 – 423, 2006.
- [78] A Kirk, I T Chapman, J Harrison, Yueqiang Liu, E Nardon et al. **Effect of resonant magnetic perturbations with toroidal mode numbers of 4 and 6 on edge-localized modes in single null H-mode plasmas in MAST.** *Plasma Physics and Controlled Fusion*, 55(1):015006, 2013.
- [79] L. R. Baylor, N. Commaux, T. C. Jernigan, S. J. Meitner, S. K. Combs et al. **Reduction of edge localized mode intensity on DIII-D by on-demand triggering with high frequency pellet in- jection and implications for ITER.** *Physics of Plasmas*, 20(8):–, 2013.
- [80] K H Burrell, M E Austin, D P Brennan, J C DeBoo, E J Doyle et al. **Quiescent H-mode plasmas in the DIII-D tokamak.** *Plasma Physics and Controlled Fusion*, 44(5A):A253, 2002.
- [81] R.J. Groebner, D.R. Baker, K.H. Burrell, T.N. Carlstrom, J.R. Fer- ron et al. **Progress in quantifying the edge physics of the H- mode regime in DIII-D.** *Nuclear Fusion*, 41(12):1789, 2001.
- [82] W Suttrop, M Maraschek, G D Conway, H-U Fahrbach, G Haas et al. **ELM-free stationary H-mode plasmas in the ASDEX Up- grade tokamak.** *Plasma Physics and Controlled Fusion*, 45(8):1399, 2003.
- [83] Y Sakamoto, H Shirai, T Fujita, S Ide, T Takizuka et al. **Impact of toroidal rotation on ELM behaviour in the H-mode on JT-60U.** *Plasma Physics and Controlled Fusion*, 46(5A):A299, 2004.

- [84] W. Suttrop, V. Hynönen, T. Kurki-Suonio, P.T. Lang, M. Maraschek et al. **Studies of the 'quiescent H-mode' regime in ASDEX Upgrade and JET.** *Nuclear Fusion*, 45(7):721, 2005.
- [85] K. H. Burrell, M. E. Austin, D. P. Brennan, J. C. DeBoo, E. J. Doyle et al. **Quiescent double barrier high-confinement mode plasmas in the DIII-D tokamak.** *Physics of Plasmas*, 8(5):2153–2162, 2001.
- [86] E J Doyle, L R Baylor, K H Burrell, T A Casper, J C DeBoo et al. **The quiescent double barrier regime in the DIII-D tokamak.** *Plasma Physics and Controlled Fusion*, 43(12A):A95, 2001.
- [87] C M Greenfield, K H Burrell, E J Doyle, R J Groebner, W P West et al. **The quiescent double barrier regime in DIII-D.** *Plasma Physics and Controlled Fusion*, 44(5A):A123, 2002.
- [88] F Troyon, R Gruber, H Saurenmann, S Semenzato and S Succi. **MHD-limits to plasma confinement.** *Plasma Physics and Controlled Fusion*, 26(1A):209, 1984.
- [89] N Oyama, P Gohil, L D Horton, A E Hubbard, J W Hughes et al. **Pedestal conditions for small ELM regimes in tokamaks.** *Plasma Physics and Controlled Fusion*, 48(5A):A171, 2006.
- [90] P.B. Snyder, K.H. Burrell, H.R. Wilson, M.S. Chu, M.E. Fenstermacher et al. **Stability and dynamics of the edge pedestal in the low collisionality regime: physics mechanisms for steady-state ELM-free operation.** *Nuclear Fusion*, 47(8):961, 2007.
- [91] T H Osborne, P B Snyder, K H Burrell, T E Evans, M E Fenstermacher et al. **Edge stability of stationary ELM-suppressed regimes on DIII-D.** *Journal of Physics: Conference Series*, 123(1):012014, 2008.
- [92] K. H. Burrell, T. H. Osborne, P. B. Snyder, W. P. West, M. E. Fenstermacher et al. **Quiescent H-mode plasmas with strong edge rotation in the cocurrent direction.** *Physical Review Letters*, 102:155003, Apr 2009.
- [93] A.M. Garofalo, W.M. Solomon, J.-K. Park, K.H. Burrell, J.C. DeBoo et al. **Advances towards QH-mode viability for ELM-stable operation in ITER.** *Nuclear Fusion*, 51(8):083018, 2011.
- [94] K.H. Burrell, A.M. Garofalo, W.M. Solomon, M.E. Fenstermacher, D.M. Orlov et al. **Quiescent H-mode operation using torque from non-axisymmetric, non-resonant magnetic fields.** *Nuclear Fusion*, 53(7):073038, 2013.
- [95] M. Greenwald, R. Boivin, P. Bonoli, R. Budny, C. Fiore et al. **Characterization of enhanced  $D_\alpha$  high-confinement modes in Alcator C-Mod.** *Physics of Plasmas*, 6(5):1943–1949, 1999.

- [96] A. E. Hubbard, R. L. Boivin, R. S. Granetz, M. Greenwald, J. W. Hughes et al. **Pedestal profiles and fluctuations in C-Mod enhanced D-alpha H-modes.** *Physics of Plasmas*, 8(5):2033–2040, 2001.
- [97] Jerry W. Hughes. *Edge Transport Barrier Studies On the Alcator C-Mod Tokamak*. PhD thesis, Massachusetts Institute of Technology, 2005.
- [98] A. E. Hubbard, R. L. Boivin, R. S. Granetz, M. Greenwald, I. H. Hutchinson et al. **Measurements of the high confinement mode pedestal region on Alcator C-Mod.** *Physics of Plasmas*, 5(5):1744–1751, 1998.
- [99] J. W. Hughes, D. A. Mossessian, A. E. Hubbard, B. LaBombard and E. S. Marmar. **Observations and empirical scalings of the high-confinement mode pedestal on Alcator C-Mod.** *Physics of Plasmas*, 9(7):3019–3030, 2002.
- [100] J. W. Hughes, B. LaBombard, D. A. Mossessian, A. E. Hubbard, J. Terry et al. **Advances in measurement and modeling of the high-confinement-mode pedestal on the Alcator C-Mod tokamak.** *Physics of Plasmas*, 13(5):056103, 2006.
- [101] D A Mossessian, P B Snyder, M Greenwald, J W Hughes, Y Lin et al. **H-mode pedestal characteristics and MHD stability of the edge plasma in Alcator C-Mod.** *Plasma Physics and Controlled Fusion*, 44(4):423, 2002.
- [102] J. W. Hughes, A. E. Hubbard, D. A. Mossessian, B. LaBombard, T. M. Biewer et al. **H-mode pedestal and L-H transition studies on Alcator C-Mod.** *Fusion Science and Technology*, 51(3):317–341, 2007.
- [103] A. E. Hubbard, J. W. Hughes, I. O. Bespamyatnov, T. Biewer, I. Cziegler et al. **H-mode pedestal and threshold studies over an expanded operating space on Alcator C-Mod.** *Physics of Plasmas*, 14(5):056109, 2007.
- [104] J.W. Hughes, B. LaBombard, J. Terry, A. Hubbard and B. Lipschultz. **Edge profile stiffness and insensitivity of the density pedestal to neutral fuelling in Alcator C-Mod edge transport barriers.** *Nuclear Fusion*, 47(8):1057, 2007.
- [105] J.L. Terry, N.P. Basse, I. Cziegler, M. Greenwald, O. Grulke et al. **Transport phenomena in the edge of Alcator C-Mod plasmas.** *Nuclear Fusion*, 45(11):1321, 2005.
- [106] D. A. Mossessian, P. Snyder, A. Hubbard, J. W. Hughes, M. Greenwald et al. **High-confinement-mode edge stability**

- of Alcator C-mod plasmas.** *Physics of Plasmas*, 10(5):1720–1726, 2003.
- [107] A. Mazurenko, M. Porkolab, D. Mossessian, J. A. Snipes, X. Q. Xu et al. **Experimental and theoretical study of quasicoherent fluctuations in enhanced D<sub>α</sub> plasmas in the Alcator C-Mod tokamak.** *Physical Review Letters*, 89:225004, Nov 2002.
- [108] J.W. Hughes, A. Loarte, M.L. Reinke, J.L. Terry, D. Brunner et al. **Power requirements for superior H-mode confinement on Alcator C-Mod: experiments in support of ITER.** *Nuclear Fusion*, 51(8):083007, 2011.
- [109] B. LaBombard, J.E. Rice, A.E. Hubbard, J.W. Hughes, M. Greenwald et al. **Transport-driven scrape-off-layer flows and the boundary conditions imposed at the magnetic separatrix in a tokamak plasma.** *Nuclear Fusion*, 44(10):1047, 2004.
- [110] C. Fenzi, G. R. McKee, R. J. Fonck, K. H. Burrell, T. N. Carlstrom et al. **Effect of ion  $\nabla B$  drift direction on density fluctuation poloidal flow and flow shear.** *Physics of Plasmas*, 12(6):062307, 2005.
- [111] B. LaBombard, J. W. Hughes, N. Smick, A. Graf, K. Marr et al. **Critical gradients and plasma flows in the edge plasma of Alcator C-Mod.** *Physics of Plasmas*, 15(5):056106, 2008.
- [112] T N Carlstrom, K H Burrell and R J Groebner. **Comparison of a  $\nabla B$  drift effect model with measured H-mode power thresholds.** *Plasma Physics and Controlled Fusion*, 40(5):669, 1998.
- [113] R J Groebner and T N Carlstrom. **Critical edge parameters for H-mode transition in DIII-D.** *Plasma Physics and Controlled Fusion*, 40(5):673, 1998.
- [114] F Ryter, W Suttrop, B Brüsehaber, M Kaufmann, V Mertens et al. **H-mode power threshold and transition in ASDEX Upgrade.** *Plasma Physics and Controlled Fusion*, 40(5):725, 1998.
- [115] D.G. Whyte, A.E. Hubbard, J.W. Hughes, B. Lipschultz, J.E. Rice et al. **I-mode: an H-mode energy confinement regime with L-mode particle transport in Alcator C-Mod.** *Nuclear Fusion*, 50(10):105005, 2010.
- [116] A. E. Hubbard, D. G. Whyte, R. M. Churchill, I. Cziegler, A. Dominguez et al. **Edge energy transport barrier and turbulence in the I-mode regime on Alcator C-Mod.** *Physics of Plasmas*, 18(5):056115, 2011.
- [117] A.E. Hubbard, D.G. Whyte, R.M. Churchill, A. Dominguez, J.W. Hughes et al. **Threshold conditions for transitions to I-mode**

- and H-mode with unfavourable ion grad B drift direction. *Nuclear Fusion*, 52(11):114009, 2012.
- [118] Arturo Dominguez. *Study of Density Fluctuations and Particle Transport at the Edge of I-Mode Plasmas*. PhD thesis, Massachusetts Institute of Technology, 2012.
- [119] A. Hubbard, E. Marmar, S. Baek, I. Cziegler, A. Dominguez et al. Progress in performance and understanding of steady ELM-free I-modes on Alcator C-Mod. In *24th IAEA Fusion Energy Conference*, number EX/1-3, 2012.
- [120] N. T. Howard, M. Greenwald and J. E. Rice. Characterization of impurity confinement on Alcator C-Mod using a multi-pulse laser blow-off system. *Review of Scientific Instruments*, 82(3):–, 2011.
- [121] Rachael M. McDermott. *Edge Radial Electric Field Studies via Charge Exchange Recombination Spectroscopy on the Alcator C-Mod Tokamak*. PhD thesis, Massachusetts Institute of Technology, 2009.
- [122] C Theiler, R M Churchill, B Lipschultz, M Landreman, D R Ernst et al. Inboard and outboard radial electric field wells in the H- and I-mode pedestal of Alcator C-Mod and poloidal variations of impurity temperature. accepted to *Nuclear Fusion*, 2014.
- [123] J. E. Rice, J. W. Hughes, P. H. Diamond, Y. Kosuga, Y. A. Podpaly et al. Edge temperature gradient as intrinsic rotation drive in Alcator C-Mod tokamak plasmas. *Physical Review Letters*, 106:215001, May 2011.
- [124] I. Cziegler, P. H. Diamond, N. Fedorczak, P. Manz, G. R. Tynan et al. Fluctuating zonal flows in the I-mode regime in Alcator C-Mod. *Physics of Plasmas*, 20(5):–, 2013.
- [125] A.E. White, P. Phillips, D.G. Whyte, A.E. Hubbard, C. Sung et al. Electron temperature fluctuations associated with the weakly coherent mode in the edge of I-mode plasmas. *Nuclear Fusion*, 51(11):113005, 2011.
- [126] Istvan Cziegler. *Turbulence and Transport Phenomena in Edge and Scrape-Off Layer Plasmas*. PhD thesis, Massachusetts Institute of Technology, 2011.
- [127] B. Coppi and T. Zhou. Plasma confinement regimes and collective modes characterizing them. *Physics of Plasmas*, 19(10):102509, 2012.

- [128] B. Coppi and T. Zhou. Interpretation of the I-regime and transport associated with relevant heavy particle modes. *Physics of Plasmas*, 19(1):012302, 2012.

# 3

## PEDESTAL MODELING AND THEORY

---

While a number of high-performance regimes (described in chapter 2) have been established and are actively explored for tokamak operation, much of the physics governing these regimes is still unknown. In particular, the physics underlying the structure of the pedestal is an area of active research, due in large part to the inherent difficulty in experimentally diagnosing the pedestal plasma as it varies over short scale lengths, and in the wide variability of H-mode behaviors observed in tokamak experiments. Nevertheless confidence in the prediction of pedestal height and stability for ITER- and reactor-scale devices is essential: core temperature and pressure in the plasma are strongly sensitive to pedestal conditions due to profile stiffness driven by marginally-stable temperature-gradient modes [1], thus fusion power density is controlled by the pressure pedestal structure. Moreover, operation with large, uncontrolled Edge-Localized Modes (ELMs – see section 2.2) can drive transient heat loads exceeding wall material tolerances on ITER-scale devices [2, 3] – an understanding of pedestal stability against ELMs is necessary for ITER operation and beyond. This chapter provides a review of the efforts to date in theory and modeling of the pedestal, including the theoretical models used in the balance of this thesis.

*elaborate or reword*

• *elaborate?*

### 3.1 EARLY MODELS

*needs better title...*

Initial efforts in understanding the pedestal took a variety of approaches, including models built from fairly simple *ansätze* for the physics determining the pedestal structure. Several of these approaches are detailed here. Overviews of these models may also be found in [4, 5, §2].

#### 3.1.1 *Empirical Observations*

Absent a firm understanding of the physics underlying the pedestal structure, experimental efforts have sought to characterize the pedestal in terms of simple scalings with engineering parameters. The pedestal width, in particular, presented significant difficulty in this regard, as it tends to be quite robust, varying only over a narrow range on a given machine [6] – observations on JET [7] and Alcator C-Mod [8, 9] found minimal variation of the pedestal width with plasma current or magnetic field, although a somewhat broader pedestal was observed at low current and with strong shaping on C-Mod [9, 10]. Accordingly,

the measured gradients in density, temperature, and pressure in the steepest region of the pedestal trend linearly with the corresponding value at the pedestal top [7, 9].

Multivariate dependences on engineering parameters may be explored with a reasonably general approach via power-law scalings, fitting pedestal data to scalings agnostic of any assumed underlying physics. Suttrop *et al.* [11] found for ASDEX Upgrade pedestals

$$\nabla p \sim B_T^{-0.31} P_{\text{tot}}^{0.16} \bar{n}_e^{-0.1} I_p^{2.1} \quad (3.1)$$

A similar approach on C-Mod using an extensive dataset of EDA and ELM-free H-modes [8] found

$$\begin{aligned} n_{e,\text{ped}} &\sim I_p^{0.95} \bar{n}_{e,L}^{0.39} B_T^{-0.46} \\ T_{e,\text{ped}} &\sim I_p^{0.95} \bar{n}_{e,L}^{-0.78} B_T^{0.80} P_{\text{net}}^{0.64} \\ p_{e,\text{ped}} &\sim I_p^{1.98} \bar{n}_{e,L}^{-0.56} P_{\text{net}}^{0.48} \end{aligned} \quad (3.2)$$

(here  $\bar{n}_{e,L}$  is the L-mode target density, as pedestal density is not readily controllable in EDA H-mode). However, later studies asserted that the magnetic-field dependence was overstated in the above [12]. While these empirical models perform reasonably well on their respective experimental data, confident extrapolation to ITER-scale operation requires a physics-based understanding of the pedestal structure.

### 3.1.2 Neutral Penetration & the Density Pedestal

Given the proximity of the plasma pedestal to neutral gas from fueling apparatus and wall outgassing in the edge, it is logical that the density profile should depend strongly on interaction with and ionization of neutral particles in the pedestal. Based on a relatively simple particle transport model, the pedestal width is expected to scale with the characteristic neutral penetration length before ionization [5, 13]:

$$\lambda_{\text{neutral}} = \frac{v_n}{n_e \langle \sigma v \rangle_{\text{ion}}} \quad (3.3)$$

where  $v_n$  is the velocity of neutrals entering the pedestal (set by the neutral thermal temperature in the edge) and  $\langle \sigma v \rangle_{\text{ion}}$  is the velocity-averaged ionization cross-section. Given that  $v_n$  is independent of plasma conditions and that  $\langle \sigma v \rangle_{\text{ion}}$  is consistent over the temperatures of interest in the edge [5], therefore we expect the simple relation  $\Delta_n \sim 1/n_{e,\text{ped}}$ . More complex models for the neutral penetration typically reproduce the dependence on  $\lambda_{\text{neutral}}$ .

However, experimental observations of the density pedestal conflict with these relatively simple predictions. Observations in similarity experiments between DIII-D, JET, and ASDEX Upgrade [14] were inconsistent with the simple model: although DIII-D data were consistent with the trends found in the model, data from JET were not, and moreover the model predicted an inconsistent scaling between the two machines for pedestal density and width. Likewise, predictions based on pedestal widths set by neutral penetration performed poorly as a predictor for pedestal height in a multi-machine scaling from AUG, DIII-D, JT-60U, and JET [15]. EDA H-modes on Alcator C-Mod show near-complete insensitivity of the density pedestal to neutral interactions – the density pedestal instead saturates to a level dictated by plasma transport (predicted best by  $n_{e,ped} \sim I_p$ ), with fueling via edge gas puffing having little effect on the density pedestal [10, 12].

In addition to significant sensitivity to machine and discharge conditions and wall materials [14], density pedestal behavior appears to be strongly sensitive to magnetic configuration – experiments on MAST [6] found that, while the density pedestal width was poloidally constant in single-null discharges, the density pedestal is measurably broader on the outboard, low-field side in double-null discharges. These results indicate that plasma-neutral interactions in the density pedestal are quite complex, and dependent on poloidal transport behaviors and fueling asymmetries [6]. This remains an important area of research, as ITER is expected to have an edge that is highly opaque to neutrals, complicating the density pedestal structure and fueling scenarios for high-density plasmas [6, 10].

### 3.1.3 Ion-Orbit Loss & Gyroradius Models

Due to the importance in the edge  $E_r$  well in pedestal formation, modeling efforts naturally turned to potential sources for the electric field to explain the pedestal. One suggested source was ion orbit loss across the last closed flux surface, in which the gyro-motion of ions near the edge intersect the SOL or the plasma-facing material surfaces – the charge imbalance induced by this particle “leak” results in a radial electric field [16]. Assuming ion orbit losses drive the  $E_r$  well, the  $\vec{E} \times \vec{B}$  shear layer width ought to be governed by the banana orbit width, which scales as the poloidal gyroradius  $\rho_{i,pol} \sim \sqrt{T_i}/B_p$ . Accounting for the squeezing effect of the radial electric field on the banana orbit width, Shaing [17] gives for the well width

$$\Delta_{\vec{E} \times \vec{B}} \propto \sqrt{\varepsilon} \frac{\rho_{i,pol}}{\sqrt{S}} \quad (3.4)$$

$$S = \left| 1 - \frac{1}{B_p \omega_{ci,p}} \frac{dE_r}{dr} \right|$$

where  $S$  is the squeezing factor and  $\omega_{ci,p}$  is the ion cyclotron frequency evaluated with the poloidal field. The model is further refined by Itoh & Itoh [18] to include the broadening effects of viscosity shear. The predicted trend is observed in ELM-free H-modes on JT-60U [19], with  $\Delta \approx 3.3\sqrt{\epsilon}\rho_{i,pol}$ ; however, as the squeezing factor  $S$  is estimated to be near-unity, the pedestal width is broader by a factor of  $\sim 3.3$  than the  $\sim \sqrt{\epsilon}\rho_{i,pol}$  banana width. ELMy H-modes on JT-60U exhibit a similar scaling at weak shaping, with a broader pedestal and additional safety factor dependence  $\Delta \approx 5\rho_{i,pol}q_{95}^{-0.3}$  at higher triangularity [20].

However, other predictions and experimental observations contradict these results. Depending on the calculation method of growth rate suppression by  $\vec{E} \times \vec{B}$  sheared flow, the pedestal width may scale with the gyroradius anywhere from  $\Delta \sim (\rho^*)^{1/2}$  to  $\Delta \sim \rho^*$ , where  $\rho^*$  indicates the gyroradius normalized to the plasma minor radius [14, 15]. Alternately, stabilization of drift-ballooning modes leads to a predicted dependence of  $\Delta \sim \rho_{i,pol}^{2/3}$  [21]; similarly, diamagnetic stabilization in the pedestal leads to the prediction of  $\Delta \sim I_p^2 \rho_{i,pol}^{2/3}$  [22]. Observations on DIII-D [23] found a dependence of  $\Delta/R \sim (\rho_{i,pol}/R)^{0.67}$ , while observations on ASDEX Upgrade [14, 24] found no gyroradius dependence for the pedestal width.

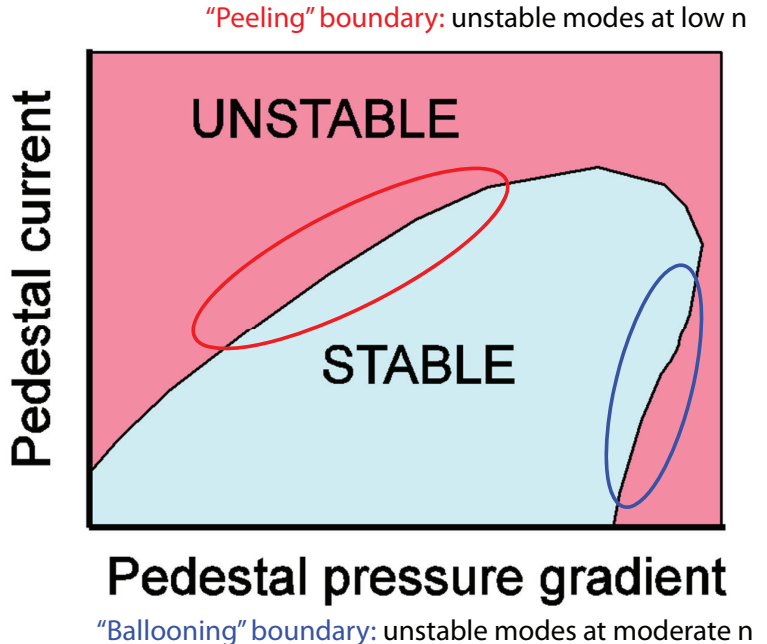
Distinguishing between these scalings is difficult given the diagnostic complications inherent in pedestal measurements, and the narrow range over which  $\rho_i$  or the pedestal and  $E_r$  well width vary on a given machine [6, 25]. Moreover, alternate models propose a scaling with poloidal beta at the pedestal top, rather than poloidal gyroradius, with trends of width of  $\Delta \sim \beta_{p,ped}^{0.4}$  to  $\sim \beta_{p,ped}^{0.5}$  observed on DIII-D [23, 26], JET [6], JT=60U [27], and ASDEX Upgrade [14]. Due to the strong covariance between  $\rho_{i,pol} \sim \sqrt{mT}/I_p$  and  $\sqrt{\beta_{p,ped}} \sim \sqrt{nT}/I_p$  these trends are quite difficult to separate. However, dedicated experiments to separate the two, either via pumping to vary density and temperature at fixed pressure, exploiting the density dependence in  $\beta_{p,ped}$  [23], or via isotope variation targeting the mass dependence in  $\rho_{i,pol}$  [27, 28], found the  $\beta_{p,ped}$  scaling to be the better predictor, with a weaker secondary gyroradius dependence  $\Delta \sim \rho_{i,pol}^{0.2} \beta_{p,ped}^{0.5}$  [6, 27]. The physics underlying the  $\Delta \sim \sqrt{\beta_{p,ped}}$  scaling will be discussed in detail in section 3.3. •

### 3.2 MHD STABILITY: PEELING-BALLOONING MODES

*pull other cites!*

Early observations of the pedestal in ELMy H-mode identified ballooning MHD instabilities as a possible driver for the ELM instability. Numerous experiments identified a pressure-gradient effect tied to the ELM trigger [29], with the value of the pressure gradient at the ELM trigger increased with plasma current and increased shaping consistent with ballooning MHD behavior [24].

**Figure 3.1:** Schematic of the stability space to coupled peeling-balloonning MHD modes, set by the edge pressure gradient and current density. Ballooning modes are driven by pressure gradient but stabilized by magnetic shear driven by edge currents, while kink/peeling modes are current-driven but stabilized by pressure gradients. [Ref to Snyder?](#)



### 3.2.1 Ballooning MHD

- EDA H-mode modeled to be ideal-balloonning stable; P-B only describes ELMy H-mode [30]
- increased triangularity reduces  $\nabla p$ ,  $n_{e,ped}$  in EDA; contrast with ELMy, where shape stabilizes P-B modes, seems to destabilize QCM earlier in EDA [9]

### 3.2.2 Peeling MHD

### 3.2.3 ELITE Code

## 3.3 KINETIC-BALLOONING TURBULENCE MODELING

## 3.4 THE EPED MODEL

**Figure 3.2:** Illustration of the peeling-balloon MHD and kinetic-balloon turbulent constraints used in the EPED model. The peeling-balloon constraint, calculated by ELITE, results in a trend roughly of  $p_{\text{ped}} \sim \Delta_{\psi}^{3/4}$ , while the KBM width constraint calculated via the ballooning-critical pedestal (BCP) technique sets  $p_{\text{ped}} \sim \Delta_{\psi}^2$ . The unique solution to these constraints is the EPED prediction for the pedestal width and height. The prediction is here shown compared to the measured pedestal from DIII-D shot 132003 (reproduced from [31]) [get permission](#)

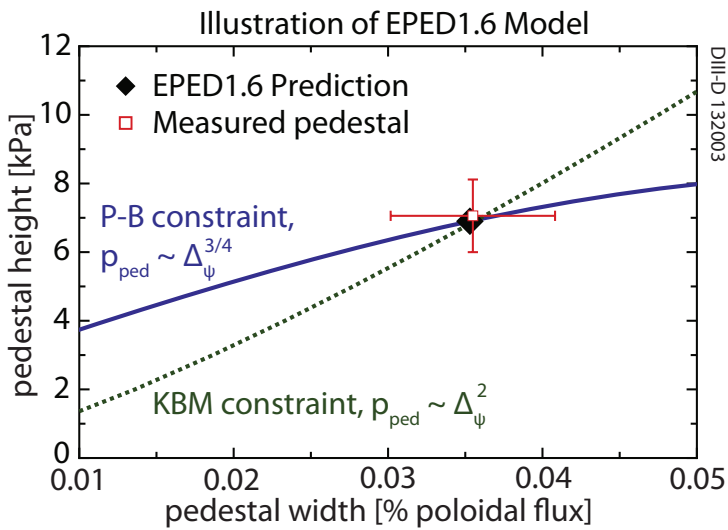
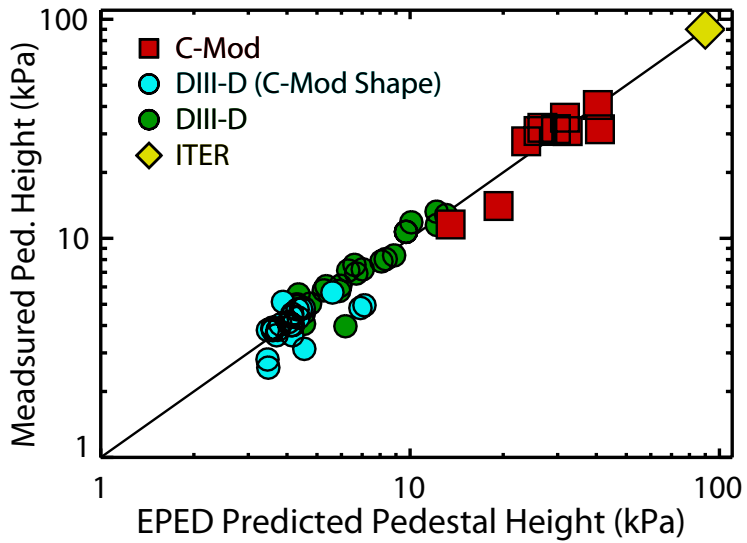


**Figure 3.3:** EPED predictions versus measured pressure pedestal heights from DIII-D and C-Mod, spanning a significant range of pedestal pressures. Notably, C-Mod pressure pedestals reach within a factor of  $\sim 2$  of the predicted ITER pedestal height. [ref to Hughes paper](#)



## BIBLIOGRAPHY

---

- [1] A. E. Hubbard, R. L. Boivin, R. S. Granetz, M. Greenwald, I. H. Hutchinson et al. **Measurements of the high confinement mode pedestal region on Alcator C-Mod.** *Physics of Plasmas*, 5(5):1744–1751, 1998.
- [2] A Loarte, G Saibene, R Sartori, D Campbell, M Becoulet et al. **Characteristics of type I ELM energy and particle losses in existing devices and their extrapolation to ITER.** *Plasma Physics and Controlled Fusion*, 45(9):1549, 2003.
- [3] G Federici, A Loarte and G Strohmayer. **Assessment of erosion of the ITER divertor targets during type I ELMs.** *Plasma Physics and Controlled Fusion*, 45(9):1523, 2003.
- [4] A E Hubbard. **Physics and scaling of the H-mode pedestal.** *Plasma Physics and Controlled Fusion*, 42(5A):A15, 2000.
- [5] Jerry W. Hughes. *Edge Transport Barrier Studies On the Alcator C-Mod Tokamak.* PhD thesis, Massachusetts Institute of Technology, 2005.
- [6] C.F. Maggi. **Progress in understanding the physics of the H-mode pedestal and ELM dynamics.** *Nuclear Fusion*, 50(6):066001, 2010.
- [7] P Breger, C Flewin, K-D Zastrow, S J Davies, N C Hawkes et al. **Plasma-edge gradients in L-mode and ELM-free H-mode JET plasmas.** *Plasma Physics and Controlled Fusion*, 40(3):347, 1998.
- [8] J. W. Hughes, D. A. Mossessian, A. E. Hubbard, B. LaBombard and E. S. Marmar. **Observations and empirical scalings of the high-confinement mode pedestal on Alcator C-Mod.** *Physics of Plasmas*, 9(7):3019–3030, 2002.
- [9] J. W. Hughes, A. E. Hubbard, D. A. Mossessian, B. LaBombard, T. M. Biewer et al. **H-mode pedestal and L-H transition studies on Alcator C-Mod.** *Fusion Science and Technology*, 51(3):317–341, 2007.
- [10] J.W. Hughes, B. LaBombard, J. Terry, A. Hubbard and B. Lipschultz. **Edge profile stiffness and insensitivity of the density pedestal to neutral fuelling in Alcator C-Mod edge transport barriers.** *Nuclear Fusion*, 47(8):1057, 2007.
- [11] W Suttrop, M Kaufmann, H J de Blank, B Brüsehaber, K Lackner et al. **Identification of plasma-edge-related operational**

- regime boundaries and the effect of edge instability on confinement in ASDEX Upgrade. *Plasma Physics and Controlled Fusion*, 39(12):2051, 1997.
- [12] J. W. Hughes, B. LaBombard, D. A. Mossessian, A. E. Hubbard, J. Terry et al. Advances in measurement and modeling of the high-confinement-mode pedestal on the Alcator C-Mod tokamak. *Physics of Plasmas*, 13(5):056103, 2006.
  - [13] M.A. Mahdavi, T.H. Osborne, A.W. Leonard, M.S. Chu, E.J. Doyle et al. High performance H mode plasmas at densities above the Greenwald limit. *Nuclear Fusion*, 42(1):52, 2002.
  - [14] M. N. A. Beurskens, T. H. Osborne, P. A. Schneider, E. Wolfrum, L. Frassinetti et al. H-mode pedestal scaling in DIII-D, ASDEX Upgrade, and JET. *Physics of Plasmas*, 18(5):056120, 2011.
  - [15] T. Onjun, G. Bateman, A. H. Kritz and G. Hammett. Models for the pedestal temperature at the edge of H-mode tokamak plasmas. *Physics of Plasmas*, 9(12):5018–5030, 2002.
  - [16] K. C. Shaing, E. C. Crume and W. A. Houlberg. Bifurcation of poloidal rotation and suppression of turbulent fluctuations: A model for the L-H transition in tokamaks. *Physics of Fluids B: Plasma Physics*, 2(6):1492–1498, 1990.
  - [17] K. C. Shaing. Poloidal magnetic field dependence of the edge electric field layer width in the H mode in tokamaks. *Physics of Fluids B: Plasma Physics*, 4(2):290–291, 1992.
  - [18] Kimitaka Itoh and Sanae-I Itoh. The role of the electric field in confinement. *Plasma Physics and Controlled Fusion*, 38(1):1, 1996.
  - [19] T Hatae, Y Kamada, S Ishida, T Fukuda, T Takizuka et al. Characteristics of edge pedestal width in JT-60U ELM-free H-mode plasmas. *Plasma Physics and Controlled Fusion*, 40(6):1073, 1998.
  - [20] Y Kamada, T Hatae, T Fukuda and T Takizuka. Growth of the edge pedestal in JT-60U ELMy H-mode. *Plasma Physics and Controlled Fusion*, 41(11):1371, 1999.
  - [21] H R Wilson and J W Connor. Ballooning instabilities, poloidal flow and the temperature pedestal at the tokamak edge. In *Proceedings of the 24th European Physical Society Conference on Controlled Fusion and Plasma Physics*, volume 21A of *Europhysics Conference Abstracts*, pages 289–292, Geneva, 1997.
  - [22] B. N. Rogers and J. F. Drake. Diamagnetic stabilization of ideal ballooning modes in the edge pedestal. *Physics of Plasma*, 6(7):2797–2801, 1999.

- [23] T H Osborne, R J Groebner, L L Lao, A W Leonard, R Maingi et al. **H-mode pedestal characteristics, ELMs, and energy confinement in ITER shape discharges on DIII-D.** *Plasma Physics and Controlled Fusion*, 40(5):845, 1998.
- [24] W Suttrop, O Gruber, B Kurzan, H D Murmann, J Neuhauser et al. **Effect of plasma shape variation on ELMs and H-mode pedestal properties in ASDEX upgrade.** *Plasma Physics and Controlled Fusion*, 42(5A):A97, 2000.
- [25] P. Gohil, K.H. Burrell and T.N. Carlstrom. **Parametric dependence of the edge radial electric field in the DIII-D tokamak.** *Nuclear Fusion*, 38(1):93, 1998.
- [26] R. J. Groebner and T. H. Osborne. **Scaling studies of the high mode pedestal.** *Physics of Plasmas*, 5(5):1800–1806, 1998.
- [27] H. Urano, T. Takizuka, Y. Kamada, N. Oyama, H. Takenaga et al. **Dimensionless parameter dependence of H-mode pedestal width using hydrogen and deuterium plasmas in JT-60U.** *Nuclear Fusion*, 48(4):045008, 2008.
- [28] G. Saibene, L.D. Horton, R. Sartori, B. Balet, S. Clement et al. **The influence of isotope mass, edge magnetic shear and input power on high density ELMMy H modes in JET.** *Nuclear Fusion*, 39(9):1133, 1999.
- [29] Y Kamada, R Yoshino, Y Neyatani, M Sato, S Tokuda et al. **Onset condition for ELMs in JT-60U.** *Plasma Physics and Controlled Fusion*, 38(8):1387, 1996.
- [30] D A Mossessian, P B Snyder, M Greenwald, J W Hughes, Y Lin et al. **H-mode pedestal characteristics and MHD stability of the edge plasma in Alcator C-Mod.** *Plasma Physics and Controlled Fusion*, 44(4):423, 2002.
- [31] P.B. Snyder, R.J. Groebner, J.W. Hughes, T.H. Osborne, M. Beurskens et al. **A first-principles predictive model of the pedestal height and width: development, testing and ITER optimization with the EPED model.** *Nuclear Fusion*, 51(10):103016, 2011.



# 4

## ELMY H-MODES ON C-MOD

The ELMY H-mode [1, 2], described in section 2.2, is the most commonly accessed high-performance regime on major tokamak experiments. The bursty transport driven by ELMs provides sufficient relaxation of the particle confinement in H-mode to allow stationary operation without excessive impurity accumulation; as such, the ELMY H-mode is considered the baseline operating regime for ITER [3, 4]. However, on ITER-scale devices the pulsed heat loading associated with ELMs drives unacceptable levels of erosion and damage to plasma-facing wall and divertor materials [5, 6].

In light of the impact of large, deleterious ELMs on the ITER wall, and the profound impact of pedestal height on overall plasma performance [7, 8], a firm understanding of the physics governing the pedestal in high-performance regimes and their extrapolation to reactor-scale devices is of paramount importance to fusion research leading up to ITER operation. To that end, a Joint Research Target combining theory, experiment, and modeling efforts in the ELMY H-mode pedestal was undertaken [9, 10]. Notably, this effort saw the development of the EPED model [11, 12, 13], described in section 3.4, which predicts the pressure pedestal width and height preceding the ELM crash through a combination of constraints based on peeling-balloonning MHD instability [14, 15, 16] (section 3.2) and kinetic-balloonning turbulence [17] (section 3.3). In this chapter, we detail the contributions from Alcator C-Mod to this joint effort [18] both in empirical studies of the ELMY H-mode pedestal, and in the implementation of the EPED model. C-Mod ELMY H-modes greatly expand the parameter space in which the EPED model is tested, reaching within a factor of two of the target pedestal pressure for ITER. The techniques developed in this analysis will subsequently be applied to I-mode pedestals.

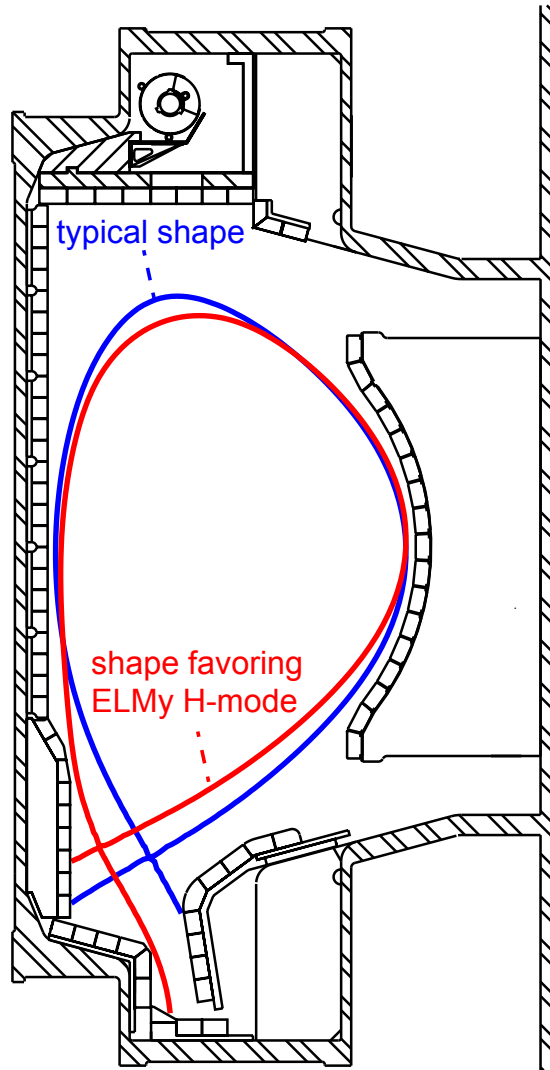
how to emphasize  
my own  
contribution?

reward

### 4.1 ELMY H-MODE ACCESS & EXPERIMENTAL ARRANGEMENT

High-confinement operation on Alcator C-Mod differs is unique among major tokamak experiments in that typical H-modes do not exhibit the large Type-I ELMs customarily seen on other devices [20]. Instead, ELM-free H-modes tend to form at lower collisionalities heating power levels, with high-density, high-power operation tending towards the continuously-regulated EDA H-mode rather than exhibiting discrete ELMs (see sections 2.1 and 2.3.2). However, by operating in a modified shape (see fig. 4.1) with low elongation,  $\kappa \sim 1.4 - 1.5$ ,

**Figure 4.1:** C-Mod cross-section comparing the typical plasma shape (blue) to the altered shape favoring ELMy H-mode operation (red), developed in joint experiments with the JFT-2M tokamak [19]. ELMy H-mode access is favored by high lower triangularity and an outer strike point in the divertor slot, coupled with very low upper triangularity and elongation. This is thought to reduce the required edge pressure gradient and current to reach the peeling-balloonning boundary.



and upper triangularity ( $\delta_u \sim 0.15$ ) paired with high lower triangularity ( $\delta_l > 0.75$ ) and a strike point on the divertor floor, regular ELMy H-mode operation is attainable. This comparatively weak shaping, developed in similarity experiments with the JFT-2M tokamak [21, 22], reduces the necessary pressure gradient and bootstrap current to reach the ideal peeling-balloonning MHD stability boundary (described in section 3.2), triggering the ELM. In this shape, new experiments on C-Mod [18] attained ELMy H-modes across a broad range in current (400 – 1100 kA) and field (3.5 – 8 T) with high-resolution pedestal data.

Pedestal profiles are taken with the edge Thomson scattering system, detailed in appendix A.1.2. The pedestal data is taken over steady ELMing phases to minimize the effects of random scatter in the data – an example of such a window, with line-averaged density  $\bar{n}_e$ , core and edge  $T_e$ , and divertor  $D_\alpha$  signal (indicative of the ELM crash), is shown in fig. 4.2, with a comparison of the individual-frame fits to

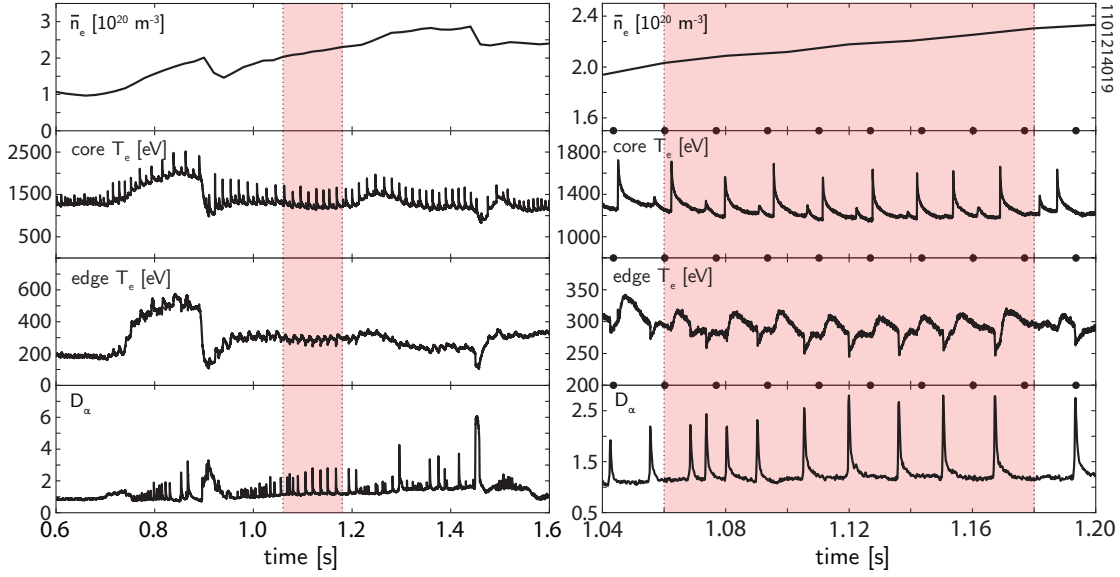


**Figure 4.2:** Example ELMy H-mode window (highlighted). Phases for study are selected for steady density ( $\bar{n}_e$  shown in the top trace), temperature (ECE  $T_e$  signals shown for the core and pedestal), and ELM cycles ( $D_\alpha$  signal shown). The same modeling window is shown zoomed-in at the right. Note the strong perturbation to the edge temperature due to the sawtooth crash. Thomson scattering frames are indicated by the black ticks on the axes – the ELM cycle is at a comparable frequency,  $\sim 60$  Hz, to the TS system frame rate. This presents a difficulty for selecting data masked to the “peak” of the ELM cycle, necessitating long, steady ELMing phases for study.

the ensemble shown in fig. 4.3. Strictly, models of the pedestal structure in ELMy H-mode predict the pedestal immediately preceding the ELM crash, when the pedestal is most unstable to the ELM trigger. However, ELMs on C-Mod typically cycle at  $60 - 100$  Hz, comparable to the repetition rate of the Thomson scattering system (as shown in figs. 4.2 and 4.3). This presents difficulties in resolving the pedestal with multiple frames per ELM and binning the data to the peaks of the ELM cycle. In most cases, pedestals are prepared in a single “ensemble average” utilizing all TS data in the window; in certain cases, a statistical set is also constructed using the last 20% of the ELM cycle as is typical for other machines. The results from this correction are discussed in section 4.2.

The electron density, temperature, and pressure profiles are fitted using a modified hyperbolic-tangent fit developed in [23]. In a general  $x, y$  space, the fitting function is expressed by

$$\begin{aligned} z &= \frac{x_0 - x}{\delta} \\ \text{mtanh}(\alpha, z) &= \frac{(1 + \alpha z)e^z - e^{-z}}{e^z + e^{-z}} \\ y &= \frac{h + b}{2} + \frac{h - b}{2} \text{mtanh}(\alpha, z) \end{aligned} \tag{4.1}$$

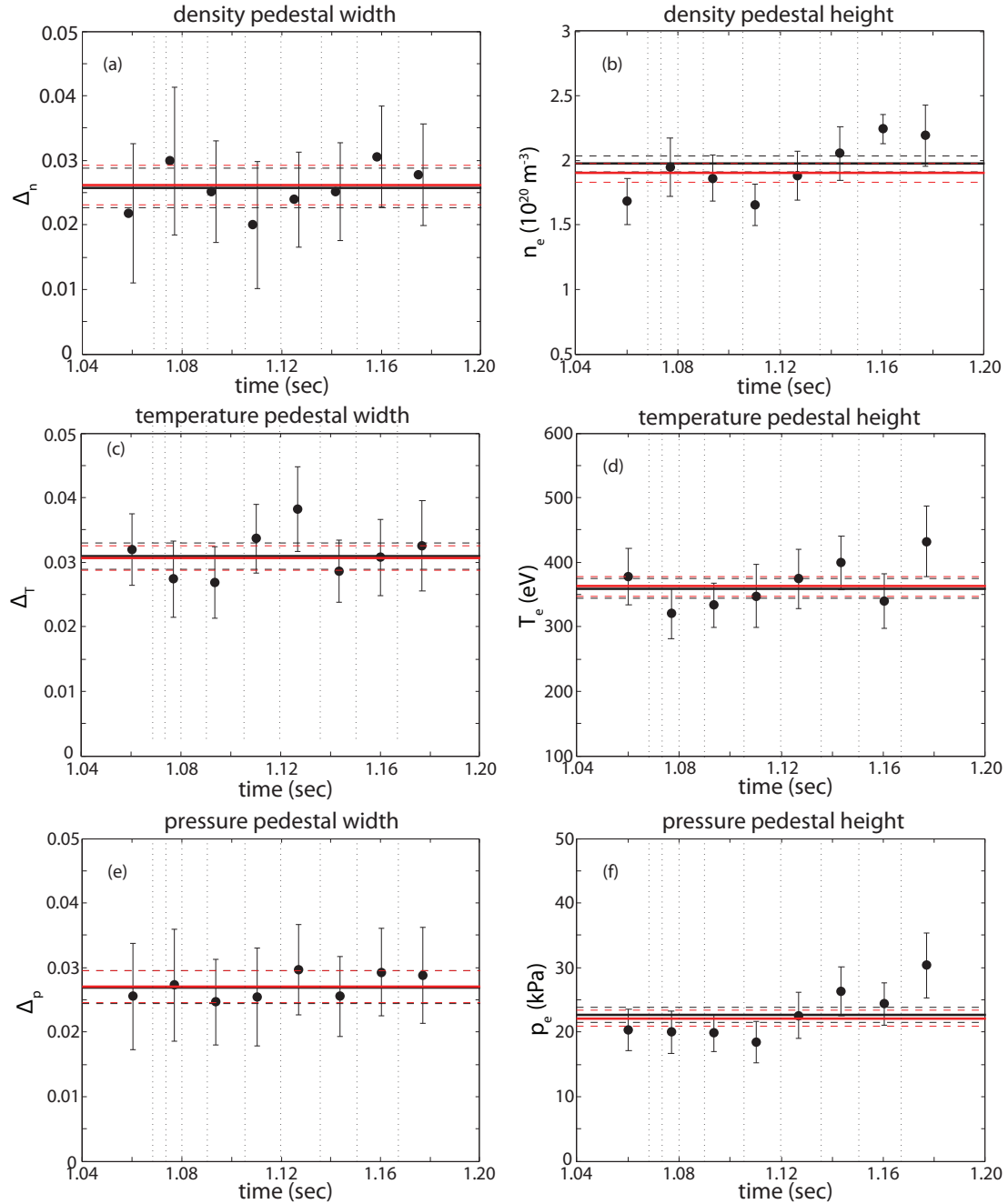
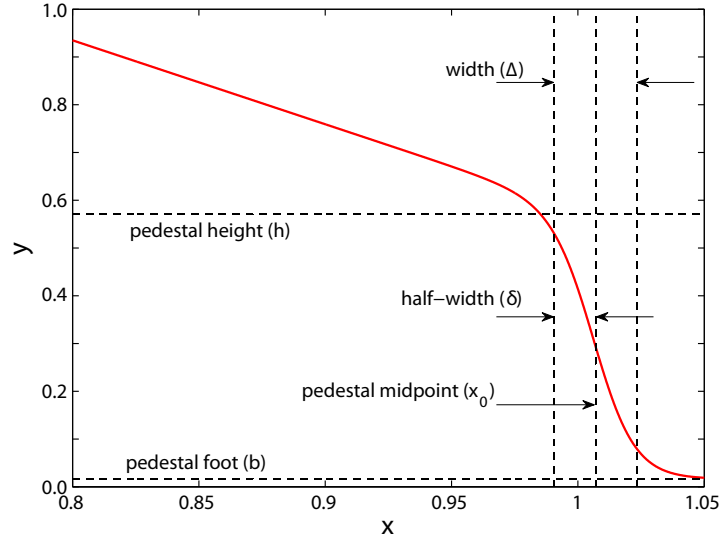


**Figure 4.3:** Comparison of fits for the  $n_e$ ,  $T_e$ , and  $p_e$  pedestal width and height from Thomson scattering. Individual frames of data are shown as black points, with their average shown by the black line (errorbars indicated by the dashes). The ensemble-averaged fit is shown in red. The ensemble fit captures the average behavior in a steady ELMing phase well, while suppressing the random scatter found in individual frames of TS data. For comparison, ELM crash times in the window are indicated by vertical dashed lines.

**Figure 4.4:** Example pedestal illustrating the  $\text{mtanh}$  function used for pedestal fitting (eq. (4.1)), defining the parameters: height  $h$ , baseline  $b$ , midpoint  $x_0$ , half-width  $\delta$ /full width  $\Delta$ . The inboard slope is characterized by the parameter  $\alpha$ .



where  $x_0$  is the pedestal midpoint,  $h$  and  $b$  are the height and baseline, and  $\delta$  is the half-width (we use  $\Delta = 2\delta$  as the “pedestal width”). The inboard slope is encoded by the parameter  $\alpha$ , with the multiplicative factor  $1 + \alpha z$  providing an approximately linear profile inboard from the steep-gradient region. This definition provides a smooth, continuous definition for the pedestal gradient throughout the profile, with the peak gradient found analytically at  $x_0$ . Recent H-mode studies use the fitting parameter  $h$  as the figure-of-merit for the pedestal height; however, it is also common to express the pedestal height in terms of the evaluated value of the fit at the 95% poloidal flux surface. For the purposes of this document we denote the height taken from the fitting parameter  $h$  by the subscript  $\text{ped}$ , and values taken at the 95% flux surface by the subscript  $95$ .

Due to the ready availability of high-resolution electron density and temperature diagnostics, for the purposes of this section we assume equal ion and electron pressures,  $p = 2n_e T_e$  (a viable approximation on C-Mod due to the relatively low impurity content found in ELMy H-modes,  $Z_{\text{eff}} \sim 2$ , and rapid ion-electron equilibration in H-mode pedestals on C-Mod [24]). All profiles are prepared using normalized poloidal flux for the abscissa, facilitating comparison to results from other machines and to the EPED model. For the purposes of the EPED model we also prepare an averaged width, defined by

$$\delta_\psi = \frac{\delta_{n_e} + \delta_{T_e}}{2} \quad \Delta_\psi = 2\delta_\psi \quad (4.2)$$

a practice necessitated by cases in which the density and temperature profile measurements are generated by distinct diagnostics (rather than taking both from the Thomson scattering system, as is customary on C-Mod). As the density and temperature widths are quite close

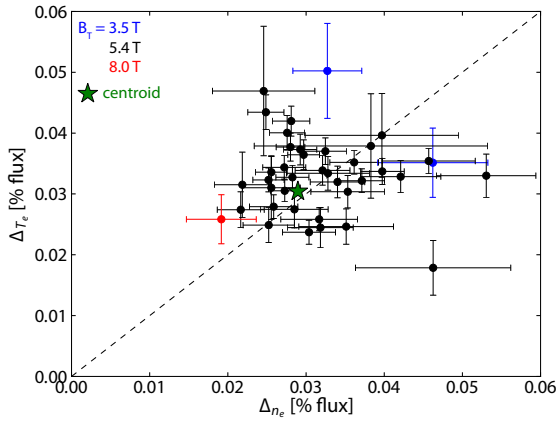


**Figure 4.5:** Comparison of the measured pedestal widths for the  $n_e$  and  $T_e$  pedestals, differentiated for the low-, standard-, and high-field H-mode cases. Pedestal widths are similar for density and temperature, although on average the density pedestal is slightly wider. The error-weighted centroid of the dataset is shown by the star.

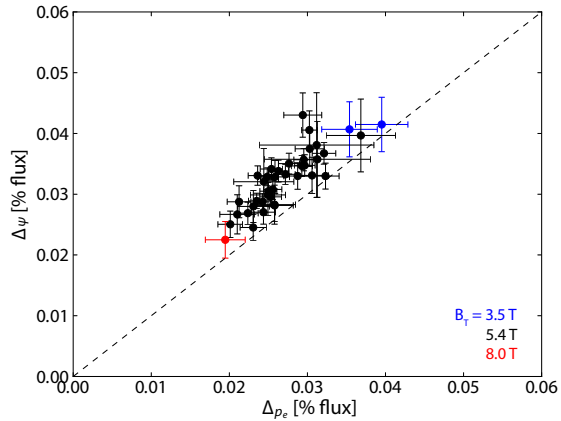


**Figure 4.6:** Comparison of the directly-measured pressure pedestal width and the EPED width  $\Delta_\Psi$ , defined as the average of  $\Delta_{n_e}$  and  $\Delta_{T_e}$ . The widths trend quite closely to one another, although  $\Delta_\Psi$  is systematically somewhat wider.

(although the density pedestal is, on average, slightly wider, as shown in fig. 4.5, with an average ratio of  $\Delta_{T_e}/\Delta_{n_e} = 1.051$ ), the difference between  $\Delta_\Psi$  and the directly-measured  $\Delta_{p_e}$  is minimal – as shown in fig. 4.6, the two widths are well-correlated, with  $\Delta_\Psi$  systematically slightly wider. •

#### 4.2 ELM CYCLE SYNCHRONIZATION

The common practice for modeling the ELMy H-mode pedestal is to take profile data immediately preceding the ELM crash (commonly, data from the last 20% of the ELM cycle), as this most closely corresponds to the pedestal profile at the stability limit associated with the ELM trigger. However, as the ELM cycle in H-mode on C-Mod is typically at a comparable repetition rate to the Thomson Scattering system (60 Hz), this practice is only possible on a subset of discharges, with sufficiently long, steady H-mode phases, such that a sufficient number of frames in the desired time window can be found.

A comparison between the ensemble-averaged and ELM-synchronized pressure pedestals (pedestal height  $p_{ped}$  and the pressure at the 95% flux surface  $p_{95}$ ) are shown in figs. 4.7 and 4.8. ELM synchronization finds an average 10.8% increase in the measured pressure  $p_{ped}$ , with a slightly lesser increase of 7.6% in  $p_{95}$ . This is consistent with the perturbation to the pressure pedestal by the ELM observed on other machines [5, 25]. The weaker perturbation due to the ELM crash observed at the 95% flux surface is also consistent with previous ELM observations – the ELM crash typically alters the pressure profile only

**Figure 4.7:** Comparison of the pressure pedestal height  $p_{ped}$  between the ensemble-averaged and ELM-synchronized profiles. On average, ELM synchronization results in a 10.8% increase in measured pedestal pressure, consistent with ELM losses observed on other machines. At lower pressures, ELMs are typically small enough that the perturbation is minimal; however, the distinction becomes important for the highest-pressure ELMy H-modes on C-Mod.

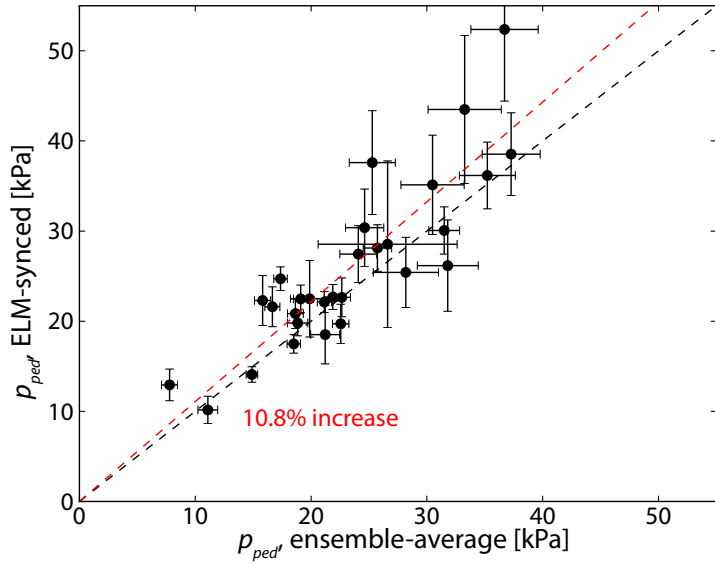
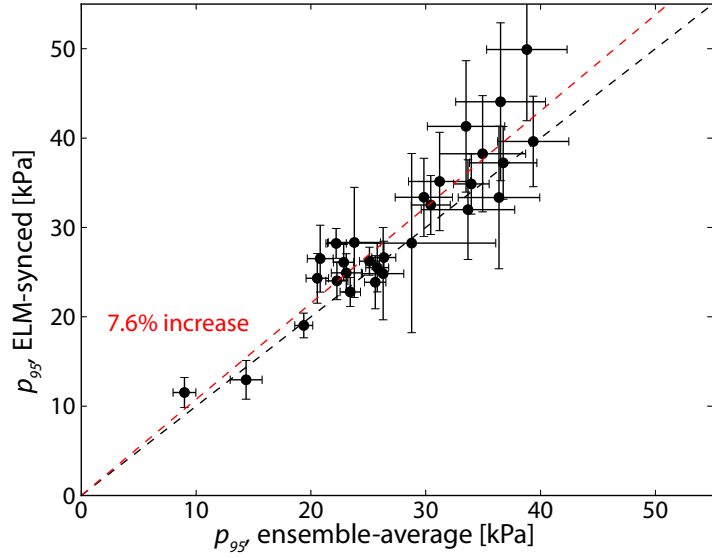


**Figure 4.8:** Comparison of the pressure at the 95% flux surface,  $p_{95}$ , between the ensemble-averaged and ELM-synchronized profiles. On average, ELM synchronization results in a 7.6% increase in the measured pressure. This is consistent with the ELM perturbation to the pedestal being largely restricted to the pedestal just within the steep-gradient region, with decreasing perturbation further into the plasma from the pedestal.



in a region just inside the steep-gradient region, with minimal perturbation to profiles in the plasma interior.

#### 4.3 EPED MODEL PREDICTIONS

The EPED model, described in section 3.4, combines pedestal limits based on coupled peeling-balloonning MHD instabilities [14, 15, 16] and kinetic-balloonning mode turbulence [17]. These models set two distinct constraints on the pedestal width and height, with peeling-balloonning MHD predicting  $p_{ped} \sim \Delta^{3/4}$  and kinetic-balloonning turbulence predicting  $p_{ped} \sim \Delta^2$ . The unique intersection of these two constraints provides a predictive value for the pedestal width and height. The most recent version of the model, EPED1.63, utilizes gy-

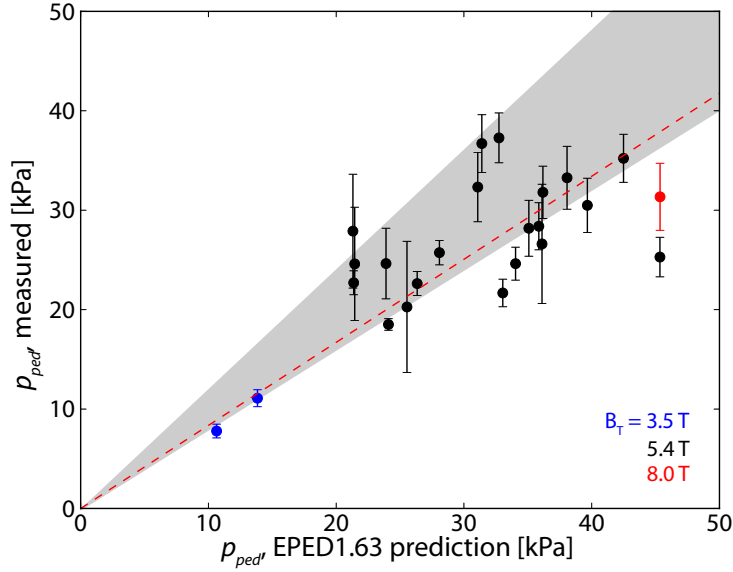
reference figure in  
chapter 3, probably

rokinetic calculations to more accurately constrain the KBM limit, and includes a modified term accounting for the strong diamagnetic stabilization of high- $n$  modes in the pedestal on C-Mod. A comparison between the observed and predicted pedestal parameters is presented here.

#### 4.3.1 Pedestal Height

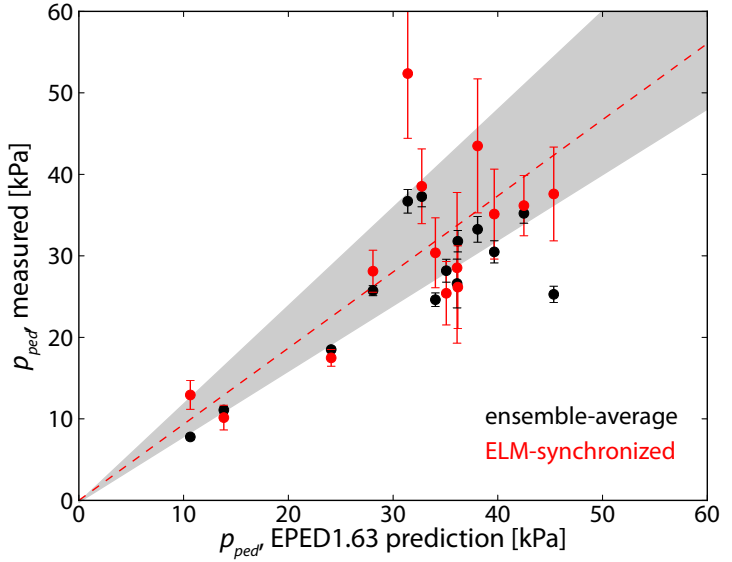
A comparison between the pressure pedestal height predicted by EPED1.63 and the observed height is shown in fig. 4.9. While most measured pedestals lie within the  $\pm 20\%$  expected error in the EPED prediction (indicated by the grey band in fig. 4.9), the EPED model systematically over-predicts the pedestal pressure, corresponding on average ratio of measured to predicted pedestal heights of  $0.835 \pm 0.036$ , indicated by the red dashed line.

**Figure 4.9:** Pressure pedestal height predicted by EPED1.63 versus the measured (ensemble-averaged) pedestal height, color-coded by magnetic field set. The grey band indicates perfect agreement,  $\pm 20\%$  typical prediction accuracy for EPED. The EPED model systematically over-predicts the pedestal pressure, with an average match of  $0.835 \pm 0.036$  (indicated by the red line).



The discrepancy between the predicted and measured pedestal heights may be attributed (at least in part) to the use of pedestal measurements averaged across the entire ELM cycle (“ensemble-averaged”). As discussed in section 4.2, models of the pedestal structure (including EPED) most closely correspond to the pedestal structure immediately preceding the ELM crash, where the pedestal is most unstable to the ELM trigger. A subset of ELMy H-modes are prepared with ELM-synchronized data, shown in fig. 4.10 with the corresponding ensemble-averaged points for comparison. The prediction accuracy is substantially improved, with an average ratio of measured to predicted pedestal heights of  $0.934 \pm 0.066$ , well within the anticipated  $\pm 20\%$  accuracy of the EPED prediction. As expected, the modification to the measured pedestal pressure by ELM synchronization is minimal at lower pedestal pressures, but becomes substantial at higher

**Figure 4.10:** Pressure pedestal height predicted by EPED1.63 versus measured, ELM-synchronized pedestal height (red, with corresponding ensemble-average points shown in black). The grey band indicates perfect agreement,  $\pm 20\%$  typical prediction accuracy for EPED. ELM synchronization brings the measured pedestal height into better agreement with EPED predictions, with a correspondence of  $0.934 \pm 0.066$  (indicated by the red dash).



pedestal pressures ( $> 35$  kPa) as ELM losses increase proportionally with the pedestal stored energy.

The EPED model still systematically slightly over-predicts the pedestal pressure, however – this is potentially due to the strong sensitivity of the stability calculation to diamagnetic effects, which tend to stabilize higher- $n$  ballooning modes. As diamagnetic effects are substantial in the relatively collisional pedestal found in H-modes on C-Mod, a careful accounting of these effects is necessary for accurate prediction – use of a slightly weaker diamagnetic stabilization model brings the prediction into generally better agreement with C-Mod data.

#### 4.3.2 Pedestal Width

While historically a number of models for the pedestal width (see section 3.1) have been examined, the most uniformly successful has been an expected scaling of pedestal width with poloidal beta at the pedestal top ( $\beta_{p,ped}$ ), observed on several machines [9], and shown to follow from a critical-gradient limit in the edge pressure profile established by kinetic-balloonning mode (KBM) turbulence. Including magnetic shear stabilization, this takes the form  $\Delta = c\beta_{p,ped}^{1/2}$ , where  $c$  is, strictly, a weakly-varying function of a number of plasma parameters [11]. This constraint on the pedestal width and height is utilized in the EPED model, coupled with peeling-balloonning MHD stability limits to set a unique constraint on the pedestal structure at the ELM crash.

An evaluation of this scaling with ensemble-averaged data is shown in fig. 4.11, with a fitted scale factor of  $\langle c \rangle = 0.0857 \pm 0.0024$ , consistent with previously-observed scalings. The earliest versions of the EPED model used this simple constraint as the second condition on

the pedestal width and height, using an experimentally-determined fixed scale factor. The newest version of the model self-consistently calculates the scale factor from gyrokinetic considerations of the KBM turbulence; however, the results are quantitatively similar. A comparison of the experimental versus the EPED1.63-predicted pedestals in  $\Delta_\psi - \beta_{p,ped}$  space is shown in fig. 4.12.

**Figure 4.11:** Ensemble-averaged EPED width  $\Delta_\psi$  (eq. (4.2)) versus  $\beta_{p,ped}$ , color-coded by field set. The expected scaling from the KBM limit,  $\Delta_\psi = c\beta_{p,ped}^{1/2}$ , is shown with a scale factor of 0.0857, consistent with observations in previous experiments.

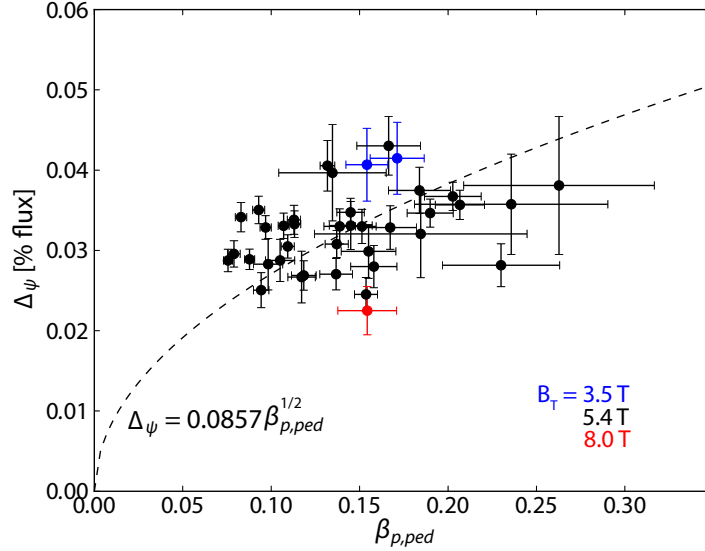
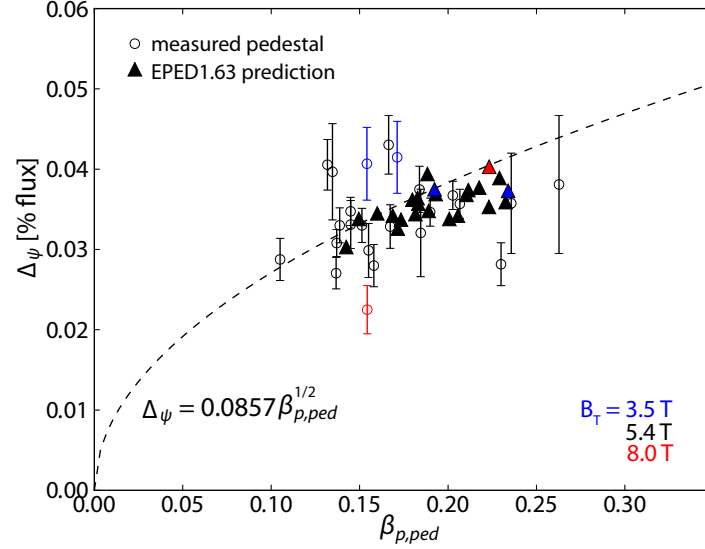
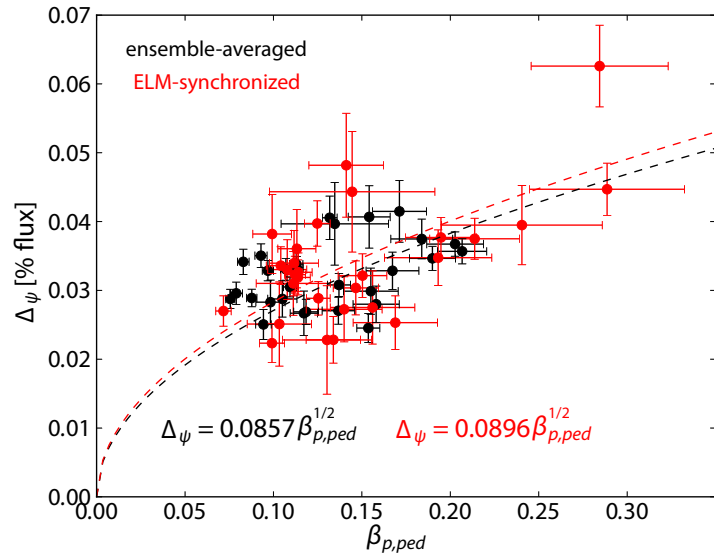


**Figure 4.12:** Comparison of EPED1.63-predicted pedestal width  $\Delta_\psi$  and height  $\beta_{p,ped}$  with the corresponding ensemble-averaged experimental points, with the KBM scaling  $\Delta_\psi = c\beta_{p,ped}^{1/2}$ . Though the EPED predictions were calculated with a self-consistent treatment of the scale factor  $c$  as a weakly-varying function of plasma parameters, the result is quantitatively similar to the simple fixed scale factor.



Application of the ELM synchronization technique does not significantly alter this result, although the pedestal pressure (i.e.,  $\beta_{p,ped}$ ) is significantly increased in the last 20% of the ELM cycle. Recent research in the inter-ELM development of the pedestal [26] has shown that the KBM saturates early in the ELM cycle, limiting the pedestal gradient; the pedestal width and height then both increase until the peeling-ballooning MHD boundary is also reached, triggering the

**Figure 4.13:** Comparison of ensemble-averaged (black) and ELM-synchronized (Red) pedestal width and height, compared to the KBM constraint. The  $\Delta_\psi = 0.0857\beta_{p,ped}^{1/2}$  scaling found in the ensemble-averaged case is shown in black, while the minor modification of  $\Delta_\psi = 0.0896\beta_{p,ped}^{1/2}$  for the ELM-synced cases is shown in red.



ELM. Consistent with this, ELM-synchronized pedestals exhibit wider, taller pedestals on average, with a similar constraint imposed by the KBM compared to the ensemble-averaged result. A comparison of the ensemble-averaged and ELM-synced pedestals in  $\Delta_\psi - \beta_{p,ped}$  space is shown in fig. 4.13, with the ELM-synced pedestals fitted to a scale factor  $\langle c \rangle = 0.0896 \pm 0.0034$ . The data may be clarified significantly by taking an error-weighted average within fixed bins in  $\beta_{p,ped}$  as well, shown in fig. 4.14, which tends to reduce the influence of strongly-outlying points on the fit. Again, the fit is quantitatively very similar – the data fit well to  $\Delta_\psi = c\beta_{p,ped}^{1/2}$  with  $\langle c \rangle = 0.0851 \pm 0.003$ . Alternately, we may use a more general power-law fit  $\Delta_\psi = c_1\beta_{p,ped}^{c_2}$ , with which we find  $\langle c_1 \rangle = 0.0824 \pm 0.015$  and  $\langle c_2 \rangle = 0.49 \pm 0.11$ , closely reproducing the  $\beta_{p,ped}^{1/2}$  model. The fitting results are quite consistent across these methods, demonstrating the robustness of the KBM model for the pedestal width and its insensitivity to the details of data preparation.

*check reasoning!*

Prediction of the pedestal width is difficult, given the robust width of the pressure pedestal (typically 3-5% of poloidal flux space, corresponding to  $\sim 5$  mm on C-Mod). The EPED model correctly recovers this robustness (within the expected  $\pm 20\%$  prediction error), as shown in fig. 4.15. As seen in fig. 4.13, ELM-synchronized pedestals are typically somewhat wider than their ensemble-averaged counterparts, commensurate with the increased  $\beta_{p,ped}$  at the maximum of the ELM cycle while the pedestal structure is limited throughout most of the ELM cycle by KBM turbulence. A comparison of the ELM-synced pedestal widths versus EPED1.63 prediction is shown in fig. 4.16.

*reword this*

**Figure 4.14:** ELM-synchronized pedestals, with data binned by  $\beta_{p,ped}$  for clarity. The data are fitted by  $\Delta_\psi = (0.0851 \pm 0.003) \beta_{p,ped}^{1/2}$  (black), or by  $\Delta_\psi = (0.0824 \pm 0.015) \beta_{p,ped}^{0.49 \pm 0.11}$  using a more general power law.

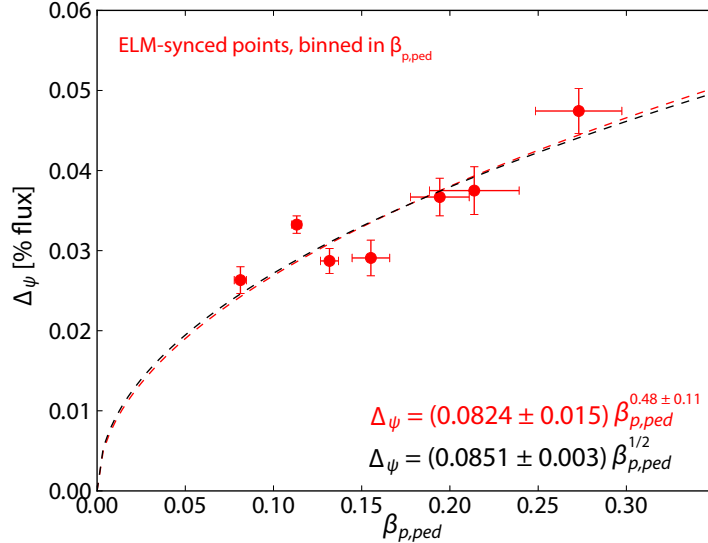
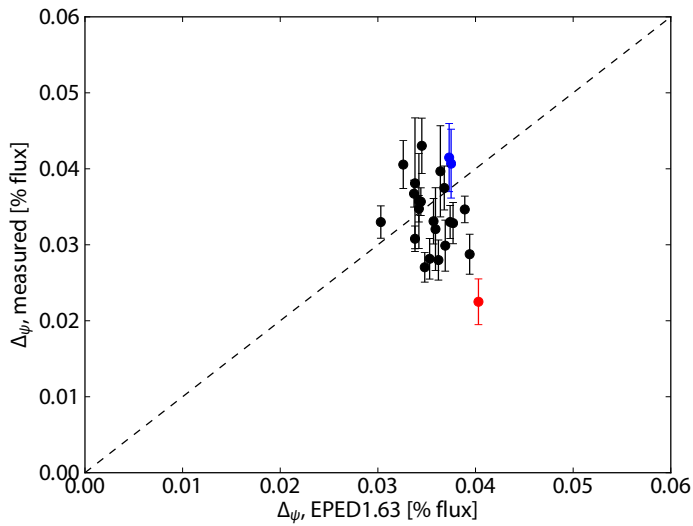


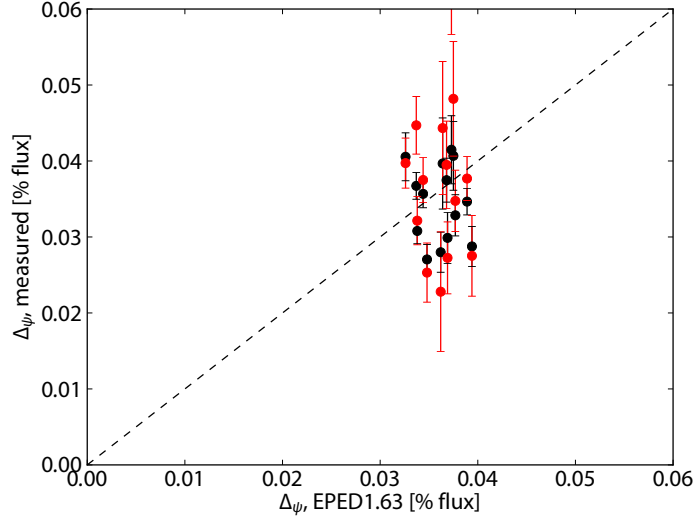
**Figure 4.15:** Measured EPED pedestal width  $\Delta_\psi = (\Delta n_e + \Delta T_e)/2$  in ensemble-averaged pedestals versus EPED1.63-predicted pedestal widths. Magnetic-field groups are indicated by color. The dashed line indicates perfect agreement with EPED prediction. Pedestals widths are robust on C-Mod, restricted to  $\sim 2 - 5\%$  of poloidal flux. The EPED model reproduces this trait within expected prediction error.



#### 4.4 ENGINEERING PARAMETER SCAN

The ELMy H-mode experiments presented here significantly expanded the parameter range available for the regime on Alcator C-Mod, including a broad scan in plasma current (400 – 1100 kA) and toroidal magnetic field (3.5, 5.4, 8.0 T), as well as sweeps of elongation ( $1.45 < \kappa < 1.55$ ) and collisionality ( $0.25 < v_{95}^* < 6$ ). This sweep entailed a factor of  $\sim 7$  sweep in pedestal pressure – notably, this expanded the range of pressure pedestals tested against the EPED model to within a factor of two of the target pedestal thermal pressure for ITER [12].

**Figure 4.16:** Measured pedestal width  $\Delta_\psi$  versus EPED1.63 predicted width. Ensemble-averaged points are shown in black, while corresponding ELM-synchronized points are shown in red. ELM-synced pedestals are typically somewhat wider, although still lie within the  $\pm 20\%$  expected error for EPED.



#### 4.4.1 $I_p$ Scan

Trends of the density, temperature, and pressure pedestal widths and heights with plasma current are shown in fig. 4.17. Previous experiments in EDA H-modes [27] demonstrated a robust linear dependence of the pedestal density on plasma current; a similar trend is found in ELMy H-mode (fig. 4.17, (b)), albeit with a significantly less robust dependence. A weak positive trend of the pedestal temperature (fig. 4.17, (d)) is also seen, but is insufficient as a unique predictor. The combined pressure pedestal ( $p = 2n_e T_e$ ) exhibits a  $p_{95} \sim I_p$  trend, with some scatter.

The density and temperature pedestal widths individually show no systematic dependence on the plasma current. The combined pressure pedestal width – although varying little over the range of 3–5% of poloidal flux – an inverse trend  $\Delta_p \sim I_p^{-1}$  is discernable. However, there is significant covariance between the plasma current and magnetic field, particularly at the low- $I_p$ /low- $B_T$  points – as some pedestal observations have asserted a broader pedestal at low field [28], this is a possible conflating factor.

*check this!*

These observations are generally consistent with historical observations of the ELMy H-mode pedestal – the combined  $p_{ped} \sim I_p$  and  $\Delta_p \sim I_p^{-1}$  trends indicate a pressure gradient limit,  $\nabla p \sim I_p^2$ , consistent with pedestals limited by ballooning MHD instability, as described in section 3.2. Moreover, the pressure pedestal width trend is consistent with the previously-observed constraint from kinetic-ballooning turbulence,  $\Delta_p \sim \beta_{p,ped}^{1/2} \sim \sqrt{p_{ped}}/I_p$ , with the scatter in  $\Delta_p \sim I_p^{-1}$  due to pressure variation. Previous experiments in H-mode have observed a trend of  $p_{ped} \sim I_p^2$  with no dependence of the pedestal width on current; however, this is consistent with the ballooning limit of  $\nabla p \sim I_p^2$ , and may be attributed to the small range over which the pedestal

*check refs*

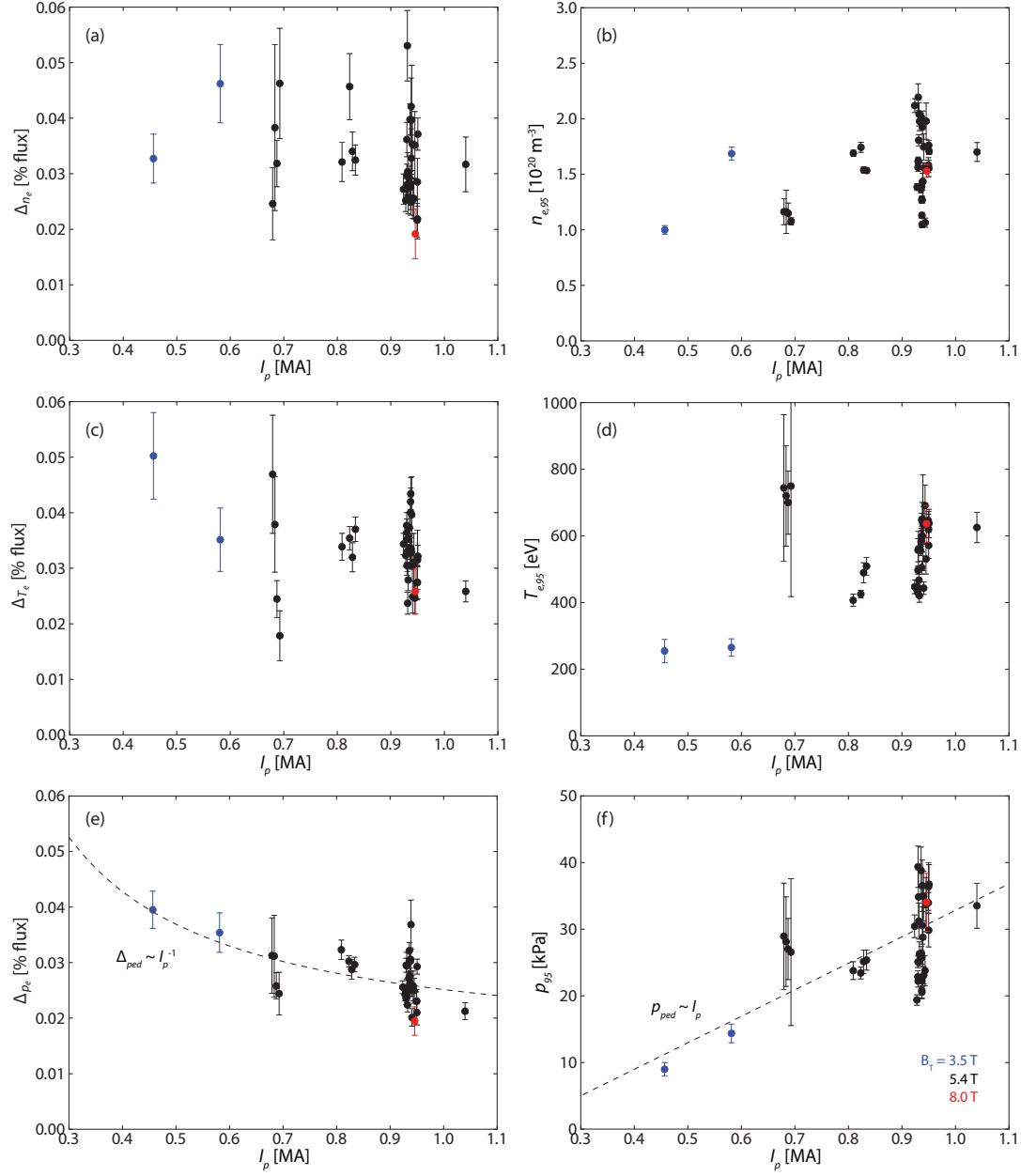
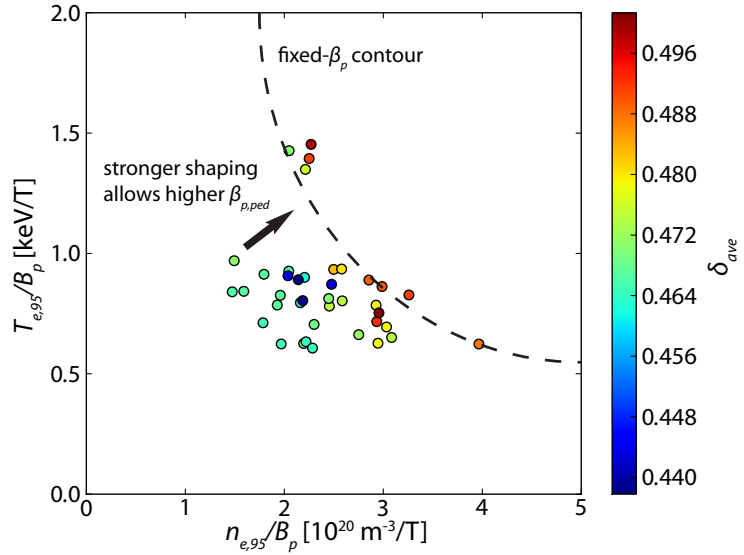


**Figure 4.17:** Plasma current scalings of the density, temperature, and pressure pedestal widths and heights. Magnetic-field sets are differentiated by color. While the density and temperature pedestals independently show little systematic dependence of their widths on plasma current, the pressure pedestal width shows a exhibits a  $\Delta_{ped} \sim I_p^{-1}$  trend. The  $n_e$  and  $T_e$  pedestal heights both positively trend with current, although with significant scatter – inverse trends between the two are consistent with the zero'th-order approximation of MHD-limited ELMy pedestals lying on a curve of fixed  $\beta_{p,ped}$  for a given shaping/field configuration. The pressure pedestal height shows a trend of  $p_{ped} \sim I_p$ , such that the pressure pedestal is consistent with the expected  $\nabla p \sim I_p^2$  scaling.

**Figure 4.18:** Pedestal density vs. temperature normalized to poloidal field (accounting for variation in plasma current) such that hyperbolae in the parameter space are curves of fixed  $\beta_{p,ped}$ . At a given shaping, ELM My H-mode pedestals are to lowest order constrained to fixed  $\beta_{p,ped}$ , with stronger shaping allowing greater attainable  $\beta_p$ .



width varies on a given machine. In the C-Mod cases as well, the pedestal width varies over a sufficiently small range that, to lowest order, the ballooning limit may be approximated as a limit on  $\beta_p$  at the pedestal top. This is shown in fig. 4.18 (see also fig. 2.3), showing the pedestal density versus temperature normalized to the poloidal field. This normalization accounts for plasma-current differences between points, as well as rendering hyperbolae in the parameter space as contours of fixed  $\beta_{p,ped}$ . At a given shaping, ELM My H-modes lie roughly on a contour of fixed  $\beta_{p,ped}$ , with stronger shaping allowing a higher attainable poloidal beta.

Pre-EPED models accounting for pressure-gradient limits assumed the pressure pedestal height would be governed simply by  $p_{ped} \sim \nabla p \times \Delta_p$ , with  $\nabla p$  limited by MHD stability and a separate constraint for the pedestal width. The ballooning limit was couched by Saibene *et al.* [29] as  $\nabla p \sim I_p^2 f_{sh}$ , where  $f_{sh}$  is a function describing the edge magnetic shear. Taking the pedestal width to be governed by poloidal gyroradius  $\rho_{i,pol} \sim \sqrt{T_e}/I_p$  (as was done by Saibene *et al.*), this predicts  $p_{ped} \sim I_p \sqrt{T_{e,ped}}$ , as shown in fig. 4.19. However, the putative scaling of the pedestal width on  $\rho_{i,pol}$  is readily conflated with the KBM-limited trend of pedestal width with  $\beta_{p,ped}^{1/2} \sim \sqrt{n_e T_e}/I_p$ . Assuming a  $\beta_{p,ped}$  limit on the pedestal width, we predict  $p_{ped} \sim I_p \sqrt{n_{e,ped} T_{e,ped}}$ , shown in fig. 4.20 to be a significantly better predictor of the pedestal height.

*better wording?*

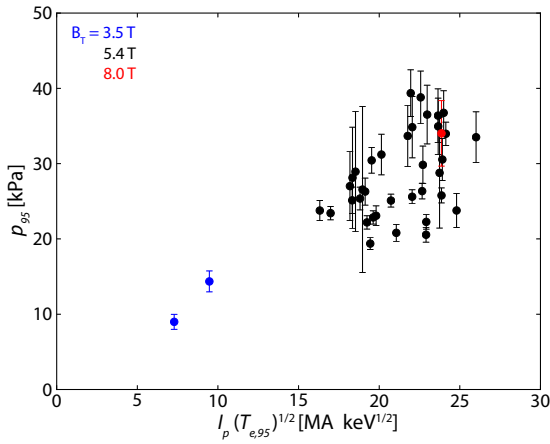


**Figure 4.19:** Pedestal pressure versus  $I_p \sqrt{T_{e,95}}$  – effectively, the  $p_{\text{ped}} \sim I_p^2 \rho_{i,\text{pol}}$  scaling predicted in [30].

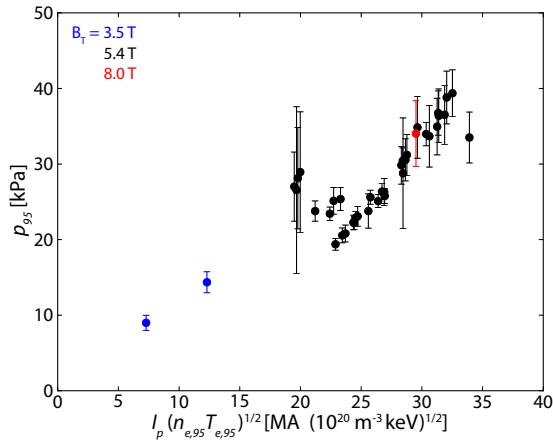
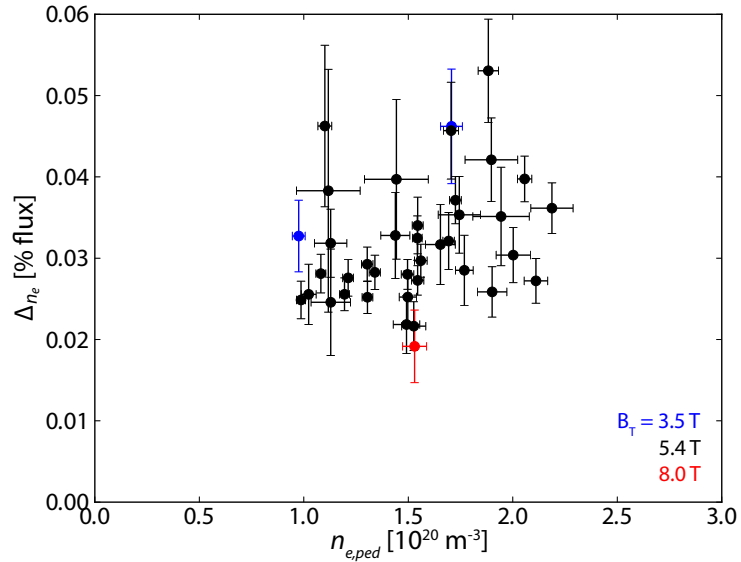


**Figure 4.20:** Pedestal pressure versus  $I_p \sqrt{n_{e,95} T_{e,95}}$  – effectively, the  $p_{\text{ped}} \sim I_p^2 \sqrt{\beta_{p,\text{ped}}}$  scaling predicted for a KBM-limited pedestal.

**Figure 4.21:** Density pedestal width versus pedestal density. Contrary to expectations from neutral-penetration models (see section 3.1.2), there is little systematic variation of the density pedestal width and height.



## 4.5 PEDESTAL WIDTH RESPONSE

### 4.5.1 Alternate Width Models

Initial models for the pedestal width (see section 3.1) led to several easily-testable predictions – first, neutral-penetration models (section 3.1.2) predict a scaling of the density pedestal  $\Delta_{n_e} \sim 1/n_{e,ped}$ , while transport-driven models predict temperature/pressure pedestal widths limited by poloidal gyroradius, or equivalently the banana orbit width (section 3.1.3). The density pedestal width is shown against pedestal density in fig. 4.21 – while there is high scatter in the data, with both the pedestal density and measured width  $\Delta_{n_e}$  spanning more than a factor of two in variation, the densest region in the dataset shows a weak positive trend between density pedestal width

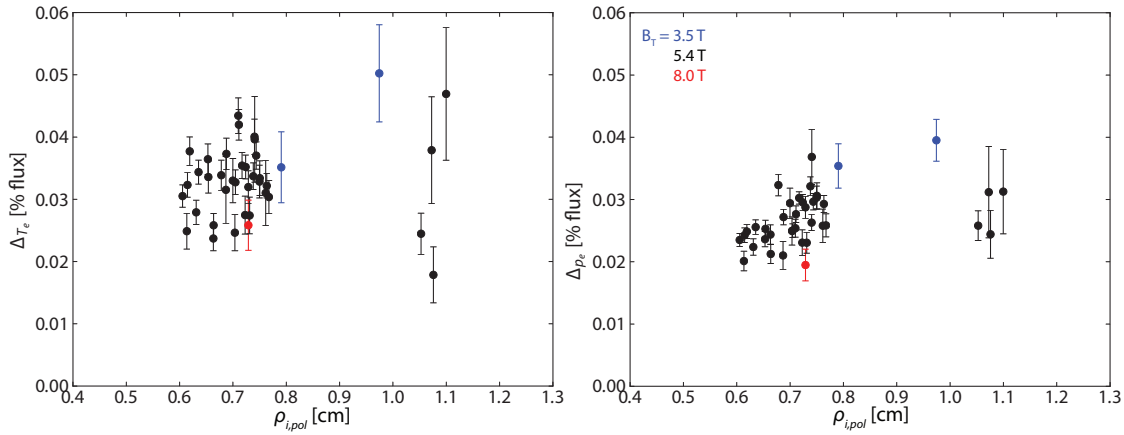


**Figure 4.22:** Temperature and pressure pedestal widths versus poloidal gyroradius. The temperature pedestal width shows no systematic variation with  $\rho_{i,\text{pol}}$ . A weak trend is possible in the pressure pedestal width, comparable to the the trend of  $\Delta p \sim \beta_{p,\text{ped}}^{1/2}$  (due to the strong covariance between  $\rho_{i,\text{pol}}$  and  $\beta_{p,\text{ped}}$ ). However, this trend is overruled in favor of a poloidal beta scaling by other observations.

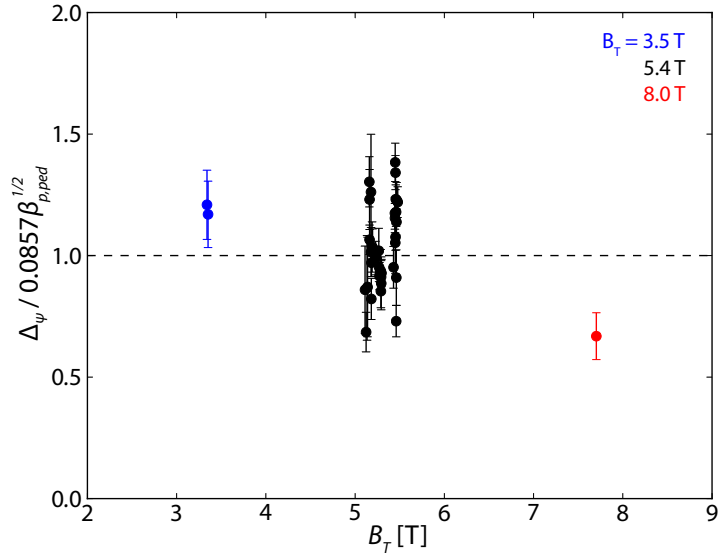
and height. This is directly contrary to the predictions from simple neutral-penetration models; however, it is consistent with previous observations in EDA H-mode [28]. The measured temperature and pressure widths  $\Delta T_e$  and  $\Delta p_e$  are shown against  $\rho_{i,\text{pol}}$  (the ion gyro-radius evaluated with the poloidal field) in fig. 4.22. In the case of the temperature pedestal width, no systematic variation with  $\rho_{i,\text{pol}}$  is seen. A possible weak trend for the pressure pedestal width is seen, with comparable spread to that seen in the pressure pedestal width versus  $\beta_{p,\text{ped}}$ . However, as there is significant covariance between  $\rho_{i,\text{pol}} \sim \sqrt{T_e}/I_p$  and  $\beta_{p,\text{ped}} \sim \sqrt{n_e T_e}/I_p$ , and the width scaling with  $\beta_{p,\text{ped}}$  is seen to be a superior predictor (see fig. 4.20) this model should be discarded in favor of the  $\Delta \sim \beta_{p,\text{ped}}^{1/2}$  scaling from KBM physics. This is consistent with results from experiments designed to distinguish between  $\rho_{i,\text{pol}}$  and  $\beta_{p,\text{ped}}$  dependencies via isotope variation to exploit the mass dependence in  $\rho_{i,\text{pol}}$  [31] or pumping experiments to independently vary pedestal density and temperature at fixed pressure [32, 33].

#### 4.5.2 Normalized Pedestal Width

As detailed in section 4.3.2, the scale factor in the dominant width scaling in ELMY H-mode,  $\Delta \sim \beta_{p,\text{ped}}^{1/2}$ , is most properly a weakly varying function of plasma shaping, collisionality, and other dimensionless parameters:  $\Delta_\psi = G(\nu^*, \varepsilon, \dots) \beta_{p,\text{ped}}^{1/2}$  [12]. These secondary dependencies in  $G$  may be examined by normalizing the pedestal width (here we use the EPED width,  $\Delta_\psi$ , from eq. (4.2)) to the fitted scaling  $\Delta_\psi = 0.0857 \beta_{p,\text{ped}}^{1/2}$  (see fig. 4.11).

ref to ch. 3 section?

**Figure 4.23:** Scalings of the pedestal width  $\Delta_\psi$ , normalized to the dominant scaling  $\Delta_\psi = 0.0857 \beta_{p,ped}^{1/2}$  with the applied toroidal field  $B_T$ . Although the high scatter at standard  $B_T$  and the sparsity of data at low and high field makes a conclusive scaling difficult, there is some indication of an inverse relation of pedestal width with toroidal field.



Normalized pedestal widths are shown against the range in toroidal fields in fig. 4.23. The high scatter in the normalized pedestal widths at standard field (5.4 T), along with the difficulty in attaining usable ELMy H-modes at low and high field, renders it difficult to conclusively establish a secondary scaling of the pedestal width with toroidal field. While the comparatively broader pedestal at low field is consistent with some previous observations, the covariance between  $B_T$  and  $I_p$  (and therefore  $\beta_p$ ) in the low-field phase of the experiment complicates this observation.

cite Hughes...  
*DIII-D observations*  
too?

Similarly, normalized pedestal widths are shown against the plasma shaping parameters – upper and lower triangularity  $\delta_u$ ,  $\delta_l$ , average triangularity  $\delta_{ave} = (\delta_l + \delta_u)/2$ , and elongation  $\kappa$  – in fig. 4.24. No clear secondary dependence of the normalized pedestal width (that is, in the scale function  $G(v^*, \varepsilon, \dots)$ ) is seen in shaping:  $\delta_l$ ,  $\delta_{ave}$ , and  $\kappa$  exhibit no trend, while  $\delta_u$  is unclear with the broadest widths (compared to the  $\sim 0.0857\beta_{p,ped}^{1/2}$  fit) at both the low and high extremes of the range in  $\delta_u$ . Rather, the shaping dependence manifests as increased poloidal beta, and secondarily pedestal width, at stronger shaping – increased shaping is known to have a stabilizing effect on ballooning MHD modes, increasing the normalized pressure gradient  $\alpha_{MHD}$  at which the instability is triggered. However, as the shaping range available for ELMy H-modes on C-Mod is restricted, weak dependences on shaping are still possible.

*cite, elaborate?*

Pedestal collisionality  $\nu_{95}^*$  is anticipated as a controlling term in the scale function  $G$ , due both to its role in controlling ionization rate and neutral penetration, and its influence on bootstrap current density and the accompanying MHD effects in the pedestal. However, across a broad range on collisionality,  $0.25 < \nu_{95}^* < 6$ , no systematic variation in the normalized pedestal width is seen (see fig. 4.25). The highest collisionality points were obtained in cold, low-field dis-

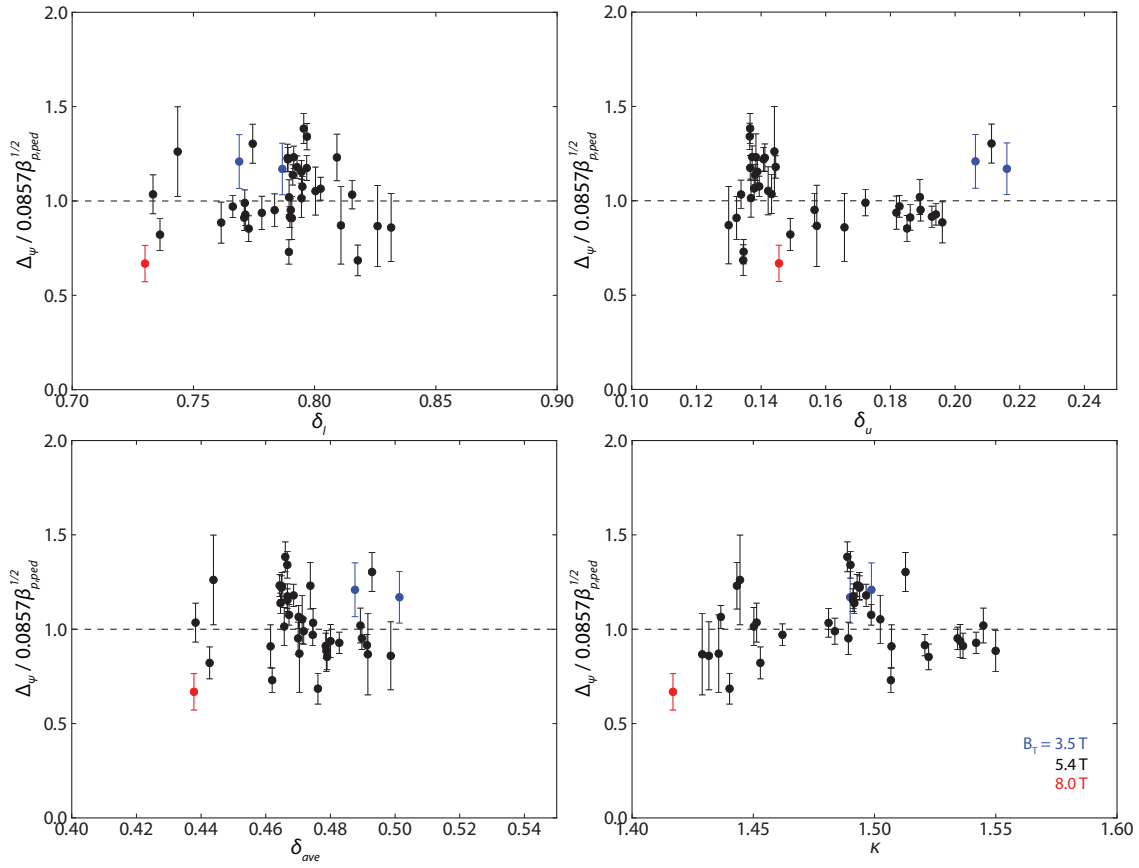


**Figure 4.24:** Scalings of the pedestal width  $\Delta_\psi$  normalized to the dominant scaling  $\Delta_\psi = 0.0857\beta_{p,ped}^{1/2}$ , with plasma shaping: upper, lower, and average triangularity ( $\delta_l$ ,  $\delta_u$ ,  $\delta_{ave} = (\delta_u + \delta_l)/2$ ), and elongation  $\kappa$ . No strong trend with shaping parameters is seen – rather, the influence of plasma shaping is exhibited by increased  $\beta_{p,ped}$  and pedestal width due to increased stability to peeling-balloon MHD.

charges, possibly conflating the elevated pedestal width (relative to the  $\sim 0.0857\beta_{p,ped}^{1/2}$  fit) with possible broadening at reduced  $B_T$ .

While a primary dependence of the pedestal width on the gyroradius is ruled out (see the discussion in section 4.5.1 and fig. 4.20), a secondary gyroradius dependence in addition to the  $\beta_p$  scaling is still possible – for example,  $\Delta_{ped} \sim \rho_{i,pol}^{0.2} \beta_{p,ped}^{0.5}$  found by Urano *et al.* [31]. However, when the scale function  $G$  is examined via trends of the normalized pedestal width versus normalized gyroradius  $\rho_{95}^*$ , shown in fig. 4.26, no systematic dependence is seen. Notably, the strong outlier for  $\rho^*$  – the high- $B_T$  case, shown to have a narrow pedestal compared to the expected scaling – is nevertheless within the range of normalized width for the bulk of the dataset. As such, no distinct dependence of the normalized width (equivalently,  $G(\nu^*, \varepsilon, \dots)$ ) can be discerned from the data.

**Figure 4.25:** Scaling of the normalized pedestal width  $\Delta_\psi / 0.0857 \beta_{p,ped}^{1/2}$  versus pedestal collisionality  $v_{95}^*$ . Low, standard, and high-field sets are indicated in blue, black, and red respectively. No systematic variation is observed.

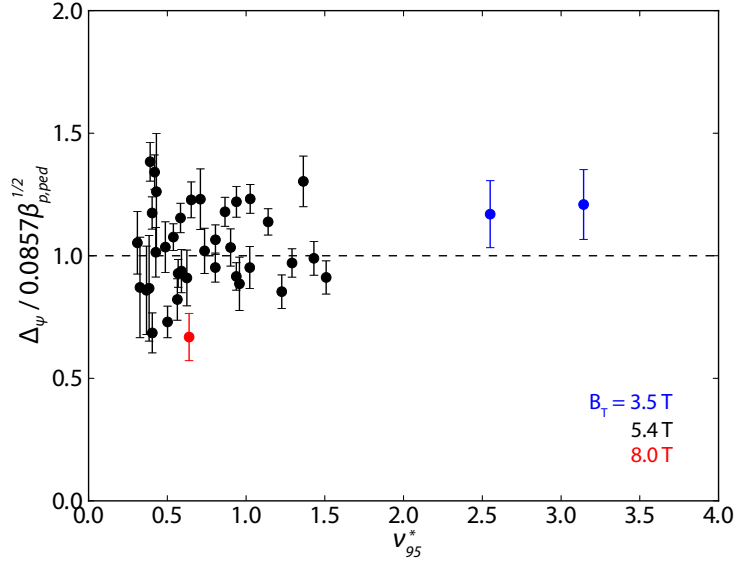
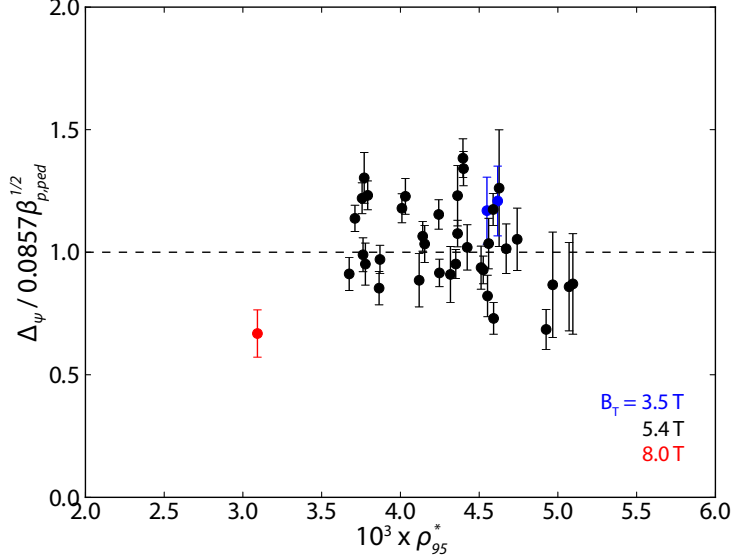


**Figure 4.26:** Scaling of the normalized pedestal width  $\Delta_\psi / 0.0857 \beta_{p,ped}^{1/2}$  with normalized pedestal gyroradius  $\rho_{95}^*$ . Low, standard, and high-field sets are indicated in blue, black, and red respectively. No systematic variation is seen.



#### 4.6 CONCLUSIONS

ELMy H-mode experiments on C-Mod reach the highest magnetic field and pedestal thermal pressure of any tokamak, reaching within a factor of  $\sim 2$  of the target pressure for ITER. As part of a DOE Joint Research Target [9], these experiments tested the EPED model series [11] for ELMy H-mode pedestal width and height, greatly expanding the parameter space in which the model has been implemented [18]. The newest version of EPED, EPED1.63 (a minor modification to EPED1.6 to account for strong diamagnetic effects on C-Mod) accurately predicts the pressure pedestal height, particularly when pedestal data is masked to time frames immediately preceding ELM crashes – a practice that, despite diagnostic difficulties on

C-Mod, produces data most closely corresponding to the pedestal structure at the point of ELM instability. Although systematic prediction of the pedestal width on C-Mod is difficult due to the narrow range over which it varies, the EPED prediction for  $\Delta_\psi$  matches experimental results to within the expected  $\sim 20\%$  error.

The pedestal width is well-described by the prediction used by EPED1.6 based on kinetic-balloonning turbulence,  $\Delta_\psi = G(\nu^*, \varepsilon, \dots) \beta_{p,ped}^{1/2}$ , where  $G(\nu^*, \varepsilon, \dots)$  is a weakly varying function,  $G \approx .0857$  – matching the fitted result from multiple machines [9]. Secondary scalings of the pedestal width, discerned by normalizing the pedestal width to the dominant  $\beta_{p,ped}$  dependence, with magnetic field,  $\nu^*$ ,  $\rho^*$ , and shaping parameters are minimal over the available range in the data set. Conversely, the pedestal width is not well-described by alternate models not based on the KBM-driven  $\beta_{p,ped}$  dependence: the density pedestal width does not exhibit a  $\Delta_{n_e} \sim n_{e,ped}$  trend expected from neutral-penetration models, while the temperature and pressure pedestals do not scale clearly with  $\rho_{i,pol}$ . The temperature pedestal width shows no trend with poloidal gyroradius, while the pressure pedestal does not show a trend independent of the  $\beta_{p,ped}$  scaling ( $\rho_{i,pol}$  and  $\beta_{p,ped}$  are difficult to discern from one another without careful operational control).

Examined over a broad range in plasma current, the pressure pedestal height exhibits a trend  $p_{ped} \sim I_p$ , while the pressure pedestal width trends as  $\Delta_{p_e} \sim I_p^{-1}$ . This is consistent with the expected trend of  $\nabla p_{ped} \sim I_p^2$  from balloonning MHD stability, although previous observations typically find  $p_{ped} \sim I_p^2$  with less systematic variation in the pedestal width. More carefully, the pedestal height is well-predicted by  $p_{ped} \sim \nabla p \times \Delta_p$  – taking  $\nabla p \sim I_p^2$  from MHD stability and the pedestal width  $\Delta_p \sim \beta_{p,ped}^{1/2} \sim \sqrt{n_{e,ped} T_{e,ped}} / I_p$  gives  $p_{ped} \sim I_p \sqrt{n_{e,ped} T_{e,ped}}$  (see fig. 4.20), which matches the observed pressure pedestal height quite well.

*cite?*

*better ending to the conclusion?*



## BIBLIOGRAPHY

---

- [1] F. Wagner, G. Becker, K. Behringer, D. Campbell, A. Eberhagen et al. **Regime of improved confinement and high beta in neutral-beam-heated divertor discharges of the ASDEX tokamak.** *Physical Review Letters*, 49(19):1408–1412, Nov 1982.
- [2] M Keilhacker, G Becker, K Bernhardi, A Eberhagen, M ElShaer et al. **Confinement studies in L and H-type ASDEX discharges.** *Plasma Physics and Controlled Fusion*, 26(1A):49, 1984.
- [3] ITER Physics Expert Group on Confinement, Transport and ITER Physics Expert Group on Confinement Modelling and Database and ITER Physics Basis Editors. **Chapter 2: Plasma confinement and transport.** *Nuclear Fusion*, 39(12):2175, 1999.
- [4] M. Shimada, D.J. Campbell, V. Mukhovatov, M. Fujiwara, N. Kirneva et al. **Chapter 1: Overview and summary.** *Nuclear Fusion*, 47(6):S1, 2007.
- [5] A Loarte, G Saibene, R Sartori, D Campbell, M Becoulet et al. **Characteristics of type I ELM energy and particle losses in existing devices and their extrapolation to ITER.** *Plasma Physics and Controlled Fusion*, 45(9):1549, 2003.
- [6] G Federici, A Loarte and G Strohmayer. **Assessment of erosion of the ITER divertor targets during type I ELMs.** *Plasma Physics and Controlled Fusion*, 45(9):1523, 2003.
- [7] J.E. Kinsey, G.M. Staebler, J. Candy, R.E. Waltz and R.V. Budny. **ITER predictions using the GYRO verified and experimentally validated trapped gyro-Landau fluid transport model.** *Nuclear Fusion*, 51(8):083001, 2011.
- [8] E.J. Doyle, W.A. Houlberg, Y. Kamada, V. Mukhovatov, T.H. Osborne et al. **Chapter 2: Plasma confinement and transport.** *Nuclear Fusion*, 47(6):S18, 2007.
- [9] R.J. Groebner, C.S. Chang, J.W. Hughes, R. Maingi, P.B. Snyder et al. **Improved understanding of physics processes in pedestal structure, leading to improved predictive capability for ITER.** *Nuclear Fusion*, 53(9):093024, 2013.
- [10] R. Groebner, C. Chang, P. Diamond, J. Hughes, R. Maingi et al. **Fusion energy science joint facilities and theory research target final report.** Technical report, Department of Energy Office of Science, 2011.

- [11] P. B. Snyder, R. J. Groebner, A. W. Leonard, T. H. Osborne and H. R. Wilson. **Development and validation of a predictive model for the pedestal height.** *Physics of Plasmas*, 16(5):056118, 2009.
- [12] P.B. Snyder, R.J. Groebner, J.W. Hughes, T.H. Osborne, M. Beurskens et al. **A first-principles predictive model of the pedestal height and width: development, testing and ITER optimization with the EPED model.** *Nuclear Fusion*, 51(10):103016, 2011.
- [13] P.B. Snyder, N. Aiba, M. Beurskens, R.J. Groebner, L.D. Horton et al. **Pedestal stability comparison and ITER pedestal prediction.** *Nuclear Fusion*, 49(8):085035, 2009.
- [14] P.B. Snyder, H.R. Wilson, J.R. Ferron, L.L. Lao, A.W. Leonard et al. **ELMs and constraints on the H-mode pedestal: peeling–ballooning stability calculation and comparison with experiment.** *Nuclear Fusion*, 44(2):320, 2004.
- [15] H. R. Wilson, P. B. Snyder, G. T. A. Huysmans and R. L. Miller. **Numerical studies of edge localized instabilities in tokamaks.** *Physics of Plasmas*, 9(4):1277–1286, 2002.
- [16] H R Wilson, S C Cowley, A Kirk and P B Snyder. **Magneto-hydrodynamic stability of the H-mode transport barrier as a model for edge localized modes: an overview.** *Plasma Physics and Controlled Fusion*, 48(5A):A71, 2006.
- [17] P. B. Snyder and G. W. Hammett. **Electromagnetic effects on plasma microturbulence and transport.** *Physics of Plasmas*, 8(3):744–749, 2001.
- [18] J.R. Walk, P.B. Snyder, J.W. Hughes, J.L. Terry, A.E. Hubbard et al. **Characterization of the pedestal in Alcator C-Mod ELMing H-modes and comparison with the EPED model.** *Nuclear Fusion*, 52(6):063011, 2012.
- [19] J.W. Hughes, P.B. Snyder, J.R. Walk, E.M. Davis, A. Diallo et al. **Pedestal structure and stability in H-mode and I-mode: a comparative study on Alcator C-Mod.** *Nuclear Fusion*, 53(4):043016, 2013.
- [20] M. Greenwald, N. Basse, P. Bonoli, R. Bravenec, E. Edlund et al. **Confinement and transport research in Alcator C-Mod.** *Fusion Science and Technology*, 51(3):266–287, 2007.
- [21] J.W. Hughes, A. Loarte, M.L. Reinke, J.L. Terry, D. Brunner et al. **Power requirements for superior H-mode confinement on Alcator C-Mod: experiments in support of ITER.** *Nuclear Fusion*, 51(8):083007, 2011.

- [22] J.L. Terry, I. Cziegler, A.E. Hubbard, J.A. Snipes, J.W. Hughes et al. **The dynamics and structure of edge-localized-modes in Alcator C-Mod.** *Journal of Nuclear Materials*, 363–365(0):994 – 999, 2007.
- [23] R.J. Groebner, D.R. Baker, K.H. Burrell, T.N. Carlstrom, J.R. Ferron et al. **Progress in quantifying the edge physics of the H-mode regime in DIII-D.** *Nuclear Fusion*, 41(12):1789, 2001.
- [24] R. M. McDermott, B. Lipschultz, J. W. Hughes, P. J. Catto, A. E. Hubbard et al. **Edge radial electric field structure and its connections to H-mode confinement in Alcator C-Mod plasmas.** *Physics of Plasmas*, 16(5):056103, 2009.
- [25] H Urano, W Suttrop, L D Horton, A Herrmann, J C Fuchs et al. **Energy and particle losses during type-I ELMs in H-mode in ASDEX Upgrade.** *Plasma Physics and Controlled Fusion*, 45(9):1571, 2003.
- [26] A. Diallo, W. Hughes, J. M. Greenwald, B. LaBombard, E. Davis et al. **Observation of edge instability limiting the pedestal growth in tokamak plasmas.** *Physical Review Letters*, 112:115001, Mar 2014.
- [27] J.W. Hughes, B. LaBombard, J. Terry, A. Hubbard and B. Lipschultz. **Edge profile stiffness and insensitivity of the density pedestal to neutral fuelling in Alcator C-Mod edge transport barriers.** *Nuclear Fusion*, 47(8):1057, 2007.
- [28] J. W. Hughes, D. A. Mossessian, A. E. Hubbard, B. LaBombard and E. S. Marmar. **Observations and empirical scalings of the high-confinement mode pedestal on Alcator C-Mod.** *Physics of Plasmas*, 9(7):3019–3030, 2002.
- [29] G. Saibene, L.D. Horton, R. Sartori, B. Balet, S. Clement et al. **The influence of isotope mass, edge magnetic shear and input power on high density ELMs in JET.** *Nuclear Fusion*, 39(9):1133, 1999.
- [30] M. N. A. Beurskens, T. H. Osborne, P. A. Schneider, E. Wolfrum, L. Frassinetti et al. **H-mode pedestal scaling in DIII-D, ASDEX Upgrade, and JET.** *Physics of Plasmas*, 18(5):056120, 2011.
- [31] H. Urano, T. Takizuka, Y. Kamada, N. Oyama, H. Takenaga et al. **Dimensionless parameter dependence of H-mode pedestal width using hydrogen and deuterium plasmas in JT-60U.** *Nuclear Fusion*, 48(4):045008, 2008.
- [32] T H Osborne, R J Groebner, L L Lao, A W Leonard, R Maingi et al. **H-mode pedestal characteristics, ELMs, and energy con-**

- finement in ITER shape discharges on DIII-D. *Plasma Physics and Controlled Fusion*, 40(5):845, 1998.
- [33] C.F. Maggi. Progress in understanding the physics of the H-mode pedestal and ELM dynamics. *Nuclear Fusion*, 50(6):066001, 2010.

The I-mode [1, 2], introduced in section 2.4, is a novel high-performance regime pioneered on Alcator C-Mod. I-mode is unique in that it appears to decouple energy and particle transport, forming a steep temperature pedestal with H-mode levels of energy confinement without the accompanying density pedestal or suppression of particle transport found in conventional H-modes. I-mode exhibits several highly attractive properties for a putative reactor regime:

1. Due to the lack of particle transport suppression (as is found in H-modes), the I-mode retains L-mode-like impurity confinement times, avoiding the accumulation of deleterious impurities in the plasma, including those from high-Z metal plasma-facing components necessary for reactor operation [3]. This ensures stationary operation without the need for ELMs or continuous fluctuations in the edge to provide the necessary relaxation of the particle confinement.
2. I-mode appears to be naturally stable against large ELMs, avoiding excessive pulsed heat loading to plasma-facing components without externally-applied engineering controls (described in section 2.2.3).
3. Energy confinement in I-mode appears to exhibit little to know degradation with input heating power, in contrast to that found in ELMy H-mode ( $\tau_E \sim P^{-0.7}$  from the ITER98y2 analysis [4]), scaling quite favorably to reactor-scale devices.

A firm understanding of the pedestal is essential for the extrapolation of any high-performance regime to ITER- and reactor-scale devices. The pedestal height sets a strong constraint on core temperature and pressure – and therefore overall fusion performance – both by acting as a boundary condition for the plasma profiles, and by supporting steeper core temperature gradients due to profile stiffness [5, 6]. Moreover, the pedestal structure, particularly the steep gradients in density, temperature, and/or pressure, determines stability of the plasma against large, deleterious ELMs (see section 3.2). In this chapter, we review empirical observations of the pedestal in I-mode from a recent series of dedicated experiments, with a focus on high-resolution pedestal profile measurements across a range of plasma parameters. Through this, we examine trends in I-mode pedestal behavior, and their impact on global behavior and performance in I-mode, and possible extrapolations to larger devices.

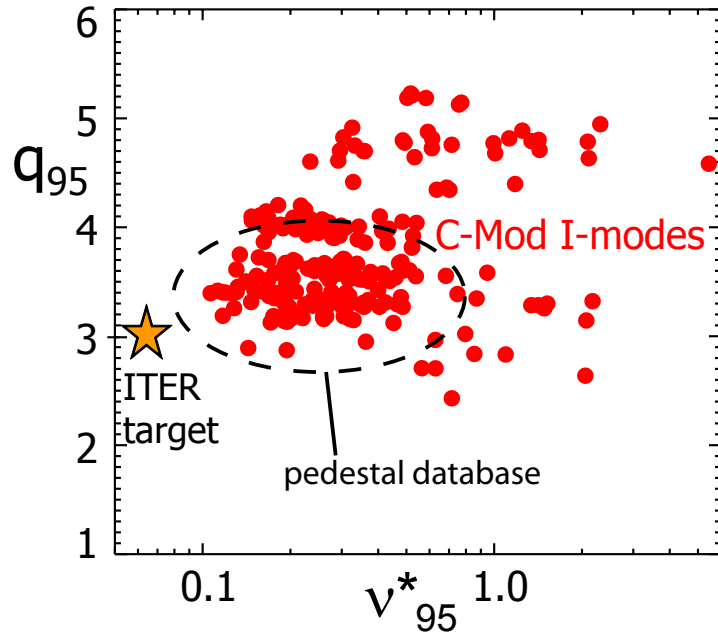
• *be more specific...  
maybe?*

## 5.1 ACCESS AND EXPERIMENTAL SETUP

All data presented here was taken on the Alcator C-Mod tokamak, described in section 1.3. As described in section 2.4.1, I-mode access hinges primarily on operation with the ion  $\nabla B$  drift (eq. (1.20)) directed away from the primary X-point in the plasma (the “unfavorable  $\nabla B$  drift” configuration). Within this requirement, though, I-mode access is fairly robust, with steady I-modes sustained in a variety of shapes – both USN with standard field, and LSN shapes with reversed field to achieve the desired  $\nabla B$  drift direction (in the latter case, the plasma current is reversed as well to preserve field helicity) – and edge-current profiles, and at low-to-moderate collisionality.

*ref to mustar  
definition*

**Figure 5.1:** Range in edge collisionality  $v_{95}^*$  and  $q_{95}$  over which I-modes have been accessed. Notably, I-mode operation is naturally favored near ITER targets for these parameters. The subset of this data prepared with high-resolution pedestal profiles, herein termed the “pedestal database”, is also highlighted.



## 5.2 PEDESTAL RESPONSES

### 5.2.1 Pedestal Temperature

### 5.2.2 Pedestal Response to Fueling

### 5.2.3 Pressure Pedestal Scalings and Performance

## 5.3 PEDESTAL WIDTHS

**Figure 5.2:** Density and temperature pedestals at matched current, field, and shaping, with varying fueling and heating power levels. The three discharges are fueled to  $\bar{n}_e$  of 1.0 (black),  $1.3 \times 10^{20} \text{ m}^{-3}$  (blue), and  $1.7 \times 10^{20} \text{ m}^{-3}$  (red) respectively, with heating powers of 2.75, 3.65, and 4.10 MW to maintain matched  $P_{\text{net}}/\bar{n}_e \sim 2.4 - 2.7$ . The constant power-per-particle maintains matched temperature pedestals across the fueling range, indicative of the independent control of pedestal  $n_e$  and  $T_e$  available in I-mode.

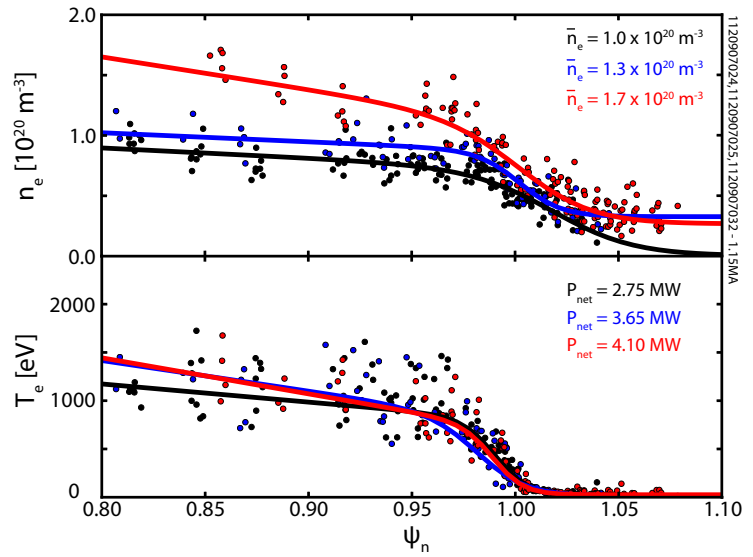
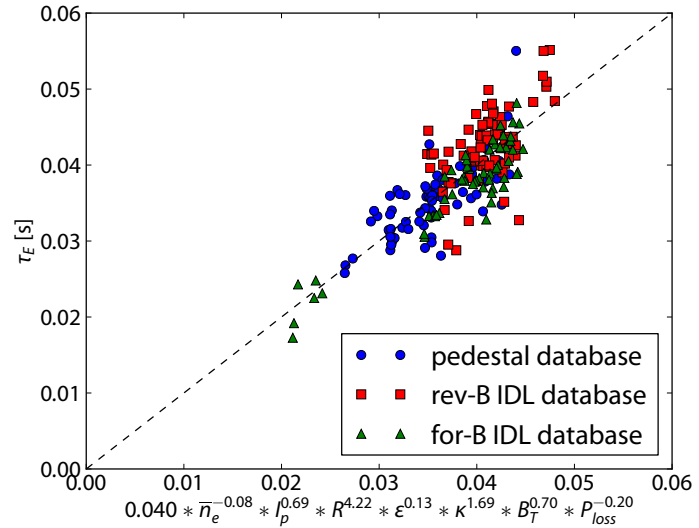


**Figure 5.3:** Power-law fit for I-mode energy confinement time  $\tau_E$ , fitted using the full ITER98y2 parameter set (fit #1 in table 5.1). Both the high-resolution pedestal database and older reversed-field LSN and forward-field USN I-mode databases are used. While the fit is generally good, lack of variation in certain parameters – particularly the size parameters  $R$  and  $\varepsilon$  (as expected for a single-machine scaling), and elongation  $\kappa$  mean that the true variation with these parameters is not accurately captured. However, the expected weak degradation of  $\tau_E$  with heating power is captured.



## 5.4 GLOBAL BEHAVIOR, PERFORMANCE, & CONFINEMENT

## 5.5 FLUCTUATION CHARACTERIZATION

★

**Table 5.1:** Parameters for power-law scalings of the I-mode energy confinement time  $\tau_E$ , along with  $R^2$  coefficients of determination for the fit. Blank entries indicate parameters that were omitted from that fit. Note that fit #5 utilized a fixed  $R^2\sqrt{\varepsilon}$  size dependence rather than taking the size to be a free fitting parameter. Parameters are in the given units:  $I_p$  in MA,  $B_T$  in T,  $\bar{n}_e$  in  $10^{20} \text{ m}^{-3}$ ,  $R$  in m, and  $P_{loss}$  in MW. Elongation  $\kappa$  and aspect ratio  $\varepsilon$  are dimensionless.

	#1	#2	#3	#4	#5
C	$0.040 \pm 0.066$	$0.007 \pm 0.002$	$0.014 \pm 0.002$	$0.014 \pm 0.002$	$0.056 \pm 0.008$
$I_p$	$0.686 \pm 0.074$	$0.696 \pm 0.073$	$0.685 \pm 0.076$	$0.692 \pm 0.073$	$0.676 \pm 0.077$
$B_T$	$0.698 \pm 0.075$	$0.697 \pm 0.071$	$0.768 \pm 0.072$	$0.773 \pm 0.071$	$0.767 \pm 0.072$
$\bar{n}_e$	$-0.077 \pm 0.055$	$-0.050 \pm 0.048$	$0.017 \pm 0.048$		$0.006 \pm 0.048$
R	$4.219 \pm 4.623$				$2^*$
$\varepsilon$	$0.127 \pm 1.144$				$0.5^*$
$\kappa$	$1.686 \pm 0.398$	$1.501 \pm 0.350$			
$P_{loss}$	$-0.197 \pm 0.048$	$-0.220 \pm 0.043$	$-0.286 \pm 0.042$	$-0.281 \pm 0.039$	$-0.275 \pm 0.042$
$R^2$	0.713	0.711	0.685	0.684	0.683

**Figure 5.4:** Power-law fit for I-mode energy confinement time  $\tau_E$ , fitted with the size parameters  $R$  and  $\varepsilon$ , and elongation  $\kappa$  excluded due to the lack of variation in these variables in the available data (fit #3 in table 5.1). Both the high-resolution pedestal database and older reversed-field LSN and forward-field USN I-mode databases are used.

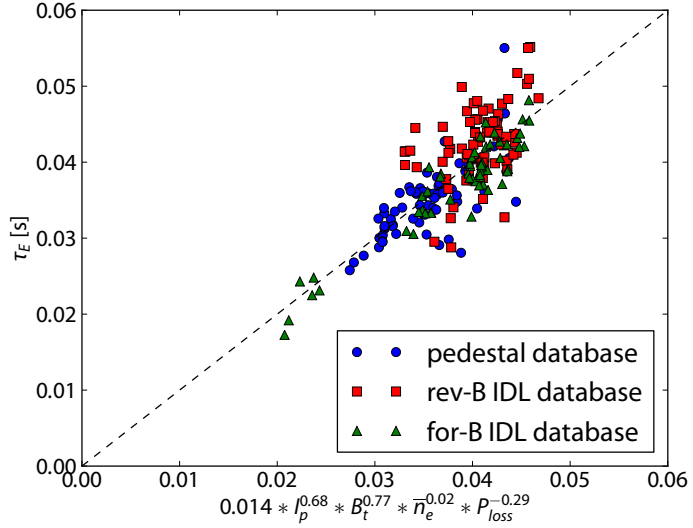


**Figure 5.5:** Power-law fit to I-mode energy confinement time  $\tau_E$ , with the ansatz of an  $R^2\sqrt{\epsilon}$  size scaling fixed (fit #5 in table 5.1). Both the high-resolution pedestal database and older reversed-field LSN and forward-field USN I-mode databases are used. Note the expected weak degradation of  $\tau_E$  with heating power.

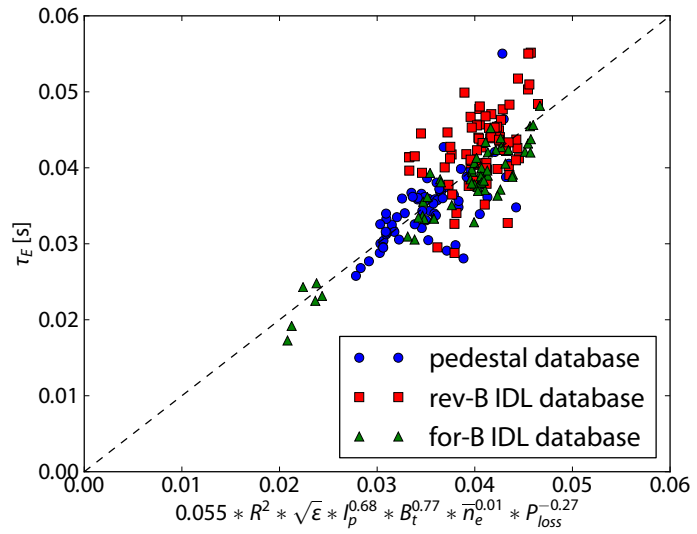
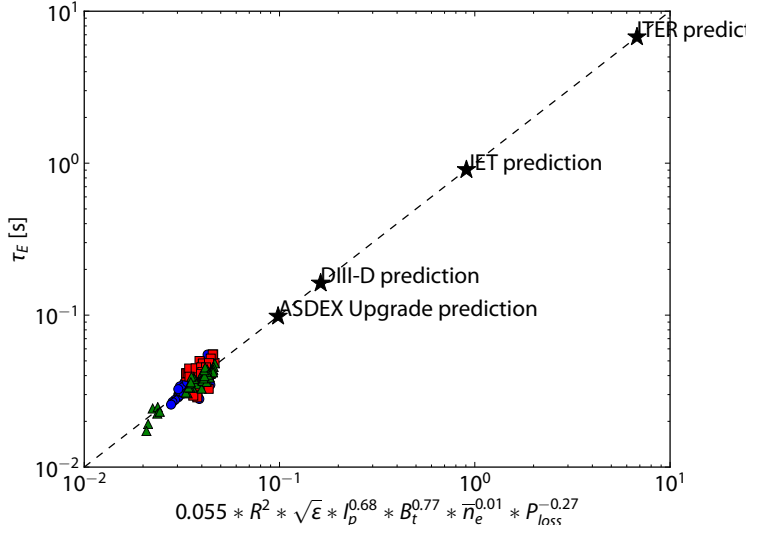


**Figure 5.6:** Modeled energy confinement time  $\tau_E$  with the fixed  $R^2\sqrt{\epsilon}$  size scaling (fit #5 in table 5.1, extrapolated to DIII-D, ASDEX Upgrade, JET, and ITER. Modeled energy confinement times are competitive with H-modes, both the measured  $\tau_E$  for existing machines and the expected ITER98y2 prediction for ITER H-modes.





## BIBLIOGRAPHY

---

- [1] D.G. Whyte, A.E. Hubbard, J.W. Hughes, B. Lipschultz, J.E. Rice et al. **I-mode: an H-mode energy confinement regime with L-mode particle transport in Alcator C-Mod.** *Nuclear Fusion*, 50(10):105005, 2010.
- [2] A. E. Hubbard, D. G. Whyte, R. M. Churchill, I. Cziegler, A. Dominguez et al. **Edge energy transport barrier and turbulence in the I-mode regime on Alcator C-Mod.** *Physics of Plasmas*, 18(5):056115, 2011.
- [3] A. Loarte, B. Lipschultz, A.S. Kukushkin, G.F. Matthews, P.C. Stangeby et al. **Chapter 4: Power and particle control.** *Nuclear Fusion*, 47(6):S203, 2007.
- [4] ITER Physics Expert Group on Confinement, Transport and ITER Physics Expert Group on Confinement Modelling and Database and ITER Physics Basis Editors. **Chapter 2: Plasma confinement and transport.** *Nuclear Fusion*, 39(12):2175, 1999.
- [5] J.E. Kinsey, G.M. Staebler, J. Candy, R.E. Waltz and R.V. Budny. **ITER predictions using the GYRO verified and experimentally validated trapped gyro-Landau fluid transport model.** *Nuclear Fusion*, 51(8):083001, 2011.
- [6] A. E. Hubbard, R. L. Boivin, R. S. Granetz, M. Greenwald, I. H. Hutchinson et al. **Measurements of the high confinement mode pedestal region on Alcator C-Mod.** *Physics of Plasmas*, 5(5):1744–1751, 1998.



# 6

## I-MODE PEDESTAL STABILITY MODELING

---

### 6.1 MHD STABILITY – ELITE

•

### 6.2 KBM AND INFINITE- $n$ MHD STABILITY

•

### 6.3 SAWTOOTH PERTURBATIONS OF PEDESTAL STABILITY

unknown!!!

•

### 6.4 OTHER MODELS

★



## BIBLIOGRAPHY

---



# 7

## CONCLUSIONS

---

•



## BIBLIOGRAPHY

---



# A

## DIAGNOSTICS

---

The dedicated pedestal experiments, both in I-mode and ELMy H-mode, presented here required an extensive suite of diagnostics to characterize pedestal behavior. Broadly, these diagnostics may be broken down into three categories:

### THOMSON SCATTERING

Details the edge Thomson scattering diagnostic, from which the high-resolution profile data used for the bulk of this thesis was gathered.

### FAST DIAGNOSTICS

Details the Electron-Cyclotron Emission (ECE) and  $H_{\alpha}$  line radiation diagnostics used to track sawtooth crashes and ELM events in the plasma edge.

### FLUCTUATION DIAGNOSTICS

Details Gas-Puff Imaging (GPI), Reflectometry, and other diagnostics used to characterize the mid-frequency fluctuations found in I-mode pedestals.

•

#### A.1 THOMSON SCATTERING

Due to the steep gradients in density, temperature, and pressure found in the pedestal, accurate characterization of plasma profiles in this region requires diagnostics capable of very fine spatial resolution. Measurements based on the Thomson scattering [1] of laser light off of electrons in the plasma provides the high-resolution pedestal profiles used in this thesis: Thomson scattering is a near-direct measurement of electron temperature and density, independent of bulk plasma parameters (i.e., it is unaffected by the cutoffs or reflections found in other diagnostics, and produces no significant perturbation to the plasma). Measurement via Thomson scattering produces an effective “snapshot” of the plasma parameters at each measurement point, with spatial resolution limited only by collection optics geometry, and time resolution limited by repetition rate on the lasers. Despite significant technical difficulties – for example, the high-powered lasers and sensitive collection optics needed to capture the weak scattered light and the necessity for careful calibration of density measurements – Thomson scattering diagnostics remain a versatile and powerful tool for plasma pedestal measurement, and provided the bulk of the profile data used in this thesis.

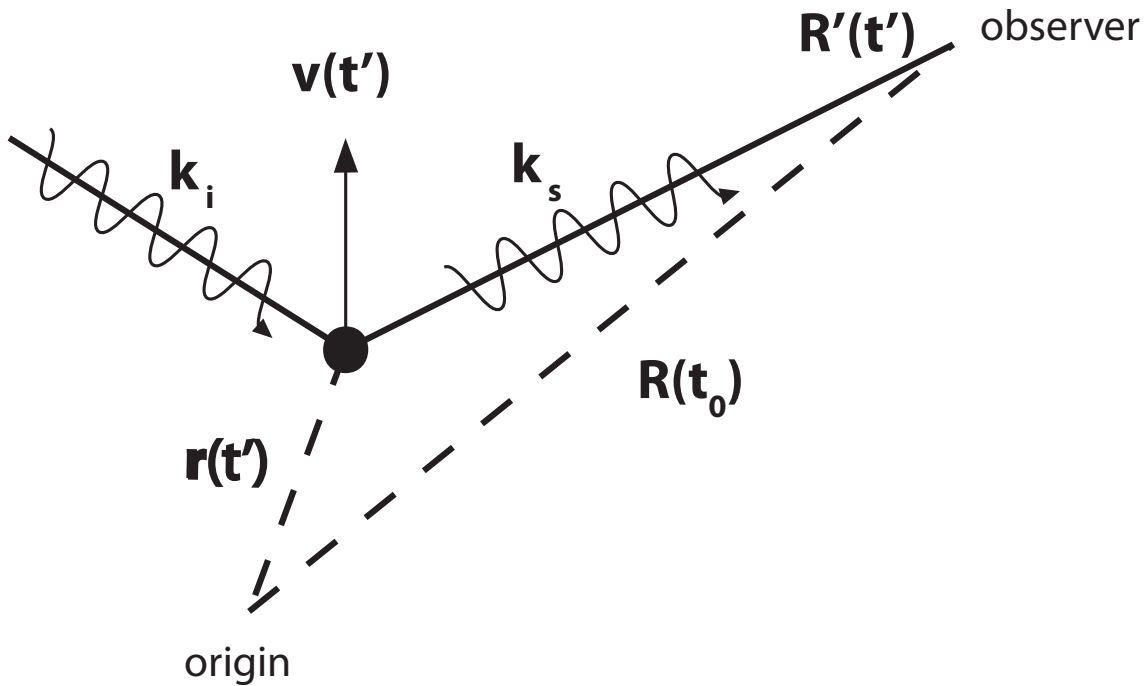


**Figure A.1:** Coordinate system considered for Thomson scattering, with the incident wave of wavenumber  $\vec{k}_i$  incident on a particle at  $\vec{r}(t')$  for retarded time  $t'$ . The scattered wave  $\vec{k}_s$  is drawn to an observer at  $\vec{R}(t')$ .

### A.1.1 Principles of Thomson Scattering

An intuitive picture of the Thomson scattering phenomenon may be obtained by the consideration of a stationary, free electron with an EM wave impinging on it. The particle will be accelerated by the wave (approximately sinusoidally for E-field-dominated acceleration at nonrelativistic speeds), causing it to radiate. Any motion of the electron will cause Doppler shifting in the scattered radiation – motion relative to the incident wave shifts the incident frequency  $\omega_i$ , at which the particle oscillates, while motion relative to an observer shifts the scattered wave. This geometry for general positions of the particle and observer is given in fig. A.1.

The scattered electric field from a generally-accelerated electron moving at  $\beta = \vec{v}/c$  is given from the Lienard-Wiechert potentials [2, §7],

$$\vec{E}_s = \frac{-e}{4\pi\epsilon_0} \left[ \frac{1}{\kappa^3 R c} \hat{s} \times \left( (\hat{s} \times \vec{\beta}) \times \dot{\beta} \right) \right]_{t'} \quad (A.1)$$

$$\kappa = 1 = \frac{\vec{R}' \cdot \vec{v}}{R' c} = 1 - \hat{s} \cdot \vec{\beta}, \quad t' = t - \frac{R'}{c}$$

where  $\hat{s}$  indicates the unit vector along the scattering direction,  $\vec{R} = R\hat{s}$  is the vector to the observer,  $\kappa$  is a relativistic scale factor, and  $t'$  is the relativistic retarded time. The apostrophe indicates a parameter

evaluated at the retarded time, i.e.,  $R' = R(t')$ ; the bracketed term in eq. (A.1) likewise is evaluated at  $t'$ . The scattered power per solid angle is given by

$$\begin{aligned}\frac{dP_s}{d\Omega} &= R^2 \vec{S} \cdot \hat{s} = R^2 \frac{1}{\mu_0} (\vec{E} \times \vec{B}) \cdot \hat{s} \\ &= R^2 \epsilon_0 c (\vec{E}_s \times (\hat{s} \times \vec{E}_s)) \cdot \hat{s} = R^2 c \epsilon_0 |E_s|^2\end{aligned}\quad (\text{A.2})$$

Relativistically, the electron motion (which in turn sets the field determined by eq. (A.1)) is given by

$$\dot{\beta} = \frac{d}{dt} (\gamma m_e \vec{v}) = -e (\vec{E}_i + \vec{v} \times \vec{B}_i) \quad (\text{A.3})$$

where  $\gamma = (1 - \beta^2)^{-1/2}$  is a relativistic scale factor. Thus

$$m_e \gamma \dot{\beta} + \gamma^3 m_e \beta (\vec{\beta} \cdot \vec{\beta}) = -e \left( \frac{\vec{E}_i}{c} + \vec{\beta} \times \vec{B}_i \right) \quad (\text{A.4})$$

Dotting  $\vec{\beta}$  into this and substituting,

$$\dot{\beta} = -\frac{e}{m_e \gamma} \left( \frac{\vec{E}_i}{c} - \frac{\vec{\beta} \cdot \vec{E}_i}{c} \vec{\beta} + \vec{\beta} \times \vec{B}_i \right) \quad (\text{A.5})$$

The general relativistic solution to eqs. (A.1) and (A.2) with the above is rather intractable, although full relativistic treatments have been undertaken [3, 4, 5, 6]. However, the radiated field may be simplified substantially in the nonrelativistic limit – in the limit of  $\beta \ll 1$ , the acceleration is simply

$$\dot{\beta} = -\frac{e}{m_e c} \vec{E}_i \quad (\text{A.6})$$

and the scattered field is

$$\vec{E}_s = \frac{e^2}{4\pi\epsilon_0 m_e c^2} \left[ \left[ \frac{1}{R} \hat{s} \times (\hat{s} \times \vec{E}_i) \right] \right]_{t'}, \quad (\text{A.7})$$

Recalling the classical electron radius,

$$r_e = \frac{e^2}{4\pi\epsilon_0 m_e c^2} \quad (\text{A.8})$$

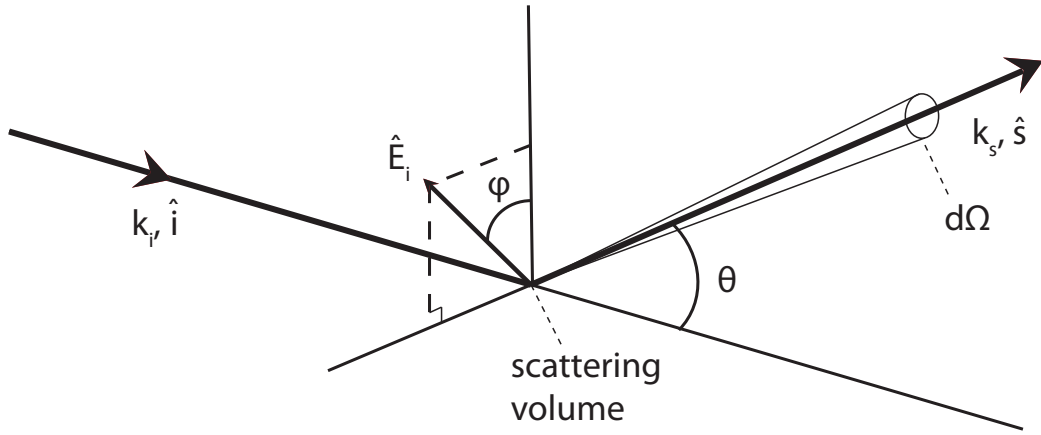


**Figure A.2:** Definitions of the angular dependences in the Thomson scattering geometry: namely, the angle  $\theta$  between the incident wave direction  $\hat{i}$  and scattering direction  $\hat{s}$ , and the polarization angle  $\phi$  of the incident electric field  $\hat{E}_i$  with respect to the projection of  $\hat{s}$  into the polarization plane.

the radiated power is given by

$$\frac{dP_s}{d\Omega} = r_e^2 c \epsilon_0 E_{i0}^2 \llbracket \hat{s} \times (\hat{s} \times \hat{E}_i) \rrbracket^2 \cos^2(\vec{k}_i \cdot \vec{r}' - \omega_i t') \quad (\text{A.9})$$

separating the magnitude, direction, and phase (evaluated at  $t'$ ) of the incident field.

We may first consider the scattering direction dependence,

$$\llbracket \hat{s} \times (\hat{s} \times \hat{E}_i) \rrbracket_{t'}^2 \quad (\text{A.10})$$

Defining the angular geometry as in fig. A.2 for the scattering angle  $\theta$  between the incident wave direction  $\hat{i}$  and scattering direction  $\hat{s}$ , and the polarization angle  $\phi$  (defined between  $\hat{E}_i$  and the projection of  $\hat{s}$  into the polarization plane), this reduces to (cf. [1, §1.7])

$$\llbracket \hat{s} \times (\hat{s} \times \hat{E}_i) \rrbracket^2 = 1 - \sin^2 \theta \cos^2 \phi \quad (\text{A.11})$$

Since the incident power flux is given by

$$S_i = c \epsilon_0 E_{i0}^2 \cos^2(\vec{k}_i \cdot \vec{r}' - \omega_i t') \quad (\text{A.12})$$

We may separate the incident flux and scattering by

$$\frac{dP}{d\Omega} = S_i \frac{d\sigma_t}{d\Omega} \Rightarrow \frac{d\sigma_t}{d\Omega} = r_e^2 [1 - \sin^2 \theta \cos^2 \phi] \quad (\text{A.13})$$

defining a scattering cross-section  $\sigma_t$ . Integrating over  $d\Omega$ ,

$$\sigma_t = \frac{8\pi}{3} r_e^2 = 6.65 \times 10^{-29} \text{ m}^2 \quad (\text{A.14})$$

The extremely small cross-section for Thomson scattering necessitates high-powered lasers and sensitive collection optics – for example, the fraction of photons scattered from a segment along the laser beam path of length  $L$  with electron density  $n_e$  is given simply by  $L n_e \sigma_t$ . For  $L = 1 \text{ mm}$  and  $n_e = 1 \times 10^{20} \text{ m}^{-3}$ , Thomson scattering faces an attenuation factor on the order of  $\sim 10^{-11}$  to the incident photon count from the laser.

The phase of the scattered wave is determined by a retarded-time evaluation of the incident phase,  $\vec{k}_i \cdot \vec{r}(t') - \omega_i t'$ . Substituting  $\vec{r}(t') = \vec{r}_0 + \vec{v}t'$ , and assuming  $R(t') \approx R(t_0)$  (which holds for observers far from the scattering volume,  $R \gg r$ ) we may rewrite the retarded time as

$$t' = \frac{1}{1 - \hat{s} \cdot \vec{\beta}} \left( 1 - \frac{R}{c} + \frac{\hat{s} \cdot \vec{r}_0}{c} \right) \quad (\text{A.15})$$

Substituting, the phase argument becomes

$$k_i \frac{1 - \hat{i} \cdot \vec{\beta}}{1 - \hat{s} \cdot \vec{\beta}} R - \omega_i \frac{1 - \hat{i} \cdot \vec{\beta}}{1 - \hat{s} \cdot \vec{\beta}} t - k_i \frac{1 - \hat{i} \cdot \vec{\beta}}{1 - \hat{s} \cdot \vec{\beta}} \hat{s} \cdot \vec{r}_0 + \vec{k}_i \cdot \vec{r}_0 \quad (\text{A.16})$$

where  $\hat{i}$  is the incident wave propagation direction. We have naturally arrived at the Doppler-shifted frequency,

$$\begin{aligned} \omega_s &= \frac{1 - \hat{i} \cdot \vec{\beta}}{1 - \hat{s} \cdot \vec{\beta}} \omega_i \\ \vec{k}_s &= k_i \frac{1 - \hat{i} \cdot \vec{\beta}}{1 - \hat{s} \cdot \vec{\beta}} \hat{s} = \frac{\omega_s}{c} \hat{s} \end{aligned} \quad (\text{A.17})$$

so the phase is

$$\vec{k}_i \cdot \vec{r}' - \omega_i t' = k_s R - \omega_s t + (\vec{k}_s - \vec{k}_i) \cdot \vec{r}_0 \quad (\text{A.18})$$

Alternately, we may define

$$\begin{aligned} \vec{k} &= \vec{k}_s - \vec{k}_i \\ \omega &= \omega_s - \omega_i = \vec{k} \cdot \vec{v} \end{aligned} \quad (\text{A.19})$$

We may establish the frequency spectrum of the scattered radiation by taking the Fourier transform of the scattered field,

$$\vec{E}_s(\omega_s) = \int \vec{E}_s(t) e^{i\omega_s t} dt \quad (\text{A.20})$$

At retarded time,  $dt = \kappa' dt'$ , and

$$\vec{E}_s(\omega_s) = \frac{r_e}{R'} \int \kappa' \Pi \cdot \vec{E}_i(\vec{r}', t') e^{-\omega_s (t' + \frac{R'}{c} - \frac{\hat{s} \cdot \vec{r}'}{c})} dt' \quad (\text{A.21})$$

Here, for generality we use the polarization tensor  $\Pi$ , which includes relativistic effects – in the nonrelativistic limit  $\Pi = \hat{s}\hat{s} - \mathbf{I}$  such that  $\Pi \cdot \vec{E}_i = \hat{s} \times (\hat{s} \times \vec{E}_i)$ . Using  $\vec{E}_i(\vec{r}, t) = \vec{E}_{i0} \exp(i(\vec{k}_i \cdot \vec{r} - \omega_i t))$  and eq. (A.19),

$$\vec{E}_s(\omega_s) = \frac{r_e}{R'} e^{ik_s R'} \int \kappa' (\Pi \cdot \hat{E}_i) E_{i0} e^{i(\omega t' - \vec{k} \cdot \vec{r}')} dt' \quad (\text{A.22})$$

Integrating and substituting  $\omega_s = 2\pi\nu_s$ ,

$$\vec{E}_s(\nu_s) = \frac{r_e}{R'} e^{ik_s R} 2\pi \kappa (\Pi \cdot \vec{E}_{i0}) \delta(\vec{k} \cdot \vec{v} - \omega) \quad (\text{A.23})$$

We may thus construct the scattered power per solid angle per unit frequency

$$\frac{d^2 P}{d\Omega d\nu_s} = r_e^2 |\Pi \cdot \hat{E}_i|^2 (c \epsilon_0 E_{i0}^2) \delta \left( \nu_s - \frac{1 - \hat{i} \cdot \vec{\beta}}{1 - \hat{s} \cdot \vec{\beta}} \nu_i \right) \quad (\text{A.24})$$

So we have established the scattered power spectrum in solid angle and frequency of a single electron as a function of scattering direction (encoded in  $\Pi \cdot \hat{E}_i$ ) and incident laser energy (in the incident Poynting flux  $\langle S_i \rangle = c \epsilon_0 E_{i0}^2$ ). The scattered spectrum locked to a single frequency by the Dirac delta function, forcing the scattered spectrum to radiate strictly at the Doppler-shifted frequency set by the electron motion.

To consider the spectrum from a population of electrons, we must consider the interactions between nearby electrons. On length scales comparable to the electron Debye length  $\lambda_{De}$  (eq. (1.1)), electrons in the plasma screen out incident electric fields – this organized motion leads to interference in the scattered radiation, referred to as *collective*

or *coherent scattering*. The full solution for the scattered spectrum (see [1, §3]) may be expanded in a series in the factor

$$\alpha = \frac{1}{k\lambda_{De}} \quad (\text{A.25})$$

Coherent effects are negligible in the limit of  $\alpha \ll 1$ , at which the scattering is said to be *incoherent* or *noncollective* – the radiation from a population of electrons is simply the sum of each individual contribution. For the effective scattering wavevector,  $\vec{k} = \vec{k}_s - \vec{k}_i$  (eq. (A.19)),

$$\begin{aligned} |\vec{k}| &= \sqrt{k_s^2 + k_i^2 - 2k_s k_i \cos \theta} \\ &\approx \sqrt{2} k_i \sqrt{1 - \cos \theta} = \sqrt{2} k_i \sqrt{2 \sin^2 \left( \frac{\theta}{2} \right)} \end{aligned} \quad (\text{A.26})$$

assuming  $k_s \approx k_i$ . Thus the noncollective requirement reduces to

$$\frac{1}{2k_i \sin(\theta/2)\lambda_{De}} \ll 1 \Rightarrow \frac{\lambda_i}{\lambda_{De}} \ll 4\pi \sin \left( \frac{\theta}{2} \right) \quad (\text{A.27})$$

This condition is readily satisfied at near-perpendicular scattering ( $\theta \approx 90^\circ$ , where the scattering amplitude is maximized) and with laser wavelengths much smaller than the Debye length ( $\lambda_{De} \sim 10 - 100 \mu\text{m}$  at tokamak conditions, compared to the  $\lambda_i \sim 1 \mu\text{m}$  IR lasers commonly used for Thomson scattering photon sources).

Thus, the incoherent scattered spectrum is simply the sum of contributions from each electron in the scattering volume – the spectrum from a population described by the distribution function  $f_e(\vec{r}, \vec{v})$  is

$$\frac{d^2P}{d\Omega dv_s} = 2\pi r_e^2 \int_V \langle S_i \rangle \int |\Pi \cdot \hat{E}_i|^2 f_e(\vec{r}, \vec{v}) \kappa^2 \delta(\vec{k} \cdot \vec{v} - \omega) d^3v d^3r \quad (\text{A.28})$$

For small scattering volumes, the electron distribution function is approximately uniform in space. In the nonrelativistic limit,  $\Pi \cdot \hat{E}_i$  is independent of velocity, thus the spatial contribution may be separated out:

$$\int_V \langle S_i \rangle |\Pi \cdot \hat{E}_i|^2 d^3r \quad (\text{A.29})$$

encoding the incident photon flux (from the Poynting vector of the laser) and the scattering direction dependence. The velocity integral (noting  $\kappa \approx 1$  in the nonrelativistic case) is

$$\int f(\vec{v}) \delta(\vec{k} \cdot \vec{v} - \omega) d^3 \vec{v} \quad (\text{A.30})$$

Splitting the velocity into components parallel and perpendicular to  $\vec{k}$ ,  $\vec{v}_\perp$ ,  $\vec{v}_k$ , this is

$$\int f(\vec{v}_\perp, \vec{v}_k) \delta(kv_k - \omega) d^2 \vec{v}_\perp dv_k = \int f_k(v_k) \delta(kv_k - \omega) dv_k \quad (\text{A.31})$$

utilizing the normalization required for  $f(\vec{v})$  to solve the integrals over  $\vec{v}_\perp$ . For a Maxwellian (eq. (1.5)) the distribution along the effective wavevector  $\vec{k}$  is

$$f_k(v_k) = n_e \frac{1}{v_t \sqrt{\pi}} e^{-v_k^2/v_t^2} \quad (\text{A.32})$$

thus the above is solvable,

$$\int f_k(v_k) \delta(kv_k - \omega) dv_k = \frac{1}{k} f_k \left( \frac{\omega}{k} \right) \quad (\text{A.33})$$

Substituting into eq. (A.28),

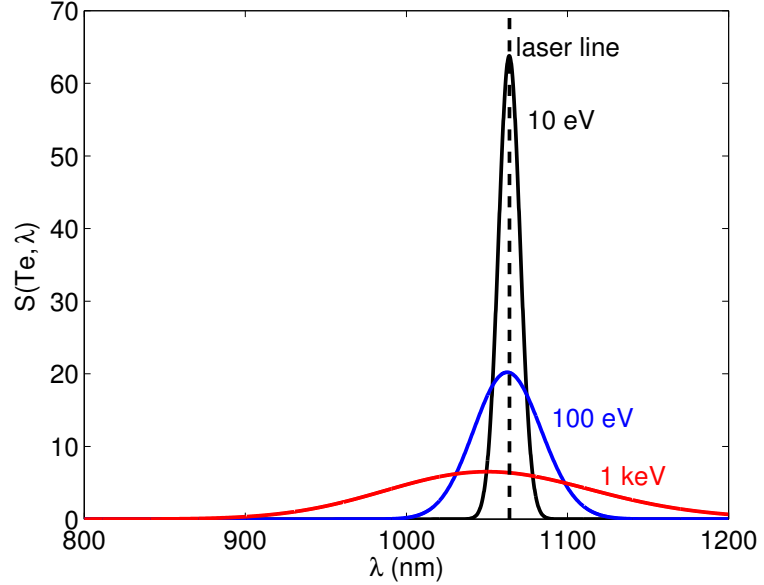
$$\begin{aligned} \frac{d^2 P}{d\Omega dv_s} &= 2\pi r_e^2 \left[ \int_V \langle S_i \rangle |\hat{s} \times (\hat{s} \times \hat{E}_i)|^2 d^3 \vec{r} \right] \times \\ &\quad \frac{1}{\sqrt{\pi k}} \frac{n_e}{v_t} \exp \left( -\frac{\omega^2}{k^2 v_t^2} \right) \end{aligned} \quad (\text{A.34})$$

Substituting  $k \approx 2k_i \sin(\theta/2) = (4\pi/\lambda_i) \sin(\theta/2)$ , the exponent is

$$-\frac{(\omega_s - \omega_i)^2}{4 \frac{4\pi^2}{\lambda_i^2} \sin^2(\theta/2) v_t^2} \approx -\frac{c^2 (\lambda_s - \lambda_i)^2}{4 \lambda_i^2 v_t^2 \sin^2(\theta/2)} \quad (\text{A.35})$$

Converting from a frequency to a wavelength spectrum, and assuming the scattering volume to be sufficiently small that the scattering angle and incident Poynting flux are uniform (thus  $\int \langle S_i \rangle d^3 \vec{r} =$

**Figure A.3:** Spectral functions normalized to density and laser power, evaluated at  $\theta = \phi = \pi/2$ . The spectrum spreads farther from the laser line at higher temperature, as well as blue-shifting due to relativistic effects.



$\langle S_i \rangle AL = P_i L$  for laser cross-section  $A$ , scattering volume  $L$ , and laser power  $P_i$ ) the nonrelativistic scattering spectrum is

$$\frac{d^2P}{d\Omega d\lambda_s} = P_i r_e^2 n_e L |\hat{s} \times (\hat{s} \times \hat{E}_i)|^2 S(T_e, \theta, \lambda_s)$$

$$S(T_e, \theta, \lambda_s) = \frac{1}{2\sqrt{\pi} \sin(\theta/2)} \frac{c}{\lambda_i v_t} \exp\left(-\frac{c^2(\lambda_s - \lambda_i)^2}{4v_t^2 \lambda_i^2 \sin^2(\theta/2)}\right) \quad (\text{A.36})$$

This expression is a Maxwellian centered at  $\lambda = \lambda_i$  with a spread determined by the electron temperature  $T_e$  (manifesting in the thermal velocity  $v_t$ ) and the scattering angle  $\theta$ . Recalling the angle  $\phi$  defined between the incident polarization  $\hat{E}_i$  and the scattering direction  $\hat{s}$  (see fig. A.2),  $|\hat{s} \times (\hat{s} \times \hat{E}_i)|^2 = \sin^2 \phi$  is maximized for scattering perpendicular to the incident laser polarization.

This analysis breaks down for relativistic electron populations. However, relativistic effects (see [1, §9]) may be expressed as a polynomial correction to eq. (A.36),

$$S_{\text{rel}}(T_e, \theta, \lambda_s) = S(T_e, \theta, \lambda_s) \left[ 1 - \frac{3.5(\lambda_s - \lambda_i)}{\lambda_i} + \frac{c^2(\lambda_s - \lambda_i)^3}{4v_t^2 \lambda_i^2 \sin^2(\theta/2)} \right] \quad (\text{A.37})$$

The relativistic correction breaks the symmetry of the Maxwellian spectrum, introducing a net blue shift to the spectrum. Physically, this is due to “relativistic headlighting,” in which the radiation from an accelerating relativistic particle is biased forward of its motion – The radiated power is stronger from particles moving toward the observer

(thus with a blue Doppler shift to their emissions). The spectral form factor  $S(T_e, \theta, \lambda_s)$  is shown in figure fig. A.3, illustrating the width dependence of the spectrum on the electron temperature and the blue shifting evident in the spectrum even at relatively low plasma temperatures.

Examination of eqs. (A.36) and (A.37) readily illustrates the method for extracting  $n_e$  and  $T_e$  measurements from the Thomson scattering spectrum – the spread of the spectrum of scattered radiation is directly tied to the electron temperature, while the integrated amplitude gives electron density (as the total scattered power is linearly proportional to  $n_e$ ). Assumptions regarding the Maxwellian distribution of the electrons allows accurate measurement of the electron profile with relatively simple hardware, detailed in the next section.

### A.1.2 Edge Thomson Scattering on C-Mod

High-resolution density and temperature measurements on C-Mod are achieved with the core [7, 8] and edge [9, 10, 11] Thomson Scattering systems. While extracting density and temperature from the general Thomson-scattered spectrum (eq. (A.28)) for an arbitrary electron distribution  $f_e(\vec{r}, \vec{v})$  is intractible, the spectrum for a thermal electron distribution is well-characterized (see eqs. (A.36) and (A.37)) and can be measured with a relatively simple system.

Both the core and edge TS systems measure light scattered from a pair of neodymium-doped yttrium-aluminum garnet (Nd:YAG) lasers with  $\lambda_i = 1064 \text{ nm}$  fired vertically through the plasma at  $R \sim 69 \text{ cm}$  such that it passes roughly through the magnetic axis. The lasers are each fired at 50 Hz  $180^\circ$  out of phase, such that the pair produce one hundred  $\sim 5 \text{ ns}$  pulses per second, taking effective “snapshots” of the plasma profile. Each pulse provides  $\sim 1 \text{ J}$  of laser energy, corresponding to roughly  $5 \times 10^{18}$  photons per laser pulse, ensuring sufficient collected photons even after the significant attenuation inherent in Thomson scattering. Focusing optics mounted at the vertical entrance port constrict the beam to a  $\sim 2 \text{ mm}$  width through the plasma.

The scattered photons are focused through a Cooke triplet with 1:2 demagnification mounted at an outboard-midplane access port onto an array of fiber-optic collectors mounted on an actuated plate (see fig. A.4). Dedicated edge-viewing fibers are mounted in an adjustable block at the base of the plate, viewing the upper plasma at a scattering angle of  $\theta \sim 80^\circ$ . While the  $\sim 1 \text{ cm}$  spot size of the core fibers is sufficient to resolve the core plasma profile, the small radial extent of the pedestal on C-Mod necessitates the millimeter resolution provided by the edge fibers.

The edge collection fibers deliver the scattered light to a filter polychromator array with 25 available spatial channels divided into four spectral bands. The spectral bandpasses, shown in fig. A.5, are de-

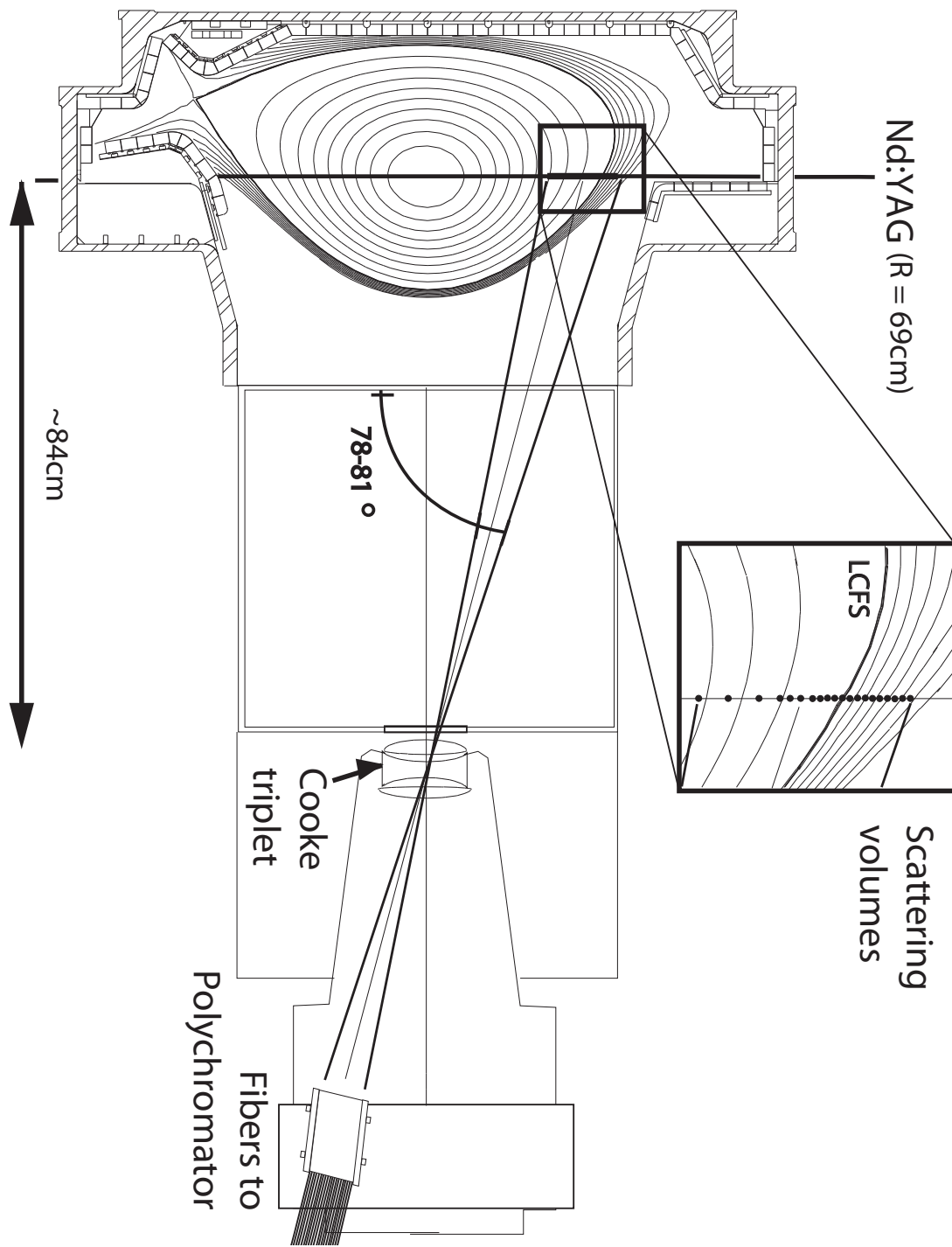
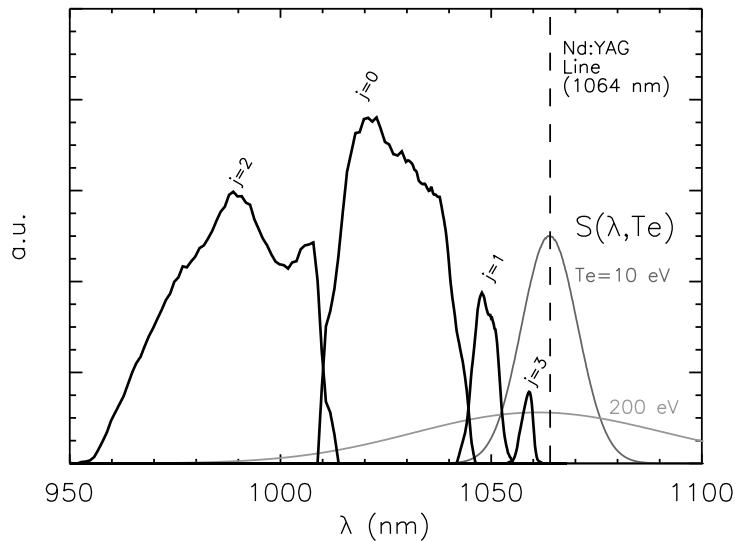


**Figure A.4:** Layout of collection optics for the core and edge Thomson scattering diagnostics on Alcator C-Mod. Two Nd:YAG lasers are fired vertically through the plasma near the magnetic axis, with the scattered light focused through a Cooke triplet at the outboard midplane onto an array of fiber optics. The positions of the high-resolution edge scattering volumes are highlighted in the inset.

**Figure A.5:** Normalized spectral response functions of the edge TS polychromator bandpasses, compared to characteristic scattered spectra at 10 eV and 200 eV.



signed such that the laser line is excluded from the captured light (reducing noise from reflected laser light incident on the fibers) while covering the expected spread in the scattered spectrum across a range of temperatures. Extracting  $n_e$  and  $T_e$  for each spatial channel is conceptually straightforward – the total signal in all spectral channels is analogous to the integrated area under the scattered spectrum (and thus  $n_e$ ), while the relative signal strengths between spectral channels is set by the spread in the spectrum (thus  $T_e$ ). For temperatures below  $\sim 50$  eV (with the true lower bound dependent on the local density), the scattered spectrum is largely restricted to the  $j = 3$  channel, setting a lower bound on the temperature measurement. Similarly, for  $T_e \gtrsim 800$  eV the spectral response in  $j = 1$  and  $j = 3$  is flat, limiting the effectiveness of those spectral bandpasses in constraining the temperature measurement.

Although the  $n_e$  and  $T_e$  measurements from Thomson scattering require careful calibration and sensitive IR optics, the edge TS system provides reliable high-resolution profile measurements across a range of parameters found in the C-Mod edge. Further details on the edge TS hardware, calibration, and data analysis procedures is available in [11, §3].

## A.2 FAST DIAGNOSTICS

In addition to the high spatial resolution necessary to diagnose the pedestal profile – provided by the edge Thomson Scattering system – a suite of diagnostics with high time resolution is desirable to capture rapid variations in plasma parameters near the pedestal. For our purposes, we focus on the electron-cyclotron emission (ECE) and  $H_\alpha$  emission diagnostics. ECE provides fast measurement of local elec-

tron temperature, useful to track the impact of transient events like ELM crashes or sawtooth heat pulses on the pedestal temperature.  $H_{\alpha}$  line emission in the plasma edge provides a measurement of density expelled into the plasma exhaust, marking both the particle transport changes during high-confinement modes and transient density bursts into the SOL during ELM crashes.

### A.2.1 Electron-Cyclotron Emission

Electron-cyclotron emission, or ECE [2, §5.2], arises from the radiation driven by gyro motion of electrons in a magnetized plasma. Relativistically, the electron motion is described by

$$\frac{d}{dt}(\gamma m_e \vec{v}) = -e(\vec{v} \times \vec{B}) \quad (\text{A.38})$$

resulting in gyro-motion at the (relativistic) cyclotron frequency

$$\omega_c = \frac{eB}{\gamma m_e} \quad (\text{A.39})$$

While it is conceptually straightforward to substitute this motion into the Lienard-Wiechert potentials, eq. (A.1), the complexity of the motion results in a rather intractible general form for the radiation even for a single electron, requiring an infinite sum of Bessel functions to characterize the harmonics of the radiation. Fortunately, ECE systems may exploit the trait that electrons undergoing gyro-motion will also *absorb* radiation at the same frequency as their emitted radiation. Over a given path  $s$  through the plasma, the absorption is governed by the absorption coefficient  $\alpha(\nu)$  (fractional absorption per unit path length), with which the radiated intensity  $I(\nu)$  is given by

$$\frac{dI}{ds} = j(\nu) - I\alpha(\nu) \quad (\text{A.40})$$

where  $j(\nu)$  is the frequency-dependence emissivity. For two points  $s_1$ ,  $s_2$  along a path, this is solved by

$$I(s_2) = I(s_1)e^{\tau_1 - \tau_2} + \int_{s_1}^{s_2} j(\nu)e^{\tau - \tau_2} ds \quad (\text{A.41})$$

$$\tau \equiv \int_s \alpha(\nu) ds$$

for the optical depth  $\tau$ . When the optical depth for a given path  $\tau_{21} \equiv \tau_2 - \tau_1$  satisfies  $\tau_{21} \gg 1$ , the plasma within the path absorbs all

radiation incident upon it – it may then be treated as optically black, with the radiation given by the blackbody intensity

$$I(\nu) = \frac{\nu^2}{c^2} \frac{h\nu}{e^{h\nu/T} - 1} \approx \frac{\nu^2 T}{c^2} \quad (\text{A.42})$$

with the approximation holding for  $h\nu \ll T$ . In a broad range of tokamak plasma conditions, the first few harmonics will be optically thick, meaning that the intensity of those harmonics is a direct, straightforward measurement of the electron temperature.

This analysis must be modified somewhat to account for a spatially-varying magnetic field (for example, the  $B_T \sim 1/R$  variation in a tokamak). Fortunately, for a given frequency  $\nu_0$  the emission is only strong close to the position of exact resonance. Through this resonance layer at location  $s_0$ , the optical depth for a given harmonic  $m$  is given by

$$\tau_m = \frac{\alpha_m(s_0)}{m |d\omega_c/ds|} \quad (\text{A.43})$$

with the emission given by

$$I(\nu_0) = \frac{\nu_0^2 T(s_0)}{c^2} (1 - e^{-\tau_m}) \quad (\text{A.44})$$

Thus electron-cyclotron emission in a tokamak allows easy measurement of electron temperature. By observing emission within a given frequency band, the measurement may be localized to a resonance layer, the location of which is calculated by the known magnetic field variation  $d\omega_c/ds$ .

**dig up refs for C-Mod ECE system**

### A.2.2 $H_\alpha$ Emission

•

## A.3 FLUCTUATION DIAGNOSTICS

★

## BIBLIOGRAPHY

---

- [1] J. Sheffield. *Plasma Scattering of Electromagnetic Radiation*. Academic Press, 1975.
- [2] I.H. Hutchinson. *Principles of Plasma Diagnostics*. Cambridge University Press, 2005.
- [3] J. Sheffield. The incoherent scattering of radiation from a high temperature plasma. *Plasma Physics*, 14(8):783, 1972.
- [4] T. Matoba, T. Itagaki, T. Yamauchi and A. Funahashi. Analytical approximations in the theory of relativistic Thomson scattering for high temperature fusion plasma. *Japanese Journal of Applied Physics*, 18(6):1127–1133, 1978.
- [5] A. C. Selden. Simple analytic form of the relativistic Thomson scattering spectrum. *Physics Letters A*, 79(5-6):405 – 406, 1980.
- [6] O. Naito, H. Yoshida and T. Matoba. Analytic formula for fully relativistic Thomson scattering spectrum. *Physics of Fluids B: Plasma Physics*, 5(11):4256–4258, 1993.
- [7] Reich Watterson and Kuo-In Chen. Status of the Alcator C-Mod scanning two-dimensional Thomson scattering diagnostic. *Review of Scientific Instruments*, 61(10):2867–2869, 1990.
- [8] D. A. Mossessian, A. Hubbard and J. Irby. Performance of Alcator C-Mod core Thomson scattering system. *Review of Scientific Instruments*, 70(1):759–762, 1999.
- [9] J. W. Hughes, D. A. Mossessian, A. E. Hubbard, E. S. Marmar, D. Johnson et al. High-resolution edge Thomson scattering measurements on the Alcator C-Mod tokamak. *Review of Scientific Instruments*, 72(1):1107–1110, 2001.
- [10] J. W. Hughes, D. Mossessian, K. Zhurovich, M. DeMaria, K. Jensen et al. Thomson scattering upgrades on Alcator C-Mod. *Review of Scientific Instruments*, 74(3):1667–1670, 2003.
- [11] Jerry W. Hughes. *Edge Transport Barrier Studies On the Alcator C-Mod Tokamak*. PhD thesis, Massachusetts Institute of Technology, 2005.



# B

## HIGH-RESOLUTION PEDESTAL DATABASE

For the work presented in this thesis, a subset of recent I-mode experiments on Alcator C-mod was prepared with high-resolution pedestal data. These data are stored in an SQL database under the C-Mod “log-book” system. Use of an SQL table enables efficient cross-platform access to pedestal data in a format ideal for data mining, and allows for easy extensibility of stored parameters for additional experiments. The database stores windows of data in which plasma parameters (e.g., temperature, stored energy, density, heating power) are steady – usable phases last at least  $\sim 100$  ms ( $\sim 10$  Thomson scattering frames), over which frames of TS pedestal data are averaged. For each phase, the SQL database stores a variety of physics and engineering parameters, and scalar fitting parameters for the pedestal. For direct comparison, the table also stores analogous data from L- and H-mode phases.

*point to mtanh  
fitting function*

**Table B.1:** SQL database parameters used as keys – (SHOT, TA, TB) is sufficient to uniquely identify entries in the database.

<i>column</i>	<i>data type</i>	<i>units</i>	<i>description</i>
SHOT	long		C-Mod shot number
TA	long	ms	start time of phase
TB	long	ms	end time of phase
MODE	string		type of phase in window, e.g., ‘IMODE’, ‘ELMY’, ‘EDA’, ‘LMODE’

★

**Table B.2:** SQL database parameters used as flags for time windows.

<i>column</i>	<i>data type</i>	<i>units</i>	<i>description</i>
ELMS	int		binary flag, = 1 for ELMs in phase
LH	int		binary flag, = 1 for LHCD in phase
WCM	int		binary flag, = 1 for WCM fluctuation in phase (I-mode only)
TREE_PATH	string		path to branch in pedestal-profile MDS tree
TREE_SHOT	long		shot number flagged in pedestal-profile MDS tree, used to differentiate sub-branches of a single shot
SEED_SPC	string		gas seeding species (Ne, N, Ar) - None for no gas seeding

**Table B.3:** SQL database parameters for useful measured parameters.

<i>column</i>	<i>data type</i>	<i>units</i>	<i>description</i>
NLo4	float	$\text{m}^{-2}$	line-integrated density from TCI
NLo4_ERR	float	$\text{m}^{-2}$	error in NLo4
NEBAR	float	$\text{m}^{-3}$	line-averaged density from TCI
NEBAR_ERR	float	$\text{m}^{-3}$	error in NEBAR
ECE_To	float	eV	core electron temperature from ECE
ECE_TPED	float	eV	pedestal electron temperature from ECE (channel nearest 95% flux surface)
NEo	float	$\text{m}^{-3}$	core density from TS
NEo_ERR	float	$\text{m}^{-3}$	error in NEo
TEo	float	eV	core temperature from TS
TEo_ERR	float	eV	error in TEo
NUSTAR	float		pedestal collisionality at 95% flux surface
RHOSTAR	float		pedestal normalized gyroradius at 95% flux surface
ZEFF	float		average effective charge
ZEFF_ERR	float		error in ZEFF measurement

**Table B.4:** SQL database parameters for EFIT values.

<i>column</i>		<i>data type</i>	<i>units</i>	<i>description</i>
KAPPA		float		plasma elongation $\kappa$ (see fig. 1.6)
KAPPA_ERR		float		error in KAPPA
DELTA_U		float		plasma upper triangularity (see fig. 1.6)
DELTA_U_ERR		float		error in DELTA_U
DELTA_L		float		plasma lower triangularity (see fig. 1.6)
DELTA_L_ERR		float		error in DELTA_L
IP		float	MA	plasma current
IP_ERR		float	MA	error in IP
DIDT		float	MA s <sup>-1</sup>	change in plasma current $dI_p/dt$
DIDT_ERR		float	MA s <sup>-1</sup>	error in DIDT
BT		float	T	axial toroidal field
BT_ERR		float	T	error in BT
BP		float	T	flux-surface averaged edge poloidal field
BP_ERR		float	T	error in BP
Qo		float		axial safety factor $q_0$
Qo_ERR		float		error in Qo
Q95		float		edge safety factor $q_{95}$
Q95_ERR		float		error in Q95
R		float	cm	major radius
A		float	cm	outboard-midplane minor radius
SSEP		float	?	separatrix separation?
BETAT		float		global toroidal beta, $\langle \beta_t \rangle$
BETAP		float		global poloidal beta, $\langle \beta_p \rangle$
BETAN		float	m T MA <sup>-1</sup>	global normalized beta, $\beta_N = \langle \beta \rangle / (I_p/aB_t)$
TAU_MHD		float	s	MHD energy confinement time, $\tau_E$
TAU_MHD_ERR		float	s	error in TAU_MHD

**Table B.5:** SQL database parameters for heating power, stored energy, and confinement.

<i>column</i>	<i>data type</i>	<i>units</i>	<i>description</i>
PLASMA_W	float	J	plasma stored energy
PLASMA_W_ERR	float	J	error in PLASMA_W
DWDT	float	W	change in stored energy, $dW_{\text{plasma}}/dt$
DWDT_ERR	float	W	error in DWDT
P_ICRF	float	MW	absorbed ICRF heating power
P_ICRF_ERR	float	MW	error in P_ICRF
P_OHM	float	MW	Ohmic heating power
P_OHM_ERR	float	MW	error in P_OHM
P_LH	float	MW	absorbed lower-hybrid heating power
P_LH_ERR	float	MW	error in P_LH
P_RAD	float	MW	radiated power from bolometry
P_RAD_ERR	float	MW	error in P_RAD
P_SOL	float	MW	power through SOL <b>check this!!!</b>
P_SOL_ERR	float	MW	error in P_SOL
P_THRES	float	MW	H-mode threshold power <b>citation?</b>
P_THRES_ERR	float	MW	error in P_THRES
H	float		ITER98y2 H-mode confinement scaling, $H_{98} = \tau_E / \tau_{98y2}$
H_ERR	float		error in H
H89	float		ITER89 L-mode confinement scaling, $H_{89} = \tau_E / \tau_{89}$
H89_ERR	float		error in H89

**Table B.6:** SQL database parameters for high-resolution pedestal profiles.

<i>column</i>	<i>data type</i>	<i>units</i>	<i>description</i>
NEPED_H	float	$\text{m}^{-3}$	density pedestal height
NEPED_H_ERR	float	$\text{m}^{-3}$	error in NEPED_H
NEPED_B	float	$\text{m}^{-3}$	density pedestal baseline
NEPED_B_ERR	float	$\text{m}^{-3}$	error in NEPED_B
NEPED_D	float		density pedestal half-width
NEPED_D_ERR	float		error in NEPED_D
NEPED_Ro	float		density pedestal midpoint
NEPED_Ro_ERR	float		error in NEPED_Ro
NEPED_ALPHA	float		density pedestal inboard-slope parameter
NEPED_ALPHA_ERR	float		error in NEPED_ALPHA
NEPED_GRAD	float	$\text{m}^{-3}$	peak density pedestal gradient (pedestal midpoint)
NEPED_GRAD_ERR	float	$\text{m}^{-3}$	error in NEPED_GRAD
NEPED_LGRAD	float		peak density pedestal gradient scale length
NEPED_LGRAD_ERR	float		error in NEPED_LGRAD
NEPED_95	float	$\text{m}^{-3}$	density at 95% flux surface
NEPED_95_ERR	float	$\text{m}^{-3}$	error in NEPED_95
TEPED_H	float	eV	temperature pedestal height
TEPED_H_ERR	float	eV	error in TEPED_H
TEPED_B	float	eV	temperature pedestal baseline
TEPED_B_ERR	float	eV	error in TEPED_B
TEPED_D	float		temperature pedestal half-width
TEPED_D_ERR	float		error in TEPED_D
TEPED_Ro	float		temperature pedestal midpoint
TEPED_Ro_ERR	float		error in TEPED_Ro
TEPED_ALPHA	float		temperature pedestal inboard-slope parameter
TEPED_ALPHA_ERR	float		error in TEPED_ALPHA
TEPED_GRAD	float	eV	peak temperature pedestal gradient (pedestal midpoint)
TEPED_GRAD_ERR	float	eV	error in TEPED_GRAD
TEPED_LGRAD	float		peak temperature pedestal gradient scale length
TEPED_LGRAD_ERR	float		error in TEPED_LGRAD
TEPED_95	float	eV	temperature at 95% flux surface
TEPED_95_ERR	float	eV	error in TEPED_95
PEPED_H	float	$/\text{m}^3 \text{eV}$	pressure pedestal height
PEPED_H_ERR	float	$/\text{m}^3 \text{eV}$	error in PEPED_H
PEPED_B	float	$/\text{m}^3 \text{eV}$	pressure pedestal baseline
PEPED_B_ERR	float	$/\text{m}^3 \text{eV}$	error in PEPED_B
PEPED_D	float		pressure pedestal half-width

**Table B.7:** SQL database parameters for WCM fluctuation measurements.

<i>column</i>	<i>data type</i>	<i>units</i>	<i>description</i>
WCM_AMP	float		normalized peak amplitude of WCM from reflectometry
WCM_FREQ	float	kHz	centroid frequency of WCM from reflectometry
WCM_WID	float	kHz	spectral width of WCM determined by $\pm\sigma$ of Gaussian fit on reflectometry
WCM_AMP_PCI	float		normalized peak amplitude of WCM from PCI
WCM_FREQ_PCI	float	kHz	centroid frequency of WCM from PCI
WCM_WID_PCI	float	kHz	spectral width of WCM determined by $\pm\sigma$ of Gaussian fit on PCI

## COLOPHON

This document was typeset using `classicthesis` developed by André Miede (although aspects were changed to comply with the MIT thesis standards and the author’s personal preferences). The style was inspired by Robert Bringhurst’s seminal book on typography “*The Elements of Typographic Style*”. `classicthesis` is available for both L<sup>A</sup>T<sub>E</sub>X and L<sup>A</sup>T<sub>E</sub>X:

<http://code.google.com/p/classicthesis/>

Hermann Zapf’s *Palatino* and *Euler* type faces (Type 1 PostScript fonts *URW Palladio L* and *FPL*) are used. The “typewriter” text is typeset in *FPL*, originally developed by Bitstream, Inc. as “Bitstream Vera”. (Type 1 PostScript fonts were made available by Malte Rosenau and Ulrich Dirr.)